Topographical, chemical and optical studies of single crystal rubrene.

Robert J. Thompson

PhD Thesis submitted for the degree of Doctor of Philosophy
Within the field of Physics of Organic Materials
Within the Department of Electronic and Electrical Engineering

13 January 2014

Declaration

I, Robert J. Thompson confirm that the work presented in this thesis is my own. Where information has been derived from other sources, I confirm that this has been indicated in the thesis.

_____

Robert J. Thompson

To Mum and Dad.

Abstract

This thesis presents a study of material characterisation methods and techniques, which can determine the effects of surface and structural defects on the properties of single crystal rubrene.

A method of cleaving is devised to produce surfaces free from previous exposure to the ambient. This method reproducibly provides large terraces intersected by straight, well orientated step edges. Atomic force microscopy studies show the cleaved surfaces undergo environmentally dependent molecular reorganization. This results in the formation of nanoscale 'beads' at molecular step edges and narrow 'fingers', one molecule high. The beads show an insulating behaviour with increased conduction at the surrounding surface.

The methodology of applying time of flight secondary ion mass spectroscopy to rubrene crystals is developed to study the chemical composition both at and below the surface. This shows a uniform oxide ($C_{42}H_{28}O$) covering the surface with an increased concentration of peroxide ($C_{42}H_{28}O_2$) located at crystallographic defects.

To investigate the effect of surface and defects on exciton dynamics in rubrene a confocal photoluminescence (PL) arrangement is designed and built. An extended PL distribution is imaged providing evidence of exciton diffusion within the material. This diffusion is seen to increase within the bulk with a suppression of emission at 603nm. Defects are seen to affect PL with emission of the 650nm PL band having a greater contribution in the presence of defects. This emission is also spatially displaced from the maximum intensity of the other bands. These results imply the existence of a defect mediated recombination pathway.

These studies show that environmental reactions readily occur at the location of crystallographic defects and step edges. This is of importance to the operation of rubrene electrical devices.

This work provides a set of techniques and developed methodologies which enable the characterisation of technologically important processes on rubrene. These should extend to other organic single crystals such as pentacene and tetracene.

Acknowledgements

I wish to thank the following people whose efforts, guidance and friendship have made this work possible. First and foremost thanks are offered to my principal supervisor Oleg Mitrofanov for providing a topic of interest which facilitated far more possibilities for scientific exploration than could be covered in the length of one PhD. I also thank him for his patience and guidance throughout the duration of my work.

I would like to thank my secondary supervisor Neil Curson who has been more proactive and involved than many principal supervisors. He has made the task of undertaking a PhD far more enjoyable as well as manageable, by providing both science expertise and a deep understanding of the doctoral degree process and academic life.

My gratitude is offered to Tom, Jim and Trevor from the workshop for not only their skilled craftsmanship but also their adept talent of producing components in timeframes which they had categorically informed me were not possible. The workshop has become a refuge from the long hours spent in front of optical benches and computer monitors. Their wit and humour made many visits to the workshop far more entertaining and enjoyable than was wise as it only lead to far more frequent visits.

Thanks to Gerald, Scott, Lee and Andy for all the aid which they offered. A technical issue was never a problem for long with such a friendly, efficient and knowledgeable support team. I especially thank Gerald without whose patience and persistence I would still be sitting exasperated in a laboratory trying to coerce computers and equipment to talk to each other.

I also would like to thank Steve Hudziak for undertaking the initial AFM experiments and for always being ready with a guiding hand to offer help and assistance. He keeps a lab similar in fashion to Aladdin's cave; no item ever required cannot be found within.

I would like to thank my good friends and family who have always been willing and ready to offer moral support, friendship and the occasional drinking session. A special mention must go to Dr. Raimund Mueckstein who throughout this journey has been paving the way just far enough ahead to allow me to steer away from the rough terrain which he often encountered.

Finally I wish to thank my parents whose loving encouragement, guidance, support, and grounding is always offered, always of help, but never receives enough thanks. Without your steadfast devotion this work could not exist.

Table of contents

Table of figures

Chapter 1

Introduction

Organic semiconductors form the basis of organic electronics and photonics. They are materials formed of hydrocarbons which possess semiconducting properties† due to the conjugated nature of their bonding.

Figure 1-1 Flexible organic solar cell produced by eight19.

The interest in organic semiconductors has rapidly increased over the past two and a half decades. This great interest arises from the unique properties which this class of semiconductors possesses. These include being easily solution processed at relatively very-low cost which allows deposition onto low cost, large area, flexible substrates.[1, 2, 3, 4, 5] The 'soft' nature of organic electronics also makes it's interface with biology a possibility.[6, 7]

The compatibility with flexible substrates is made possible due to the low temperature solution based processing that removes the necessity for rigid substrates that are required to withstand the high temperatures during deposition of traditional semiconductor materials. The benefits of this development are not just confined to novel device design previously inaccessible, such as electronic devices which can replicate the flexible nature of paper for e readers, or solar chargers which can be rolled up. The major benefit is the new manufacturing processes allowed, such as

† Semiconductors are a class of solids which sit in between conductors and insulators. They are insulators at 0 K and require energy to provide free charge carriers which allow current to flow.

newspaper style roll to roll printing of electronics.[8] This manufacturing technique has the potential to reduce production costs of electronic device fabrication.[9]

One of the most important and novel properties of organic semiconductors is that the structure of their constituent molecules can be altered. This allows "tuning" of the semiconductors properties such as band gap energies and therefore emission and absorption wavelengths.[10, 11] These properties mean that the fields of organic electronics and photonics are ideally suited to facilitate the development of flexible, low-cost, disposable electronics. This includes devices such as organic solar cells, light-emitting displays, smart tags and molecular sensors.[4, 9] Figure 1-1 shows a flexible organic solar cell exemplifying the potential device design opportunities which organic semiconductors offer.

The study of organic materials for use in photonics and electronics began in the 1960's when electro-luminescence was first seen in organic semiconductor crystals.[12, 13] Upon this discovery a small scientific community began to form with an interest in the electrical properties of these small molecules and also conjugated polymers. This community and the interest in these materials flourished in the 1990's, making huge progress by the end of the decade with the 2000 Nobel prize for chemistry being awarded to A.J.Heeger, A.G.MacDiarmid and H.Shirakawa for their research into the area of conductivity of organic materials.[14, 15, 16, 17]

Research into organic semiconductors has now taken two specific directions. Each direction concentrating on one of the two distinct groups of organic materials: organic small molecules and polymers. Although much research has been carried out in both areas, an understanding of the fundamental properties of organic materials is lacking. Notably charge transport, which is well understood and modelled in inorganic materials, is a topic of debate and controversy in organic semiconductors. It is expected that due to the low coupling between molecules in organic materials a charge hopping mechanism for conduction should exist though experimental data seems to show a much more band like charge transport mechanism. A well-defined model of the transport mechanisms leading to an understanding of the origin of band gaps and band gap states is needed to further our understanding of both optical and electronic characteristics in organics. This is discussed in further detail specifically in the context of rubrene with Section 2.2

Both groups of organic materials are commonly processed as amorphous films which can be easily produced over large areas. However this leads to a high level of disorder, making probing of the fundamental properties at best problematic, and in general almost impossible.[18, 19] The single crystalline form of the material has a highly ordered structure over large areas and an increased purity. It is this lack of defects and well orientated structure which allows bypassing of

the disorder limited processes and produces the highest charge carrier mobilities and longest exciton diffusion lengths recorded in organic bulk materials increasing their potential performance for use in field effect transistors and photovoltaic cells respectively.[20, 21, 22, 23] These single crystals allow access to the fundamental (non-defect limited) material properties: charge excitation, transport of the resultant carriers, intrinsic surface and interfacial phenomena and pure-materials optical spectra.

Figure 1-2 Left, Worlds first curved 3D OLED TV produced by LG. **Right,** OLED white light source panels produced by LG Chem.

Although a thorough model of the intrinsic electronic properties of organic semiconductors is yet to be defined, research has led to applications in low-cost, flexible and efficient electronics such as flexible displays, organic solar cells and printed microelectronic circuits.[2, 4, 24] Figure 1-2 shows some of the applications of organic semiconductors which are currently commercially available.

1.1 Why is rubrene of interest?

The studies reported within this work will focus on rubrene ($C_{42}H_{28}$). This organic semiconductor in its crystalline phase has shown excellent properties making it the ideal material for studying the mechanisms which control the properties of organic semiconductors. Figure 1-3, Figure 1-4 and Figure 1-5 exemplify some of the properties which make rubrene a material of such interest. These include the highest recorded field effect mobility for any bulk organic semiconductor; a mobility larger than that of amorphous silicon, as shown in Figure 1-3. High carrier mobility increases the speed at which a transistor can be "turned on or off" making rubrene an ideal material for the development of high performance field effect transistors.[22, 23, 25] Rubrene also shows the largest diffusion of photo excitation energy. This is mediated by molecular excitons and has been directly imaged, as shown in Figure 1-4.[20] A long excitation diffusion length provides the possibility of highly efficient photovoltaics as excitons must diffuse to an interface in order to contribute to the electronic current. As discussed by Najafov et al. [21]

recent studies of organic semiconductors have concentrated on polycrystalline and amorphous films where the exciton diffusion length is on the order of ~ 10-50 nm, much smaller than the absorption length of light in the visible spectrum with an absorption coefficient of approximately 1 μm. Rubrenes exciton diffusion on the μm scale therefore creates an excellent platform for the development and study of single crystals for use in organic photovoltaics. The processes defining exciton generation, diffusion and separation are discussed in Section 2.3.5

Figure 1-5 demonstrates how the mobility of single crystal rubrene remains constant even with bending of the crystal to substantial radiuses,[26, 27] another property showing the potential for novel device design which rubrene offers.

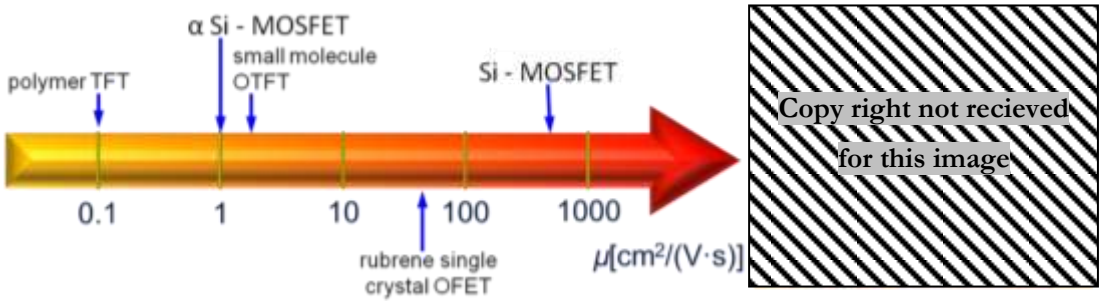

Figure 1-3 The rubrene field effect mobility placed in context of the standard field effect mobilities of other technologies. **Right:** rubrene field effect transistor on a single crystal.

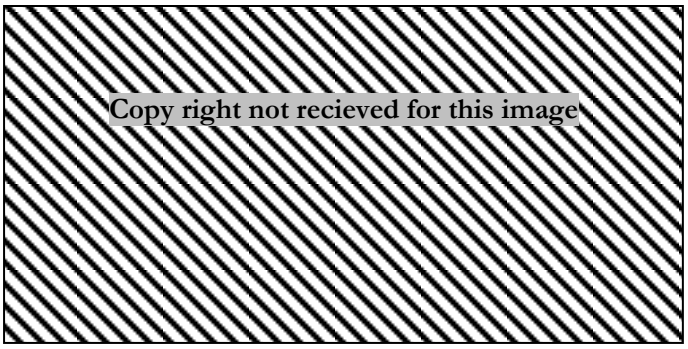

Figure 1-4 Direct image of the large exciton diffusion in rubrene singly crystals.[20]

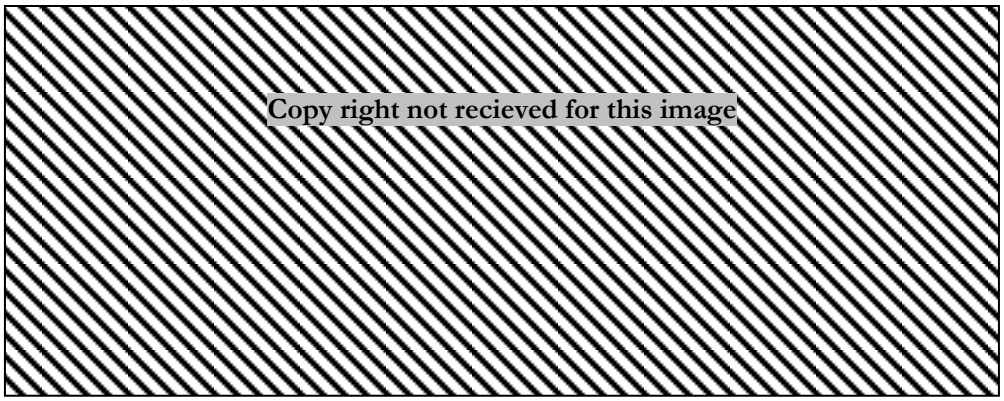

Figure 1-5 Device images and plot of bending vs. mobility showing the maintained integrity of flexible rubrene transistors.[27]

1.2 Thesis outline

Within the studies presented in this thesis I aim to explore the effect of exposure to the ambient environment. Particular attention is paid to the development of the material at the site of defects. These locations are seen to play a key role in evolution of rubrene upon exposure to the ambient. In characterising the material I will probe the electrical, optical, topographical and chemical properties of the material. Understanding how these properties change will provide valuable information for the design and operation of future rubrene based electronic devices.

This thesis begins with a detailed discussion of the physical processes which are known to control the properties of rubrene. This discussion will include the processes which are commonly accepted throughout the research community as well as the areas in which ambiguity still exists. This chapter will also introduce the affects which defect incorporation can have upon the material's properties. After this discussion the aims of the research will be presented. This will be followed by an explanation of the experimental techniques undertaken within the research. Chapters 4, 5 and 6 will then present and discuss the findings of each set of studies. Each of these chapters will concentrate on one of the three main techniques employed: atomic force microscopy, time of flight secondary ion mass spectroscopy and optical spectroscopy. Chapter 7 will then present the conclusions of the work and introduce the future studies which will be undertaken in response to the research presented in this thesis.

Chapter 2

Rubrene the molecule & crystal

Rubrene (5,6,11,12-Tetraphenyltetracene‡) consisting of 42 carbon and 28 Hydrogen atoms ($C_{42}H_{28}$) is a polycyclic aromatic hydrocarbon, (polycyclic, meaning contains multiple closed rings of atoms; aromatic, meaning containing benzene rings; hydrocarbon, meaning composed entirely of hydrogen and carbon). It is one of the most exciting and promising small molecule organic semiconductors, being a record breaker in photocurrent generation efficiency, exciton diffusion length and charge carrier mobility.[22, 23, 25] The first successful demonstrations of high-performance organic field effect transistor (OFET) devices were performed on single crystal rubrene in 2002-2003.[28, 29] Rubrene also shows an interesting set of photo physical processes including: luminescence mediated by band gap states[30] and structure dependent photo luminescence.[31] Due to all of these properties, rubrene is an excellent candidate for electrical components, primarily photovoltaic cells and field effect transistors. The purity of crystals grown via the vapour transport method also makes the material an ideal model system for organic molecular crystals, allowing us to probe the "upper limit" of what can be aimed for in practical organic electronic devices.

Having been the focus of intense study, rubrene still has many questions yet unanswered about its properties. Currently the nature of excitons and the origin of band gap states, which both affect the conductivity of the material, are areas of concentrated research. These electronic properties are sensitive to both atmospheric and material treatment. Before reliable device fabrication can be accomplished they require understanding and controlling.

Within this chapter I will review the material rubrene in single crystal form, looking at some of the physical processes which control its observed properties. I will finish by posing the questions I will aim to address throughout the work presented here.

‡ IUPAC nomenclature, 5,6,11 & 12 refer to the location of the phenyl groups.[107]

2.1 The material

2.1.1 The molecule, $C_{42}H_{28}$

Rubrene molecules consist of a tetracene backbone (4 fused benzene rings) with two phenyl side rings attached to each of the central benzene rings, as shown in Figure 2-1.[32]

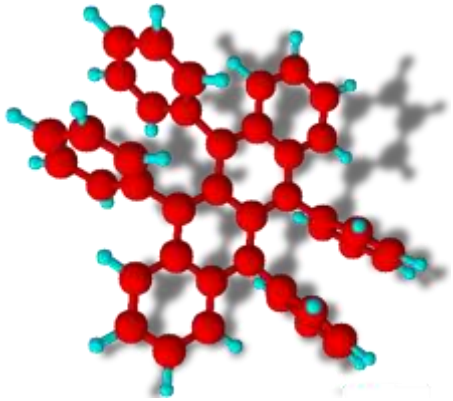

Figure 2-1 3D image of the molecular structure of rubrene. Hydrogen and carbon are represented in light blue and red respectively. The molecule consists of a tetracene backbone (4 fused benzene rings) and 4 phenyl side groups.

The tetracene backbone produces a conjugated conduction pathway across the molecule. The large rotation of the phenyl groups out of the plane of the backbone reduces the delocalisation of the electron wave function over the entire molecule. This prevents a conduction pathway from existing perpendicular to the tetracene backbone. As is discussed further in Section 2.2 . Petrenk *et al.* report an interesting study on the effect of the phenyl rings by comparing the respective molecular orbitals of rubrene and tetracene,[31] showing evidence of greater coupling to vibronic modes in rubrene. Although of note, their study concentrated on the single isolated molecule and within this work I will be concentrating on rubrene in crystalline form.

2.1.2 The crystal

Within this study I aim to probe the intrinsic properties of the material rubrene, investigating how these are altered by the presence of external components introduced by exposure to the ambient environment. In order to probe these properties we must start with a high quality sample which is not dominated by defect driven processes. It is well known that for polycrystalline and amorphous films of rubrene, defects are readily and unintentionally incorporated within the material.[33, 34, 35] The most pure form of the material, which is resilient to the incorporation of chemical defects, and contains a low density of structural defects, is that obtained in the high quality crystals grown by vapour transport (see Section 2.1.3).

The most common polymorph of rubrene crystals grown by vapour transport has an orthorhombic symmetry with a `herringbone' packing in the ab-plane as seen in Figure 2-2.[32, 36] The unit cell of rubrene contains 4 molecules and has dimensions as specified in Table 2-1.[32] Throughout this work I will adhere to the nomenclature presented in Figure 2-2 for the crystallographic axes of rubrene. Any data referred to will also be presented adhering to these labels regardless of the nomenclature of the source material.

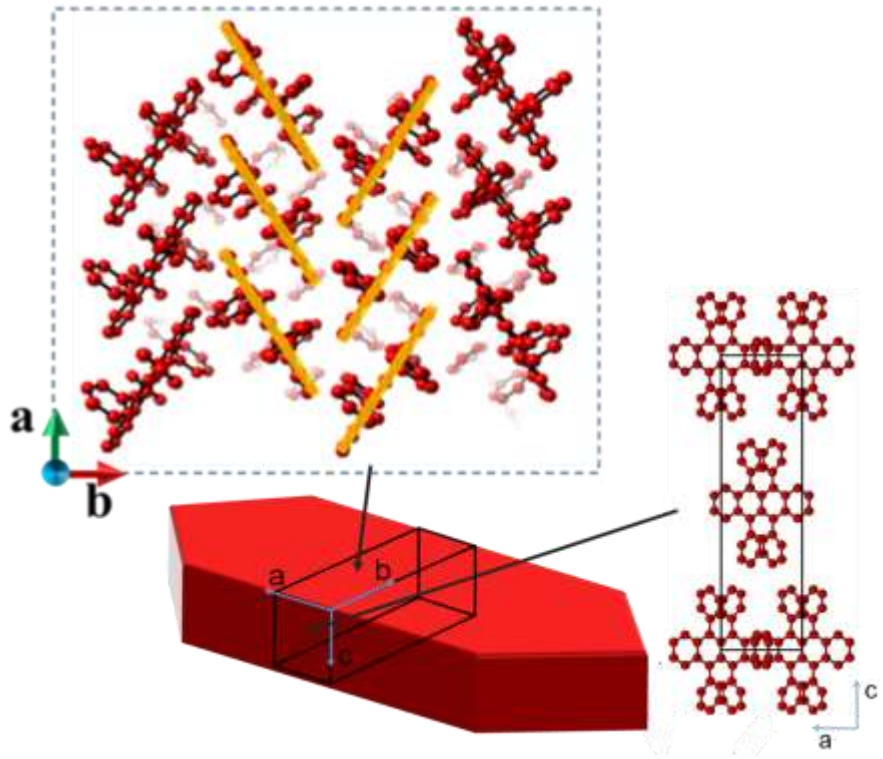

Figure 2-2 Diagram of the crystallographic packing of rubrene. The exposed (001) surface within the ab-plane is the largest facet which is produced in rubrene crystal growth. The herringbone structure is highlighted by orange sticks.

Table 2-1 Structural parameters of crystalline rubrene, values are for a crystal at a temperature of 293K. [32]

Parameter	Value
a[Å]	7.193(3)
b[Å]	14.433(5)
c[Å]	26.86(1)
Volume [Å^3]	2788.5(18)

2.1.3 Crystal growth

As stated, samples used in the studies presented within this thesis are grown using the vapour transport method.[37] Growth was undertaken by the group of Professor Kloc at Nanyang Technological University. Figure 2-3 shows the apparatus used in the growth of crystals. A temperature gradient is set up along a quartz tube. At the peak temperature the source material is sublimated and a flow of inert gas transports the material along the tube. At lower temperatures the rubrene molecules are deposited and crystallisation occurs. The temperature gradient acts to purify the crystals as samples containing defects are seen to be produced at different temperatures to the pure rubrene crystals.[38] This means that purity of a crystal can be inferred from its position along the growth chamber. This ensures that only high purity crystals with low defect incorporation are used.

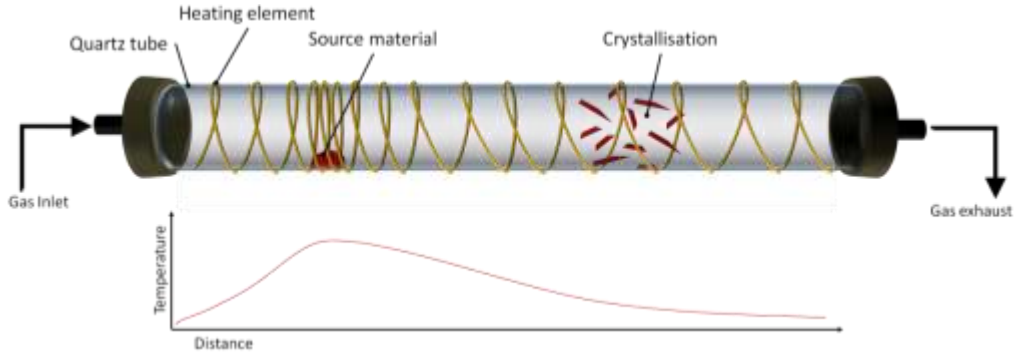

Figure 2-3 Schematic showing the process and apparatus used for the vapour transport deposition method of growing single crystal rubrene. Inert gas flows through a tube held at a temperature gradient. Sublimated source material is carried by the inert gas to a temperature region where deposition and crystallisation occurs.

2.2 Conduction within rubrene

To try and begin to unravel the complex nature of conduction and charge transport in rubrene I will here introduce the concepts of charge transport in organic crystals. I will then look at several studies focused on the transport of charge carriers within rubrene.

2.2.1 Bonding and conduction within organic materials

Within single crystal rubrene the molecules are bound by weak Van der Walls bonding which leads to weak intermolecular interactions. This is in contrast to the strong covalent bonds between the atoms of the individual molecules which lead to strong intermolecular interactions. This bonding in the case of conjugated molecules leads to a delocalisation of electrons over the entire molecule. To understand how this occurs, first picture the carbon atom which has electrons in each of the outer 2s, $2p_x$, $2p_y$ and $2p_z$ orbitals. When carbon-carbon bonds form, the

valence electrons of the carbon atom rearrange into new orbitals, producing a sp^n-hybridised basis set.[39] Figure 2-4 a) shows the formation of methane, CH_4, here the mixing of the carbon's 2s and 2p orbitals produces a sp^3 hybrid orbital. Each sp^3 orbital bonds with a 1s orbital from a hydrogen atom, this produces a σ-bond. This shows how the mixing of the s and p orbitals is able to bring about a different geometric configuration of the bonding.

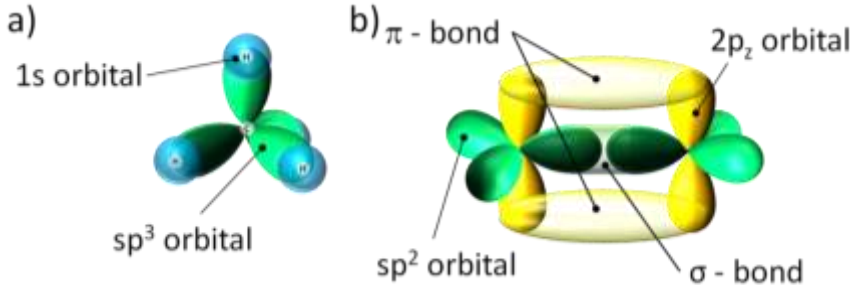

Figure 2-4 Figures showing the formation of π and σ orbitals. **a)** In CH_4, the four orbitals of the sp^3 hybridised carbon atom are directed towards the hydrogen atoms, each sp^3 orbital combines with a 1s orbital to form a bonding molecular orbital; four σ-bonds are created in a tetrahedral orientation. (Modified from [39]). **b)** C_2H_4 exhibiting the double bond nature of two sp^2 hybridised carbon atoms bonding. A σ-bond is formed between the sp^2 orbitals directed at each carbon atom, the p_z orbitals (1 from each carbon atom) overlap to form a bonding molecular π-orbital, (hydrogen atoms are removed for clarity).

For conduction to occur in organic materials it is well known that conjugation is required. Conjugation refers to the alternating sequence of single and double bonds in the molecule. Figure 2-4 b) exemplifies the importance of the carbon – carbon double bond within conductive conjugated molecules. This case shows the double bond character of ethylene, C_2H_4. Here sp^2 hybridisation of the carbon molecules produces three sp^2 orbitals within a single plane which form σ-bonds. The remaining p_z orbitals (one from each carbon atom) form a π bond which is out of the plane of the molecule.

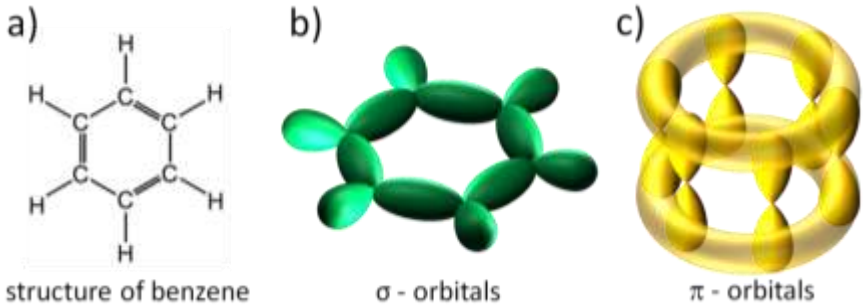

Figure 2-5 Electronic structure of a benzene ring, the basis of all aromatic molecules. **a)** structure of benzene ring, **b)** σ – orbitals of the molecule which all lie within a single plane, these are formed from the sp^2 orbitals of the carbon atoms. **c)** Superposition of the p_z orbitals forming π-bonding orbitals. This leads to delocalised charge density over the entire molecule.

When we now extend this principle to an entire conjugated molecule, such as benzene, C_6H_6 as in Figure 2-5, we see that the bonding molecular π-orbital leads to a delocalisation of the electron over the entire molecule. The benzene ring as seen in Figure 2-5 is the basis of all aromatic conjugated hydrocarbons, such as the highly conductive tetracene backbone within rubrene.

2.2.2 Coupling between molecules

The delocalisation of the π-electrons within molecules only informs us of half the story. As explained previously each molecule within a molecular crystal is held in place by weak Van der Walls forces, meaning there is little intermolecular interaction. For this reason the optical properties of molecular crystals strongly resemble those of isolated molecules. In order to have an understanding of conduction channels and their properties within molecular crystals we must understand the movement of charge between molecules. One important factor describing this is the interchain transfer integral 't'.[40, 41] Brédas *et al.* explain that "the interchain transfer integral expresses the ease of transfer of a charge between two interacting chains."[40] The transfer integral is direction specific. The main factor determining the transfer integral is the overlap of molecular electron wavefunctions within a specified direction. More details on transfer integral can be gained from da Silva *et al.*[41]

Figure 2-6 shows the electron wavefunctions for a rubrene molecule in its Highest Occupied Molecular Orbit (HOMO) and its Lowest Unoccupied Molecular Orbit (LUMO) these are the states which lie at either edge of the semiconductor band gap. For this reason the HOMO and LUMO are the most important molecular orbitals in the description of opto-electronic processes within the material.

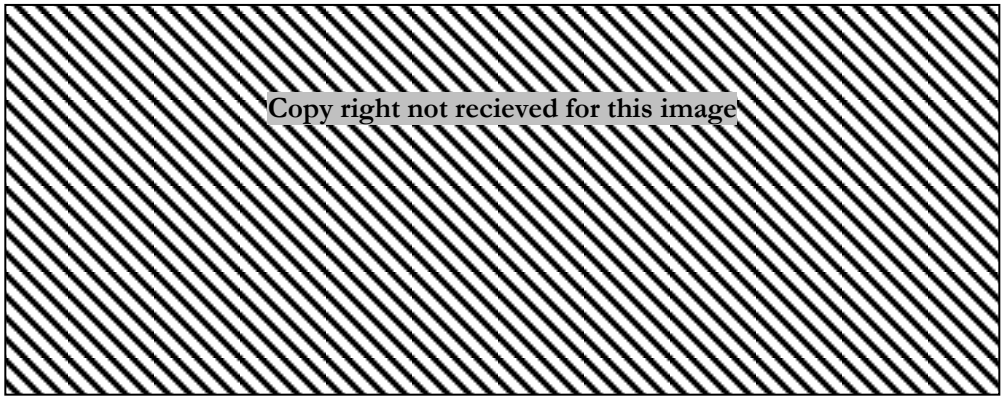

Figure 2-6 Electronic structure showing the molecular orbitals of rubrene calculated by density functional theory, **a)** chemical structure of rubrene, **b)** Molecular orbital of the highest energy occupied state, (Highest Occupied Molecular Orbital), **c)** Molecular orbital of the lowest energy excited state, (Lowest Unoccupied Molecular Orbital). [41]

Interestingly the HOMO and LUMO of both rubrene and tetracene are very similar in both shape and energy. This is clearly shown by Demétrio *et al.*,[41] who highlight that the large torsion angle between the phenyl rings and the tetracene backbone (measure to be ~85° in the crystal, [42]) strongly reduces mixing of the molecular orbitals between the backbone and side groups. This is likely to have a large effect of reducing the conduction of electrons laterally across the molecule (ie. from phenyl ring to backbone to phenyl ring).

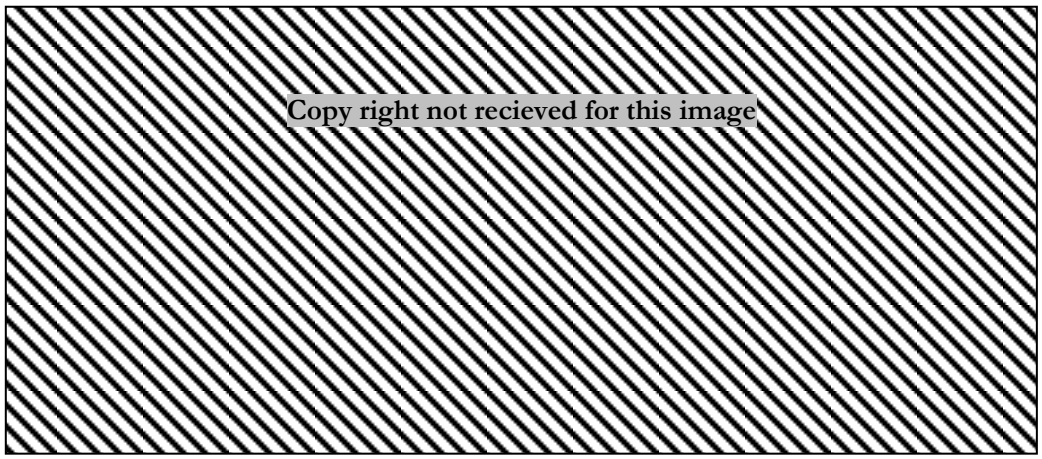

Figure 2-7 a) Illustration of the lattice parameters within the ab-plane of crystalline rubrene. The Short –axis and long axis displacements along the π-stacks in the a direction are also indicated. [41] **b)** Evolution of the calculated HOMO and LUMO transfer integrals as a function of displacement of two tetracene molecules stacked along the rubrene a direction with a π-stacking distance of 3.72 Å as found in the rubrene crystal. [41]

Within rubrene Demétrio *et al.*[41] have calculated a large value for the transfer integral along the a-axis with a smaller interaction calculated along the diagonal d direction (labelled in Figure 2-7 a)). The calculations for all other directions produced a negligible transfer integral. This leads to the understanding that movement of charge between molecules will occur in one of these two directions. Both rubrene and pentacene stack in a similar herringbone structure and in fact pentacene has a larger molecular density than rubrene with a shorter stacking distance between π-bonds. The larger transfer integrals of rubrene must therefore be triggered by the presence of the phenyl side groups. Due to the presence of the phenyl groups a long-axis displacement occurs in the crystal packing of the rubrene molecules. To see the effect of the long axis displacement Demétrio *et al.* calculated the change of *t* with respect to the displacement distance. This can be seen in Figure 2-7 b). Amazingly the displacement of rubrene, at 6.13 Å, coincides with an extreme of the transfer integral of both HOMO and LUMO. (Note that for the calculation of transfer integral in Figure 2-7 b) the side phenyl groups were replaced with

hydrogen atoms to avoid the major steric interactions upon displacement.) The increased charge transfer integral along a-axis is also believed to be due to the absence of short axis displacement between the adjacent molecules.

The results in this section describe the probability of charge transfer between molecules in respective directions. The discussed data leads to the prediction that charge movement through the crystal will be highly anisotropic, with high mobility in the a crystallographic axis. Any mobility within the b-axis will most likely be occurring due to charge transfer in the d direction. This anisotropic mobility agrees with measured results and is discussed further in the following section.

2.2.3 Mobility, μ

Characterisation of charge transport in organic semiconductors is usually by charge carrier mobility, μ, as with inorganic semiconductors. μ is defined in equation (2-1) where q is the charge in coulombs, τ , the scattering time of the carrier and m is the mass of the carrier.

$$\boldsymbol{\mu = \frac{q\tau}{m}} \qquad (2\text{-}1)$$

Equation (2-2) uses the carrier mobility to calculate the drift velocity of the charge carrier for a given applied electric field. It can be seen from this equation that the mobility effectively tells us how easy it is for a charge carrier to move through the given system under the influence of an electric field. Therefore an increase in mobility leads to a higher conductivity. From Equation (2-2) the units of mobility can easily be derived to give $cm^2(V{\cdot}s)^{-1}$.

$$\mathbf{J = qn\mu E \Rightarrow \nu_d = \mu E} \qquad (2\text{-}2)$$

Within Equation (2-2) J is the current density [$C{\cdot}cm^{-2}$], n is the volume density of charge carriers [cm^{-3}], E is the applied electric field [$V{\cdot}m^{-1}$] and ν_d is the drift velocity [$cm{\cdot}s^{-1}$].

2.2.4 Methods of charge transport in molecular crystals

Within solids there are two extreme types of carrier motion. The first, in which carriers move as a highly delocalised wave, in a broad carrier band, with a relatively large mean free path, is termed band-like. In the second, carriers are highly localised and move by hopping from site to site, being scattered at virtually every step.[39]

Band-like conduction is found in highly ordered, pure crystals. Often charge transport properties are highly dependent on crystallographic direction. As within this mechanism transport is

hindered by scattering, there is an inverse proportionality of mobility with temperature, T, as shown in Equation (2-3) where $n > 1$. This method of transport is depicted in Figure 2-8 a).

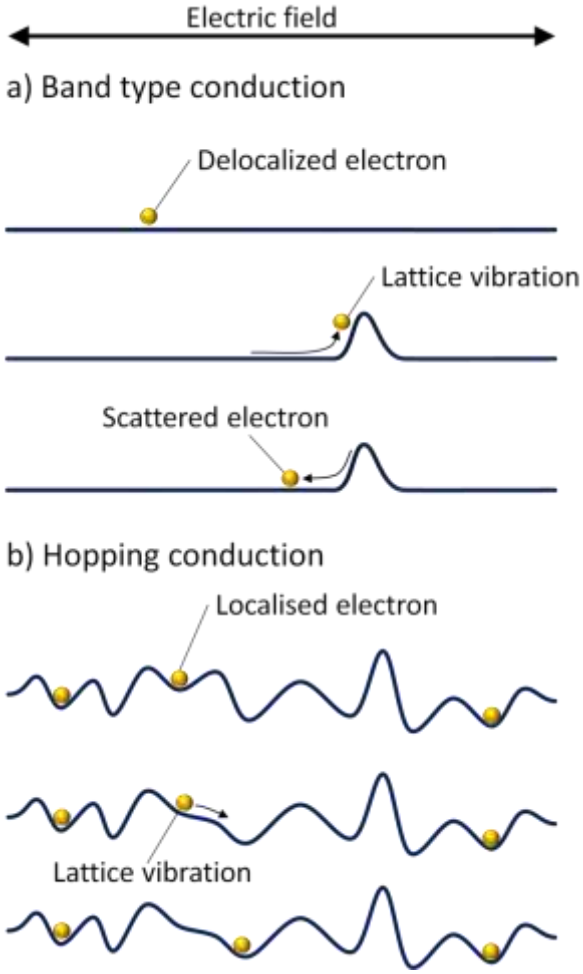

Figure 2-8 Two proposed methods of transport within rubrene, **a)** Band-like transport: In a perfect crystal, depicted as a straight line, a free carrier is delocalised, it moves as a plane wave without scattering. In a real crystal there is the existence of lattice vibrations or phonons that disrupt the crystal symmetry. These phonons scatter the electron acting to reduce the mobility. Lowering the temperature reduces the presence of lattice vibrations therefore increasing the mobility. **b)** Hopping transport: If carriers are localised due to defects, disorder, or self-localisation, then lattice vibrations are essential for carriers to move from one site to another. This is an activated process and therefore the mobility will increase with increasing temperature. (Modified from [39])

The Hopping transport mechanism is thermally activated, with carriers hopping discontinuously between adjacent molecules. This method of transport is often predominant in crystals with high disorder and defect content.[39] As this mode of transport requires the existence of lattice vibrations the mobility increases with temperature as expressed in Equation (2-4) where E is

the activation energy and k the Boltzmann constant. This method of transport it depicted in Figure 2-8 b).

$$\mu \propto T^{-n} \quad (2\text{-}3)$$

$$\mu \propto \exp\left(-E/kT\right) \quad (2\text{-}4)$$

The charge transport through molecular crystals is complex and cannot be defined as distinctly either hopping or band-like; instead it is likely to be a hybrid of the two. Due to relatively weak intermolecular interactions with organic crystals, it is often expected that the hopping regime should be dominant. This type of conduction though would be extremely unlikely to yield even the modest mobilities of lesser performing crystals such as anthracene, (μ = 1 $cm^2(V{\cdot}s)^{-1}$). It certainly would not produce the values which rubrene achieves, being quoted as high as 40 $cm^2(V{\cdot}s)^{-1}$.

The next section will go on to look at some of the important results which have been achieved in studying the mobility of rubrene. It is important to note that the mobility of rubrene which we discuss refers to holes only.

2.2.5 Mobility in rubrene single crystals

The standard measure of mobility in organic materials is the field effect mobility acquired by creating a field effect transistor (FET) at the surface of rubrene. An example of a rubrene FET is shown in Figure 2-9.

Chapter 3 written by V. Podozorv in "*Organic field-effect transistors*" goes into detail on the operation of single crystal OFETs, with the chapter concentrating on the case of rubrene.[43] I will here briefly describe the operation.

Free charge carriers can be introduced into organic semiconductors via chemical doping, photo generation or electrical injection. Rubrene has not been intentionally doped in measurements of the field effect mobility or in any studies within this thesis. Therefore mobile charges must be injected at the contacts; these are electrons or holes depending on the mode of operation. These mobile charges move along a field induced conduction channel between rubrene and a gate dielectric. Successful FETs have been produced using several fabrication methods including: conformal coating of a parylene gate dielectric by deposition on the surface,[28, 29] air gap FETs such as that depicted in Figure 2-9,[44, 45] and electrostatic attachment of Si/SiO_2 structures with evaporated contacts.[46] A large advantage of the air gap FETs which are produced on soft

stamps is that they can be applied, removed and reapplied without damaging the crystal. This allows multiple measurements on the same crystal in varying orientations and geometries. As contact resistance is not negligible a four probe technique is used to measure the resulting currents and voltage.[43]

Similar to most organic materials rubrene operates with a hole mobility greater than that of the electron mobility, the electron mobility of rubrene being smaller by two orders of magnitude reaching maximum values of 0.81 $cm^2(V{\cdot}s)^{-1}$.[47] For this reason rubrene is often termed a p-type semiconductor, this does not imply doping of the material as in inorganic semiconductors and is simply used to identify the material as having higher hole mobility. The understanding of the higher hole mobility often seen in organic materials is described by Kymissis in Chapter 2 of Organic Field Effect Transistors.[48] The majority of organic semiconductors are dominant hole carriers, this can be understood when thinking of the hydrogen atoms which surround the back bone. Kymissis explains, " the hydrogen atoms are less electronegative than the carbon backbone itself and lend some electron density to the delocalized pi-electron cloud. The electron rich conjugated molecule has difficulty accepting another electron, but is able to lose an electron with relative ease. As a consequence, positive charge carriers dominate". This clearly explains the dominance of hole transport within organic materials and in our case rubrene. A more detailed description of organic FETs can be gained from the books by *Kymissis* and *Podzorov*.[43, 48]

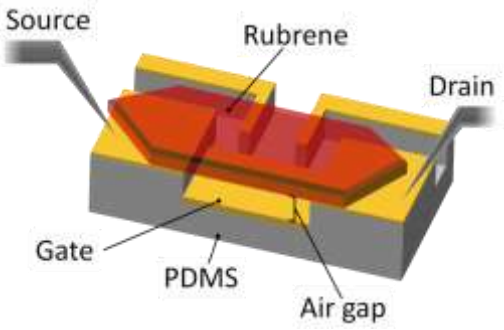

Figure 2-9 Schematic diagram of the FET used to measure the directional dependence of mobility within a rubrene crystal as reported in [50]. The flexible PDMS substrate allowed the contacts to be removed and re-applied in different orientations.

The Shockley FET model can be used to describe characteristics of a rubrene FET.[3, 49] This model has two regimes, the first in which there is a linear relationship between the gate voltage, V_G, and the source-drain current, I_{SD}^{lin}, for the constraint that $|V_G| \gg |V_{SD}|$. The second regime is a quadratic relationship in the saturation regime which exists when $|V_G| < |V_{SD}|$. These regimes are described by Equations (2-5) and (2-6) ,where W and L are the width and length

of the region between source and drain, V_T is the threshold voltage and C_i is the gate-channel capacitance of a FET per unit area. [3]

$$I_{SD}^{lin} = \frac{W}{L}\mu C_i V_{SD}(V_G - V_T) \quad (|V_G| \gg |V_{SD}|) \text{ [3]} \tag{2-5}$$

$$I_{SD}^{sat} = \frac{W}{2L}\mu C_i (V_G - V_T)^2 \quad (|V_G| < |V_{SD}|) \text{ [3]} \tag{2-6}$$

Figure 2-10 a) shows the measured transconductance of a rubrene FET which agrees in textbook fashion to the Shockley FET model.[3] Of note in Figure 2-10 a) is the nearly zero threshold voltage which indicates a low density of deep traps. The measurements of transconductance show excellent linearity of $I_{SD}(V_G)$ and $I_{SD}^{1/2}(V_G)$ which is of importance as Equations (2-5) and (2-6) assume the mobility is carrier density independent. The linearity therefore justifies the extraction of mobility from the data in Figure 2-10 a), this is shown in upper insert where the mobility plateau at the same value.

Figure 2-10 b) shows the dependence of mobility with temperature. Above 175 K there is an inverse relationship with temperature which, as discussed in Section 2.2.4 , implies the method of charge movement is via band-like conduction. This is in agreement with the large band widths which were predicted by da Silva *et al.* [41] The anisotropy of mobility within the two crystallographic axes of the ab-plane is also clearly seen. This agrees with the anisotropic transfer integral calculations discussed in Section 2.2.2 . The anisotropy of rubrene mobility is also shown in the work by Resse *et al.*[50] displayed in Figure 2-10 d) which clearly shows the increased mobility in the a direction.

The mobility plots for both axes in Figure 2-10 b) show that at temperatures below 175 K, mobility decreases exponentially with cooling. Podzorov *et al.* conclude that this is evidence of shallow trap dominated charge transport. [45] Figure 2-11 shows a qualitative diagram of the energy levels proposed by Podzorov *et al.* which describe this shallow trap dominance. They suggest that within the HOMO-LUMO gap there is the presence of localised states (traps). When *p*-type carriers are injected they fill these traps and are therefore unable to contribute to conduction. As *T* increases thermal excitation promotes these carriers from the shallow traps into the HOMO band where they can be utilised for conduction.

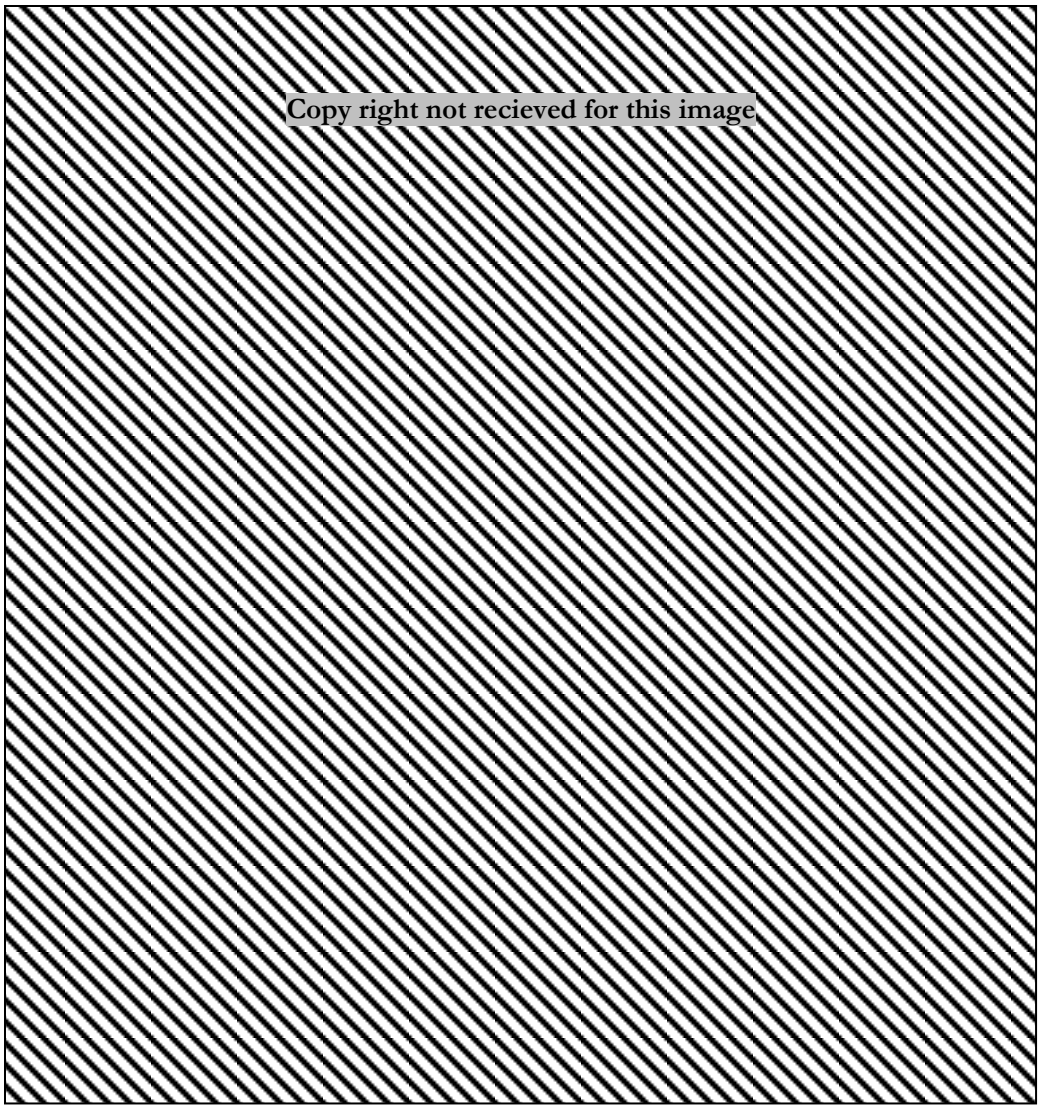

Figure 2-10 a) Measurements of rubrene single crystal FETs, both regimes show remarkable linearity allowing valid use of the FET equation to extract values for mobility.[3] **b)** The temperature dependence of field effect mobility and the threshold voltage measured along the a and b axes of rubrene crystals.[45] **c)** Temperature dependence of Hall mobility μ_H (blue solid circles) and the mobility extracted from the conductivity, using the density of charge carriers calculated from the gate-channel capacitance (black open circles).[51] **d)** Field effect mobility as a function of orientation, averaged over source/drain voltage from -2 to -10. [50]

Figure 2-10 c) shows the temperature dependence of the Hall mobility, μ_H, in comparison to the longitudinal FET mobility. The hall mobility is not dependent on V_G or the density of charge carriers and should therefore not be affected by the traps described in Figure 2-11 which reduce the effective FET mobility. Measurement of the hall mobility therefore gives us access to the intrinsic, trap free mobility. As can be seen the mobility has an inverse relationship with T. This indicates that charge transport on the surface of rubrene occurs via delocalised band-like transport over the entire temperature range studied. [51]

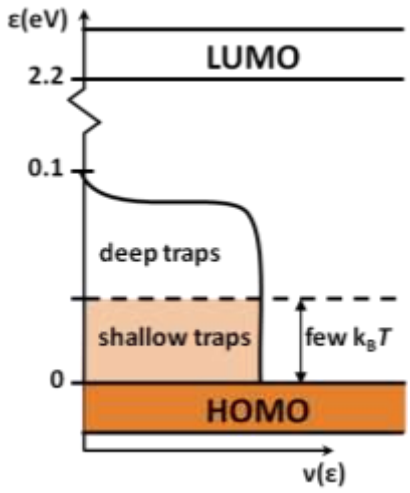

Figure 2-11 Schematic showing the proposed electronic states near the HOMO which lead to the dominance of shallow traps at low temperatures. [45]

The data presented within the previous section indicates that conduction within rubrene shows the signs of band-like transport. However it has been estimated that for $T > 100$ K the mean free path of carriers is comparable to the lattice constant, which contradicts the delocalised nature of band-like transport.[3, 19] A complete understanding of the conduction methods within molecular crystals and rubrene is beyond the scope of this work and is a complex issue which the community has not yet reached a firm conclusion upon. The previous section however gives an insight into the possible methods of transport in rubrene. Providing details of the considerations, as well as the observations, which have been made for the material. These factors are all of importance when considering the effect of material variation due to defect incorporation.

2.3 Photo physics of rubrene

2.3.1 Photoluminescence spectroscopy

Photoluminescence spectroscopy allows us to probe the energy levels of organic semiconductors using optical excitation. This is of particular interest as it allows us to characterise the energy gap between the HOMO and LUMO, as well as probing any in-gap states which exist. As has already been touched upon, and will be discussed further in Section 2.4 , knowledge of these states is important for the understanding and development of Field Effect Transistors and organic photovoltaic devices.

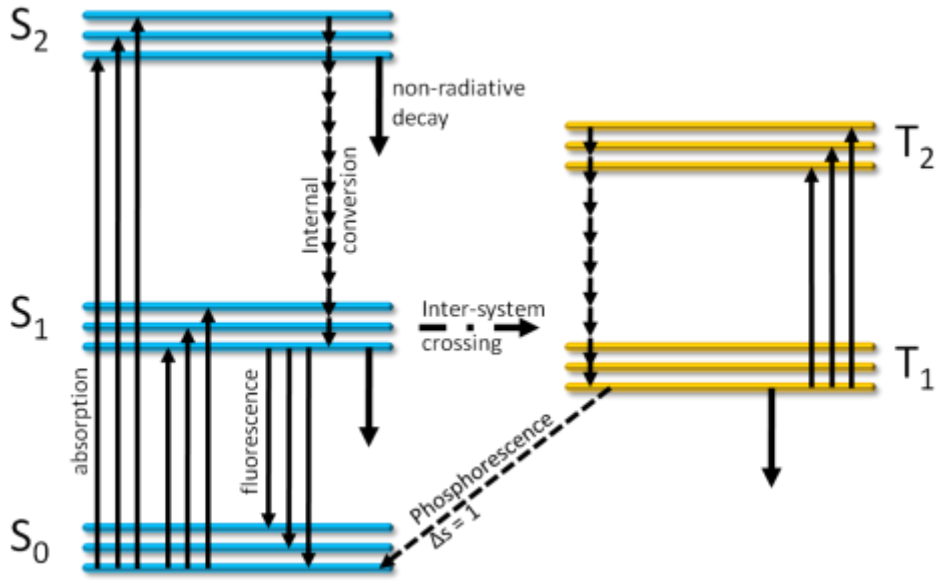

Figure 2-12 Jablonski diagram showing the radiative and non-radiative decay processes in a typical polyatomic molecule. S_n represents the singlet states of the molecule and T_n the triplet

The electronic excited states of organic molecular crystals strongly resemble that of the isolated molecule.[41] This means that the optical spectrum of the crystalline material also strongly resembles that of the isolated molecule. Figure 2-12 shows the relevant photo excitation and relaxation pathways within a molecule. Upon photon absorption a molecule is promoted into an excited state. Once in the excited state, the system quickly relaxes via vibrational relaxation to the lowest excited state, from where fluorescence can occur. It is also possible, if accompanied by a spin flip process, for inter system crossing to the triplet state to occur from the initial excited state. The inter system crossing process is of particular interest in rubrene due to the observation of singlet fission, this is discussed further in Section 2.3.5

Within polyatomic molecules there are several energetic modes which can exist at each electronic state due to vibrations within the molecule.[52] An example of these vibrations would be an oscillation of the carbon-carbon bond length. These vibrations are termed vibronic modes. Several vibronic modes can exist on a single molecule and are seen as series of discreet energy levels within each electronic state that follow a progression represented in Equation (2-7), where n represents the electronic level, V, the order of the vibronic level, and ω_v, the frequency of the vibronic mode. Figure 2-13 demonstrates how these vibronic states and the short time scale of vibronic relaxation lead to the stereotypical 'mirror image' of absorption and emission spectra.

$$E\left(S_n^V\right) = E\left(S_n^0\right) + V\hbar\omega_v \qquad (2\text{-}7)$$

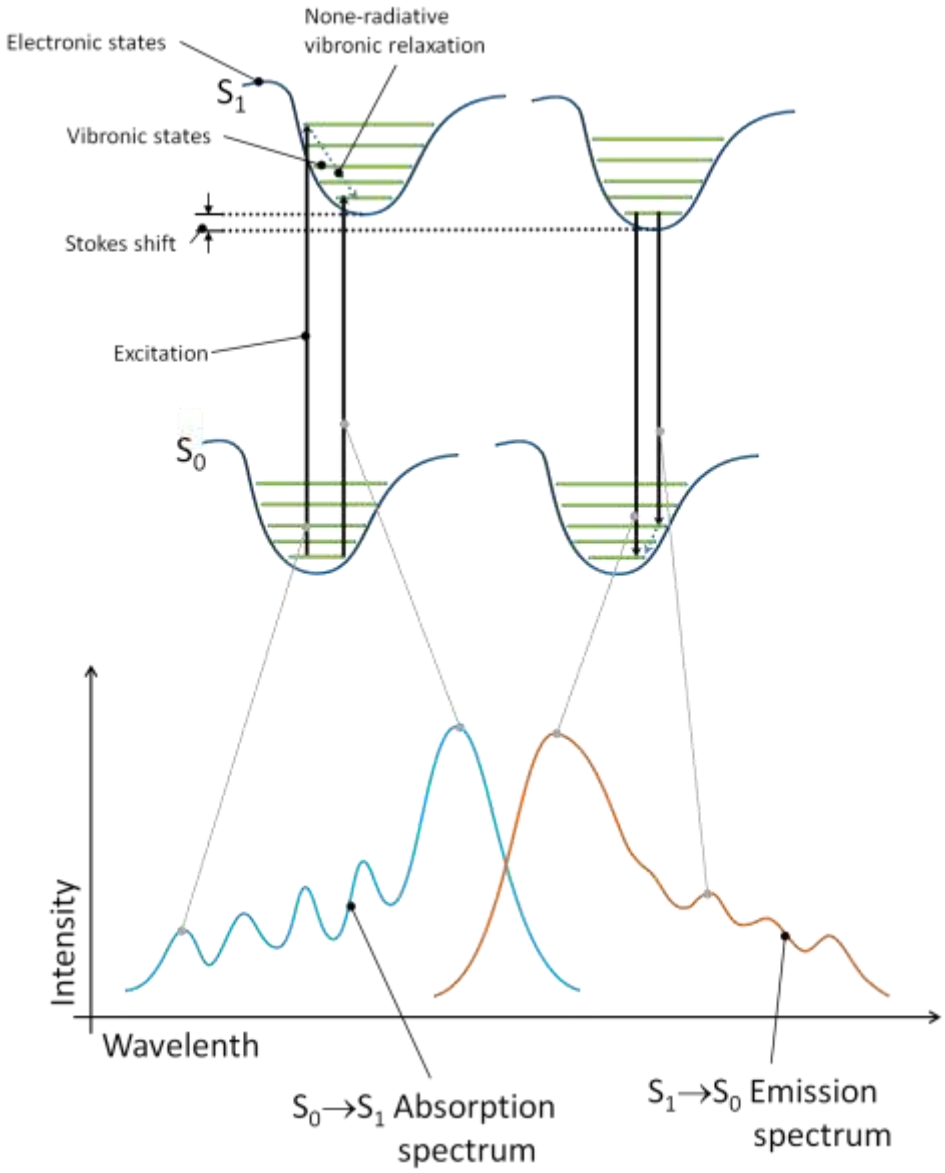

Figure 2-13 Schematic showing the transition between the ground and first excited state during excitation and emittance. It is demonstrated how the 'mirror image' of the absorption and emission spectrum occurs.

2.3.2 Two photon excitation

It is possible to excite a molecule via the interaction of two photons. In this case the transition energy must be equal to twice the energy of a single photon. As two photons are required the probability of excitation is proportional to the square of intensity. Excitation is therefore negligible except at the focus of the excitation beam. The excitation profile at this location can be mapped as a square of intensity and therefore the confinement of excitation is defined by how tightly the excitation beam is focused. This is discussed further for the experimental system

of this study in Section 6.2 . When the wavelength of the individual photon is not present in the absorption spectrum of the material, this has the benefit of allowing the excitation beam to penetrate the material. This allows excitation within the bulk away from any possible surface effects. It should be noted that the selection rules of two photon (2P) excitation are different from those of one photon (1P) excitation. The states at which the excitation couples to in 2P are not necessarily the same as those with 1P excitation. As relaxation of the molecule occurs on a time scale shorter than that of fluorescence, radiative decay occurs from the lowest vibronic level of the first excited state. This is the same for both 1P and 2P excitation (Figure 2-13). Therefore although a variation in the absorption spectra is expected, the emission spectra of both 1P and 2P excitations should be comparable.

2.3.3 Rubrene optical properties

There have been many studies which look at the optical spectra, both absorption and emittance, of rubrene single crystals.[30, 38, 53, 54, 55] There is however within the literature a diverse range of reported spectra. As will be discussed in the proceeding sections and there are several factors that will affect the shape of the optical spectra such as the introduction of defects to the sample. For this reason it is therefore imperative that sample preparation and handling is carefully considered and controlled.

Figure 2-14 shows the 'intrinsic' absorption and photoluminescence spectra for rubrene as measured by Irkhin *et al.*.[56] Due to the highly ordered and well orientated packing in single crystal rubrene the coupling of light to electronic states is highly anisotropic. To exhibit this Figure 2-14 shows spectra polarised along the a, b and c axes of the crystal as well as the spectra for amorphous rubrene.

As is clearly shown in Figure 2-14 a) the c axis is dominated by a peak at 2.22 eV which is not present in the intrinsic ab-polarised spectra. In most recorded data this peak is reported as being present in the ab-polarised emission. This peaks has been shown by Tavazzi *et al.*,[57], Mitrofanov *et al.*,[38] as Irkhin *et al.*,[56] as well as many others to be c-polarised emission. It is proposed that the presence of this peak in ab-polarised measurements is due to a 'leakage' of the c-polarised emission. The c component can be introduced into measurements of the ab-polarised spectra in several ways. The 'leakage' could be due to an erroneous c-polarised component introduced as light is focused, via non-normal acquisition with respect to the ab- plane. It could also be introduced due to light scattering at crystal imperfections. Again due to the anisotropic coupling of light there is also a polarisation dependence on the absorption length at 442nm. This

is quoted at 3μm, 2μm and 0.6μm for a, b and c polarisation respectively. At 532nm these values are 15μm , 6μm and 0.2μm respectively.[56]

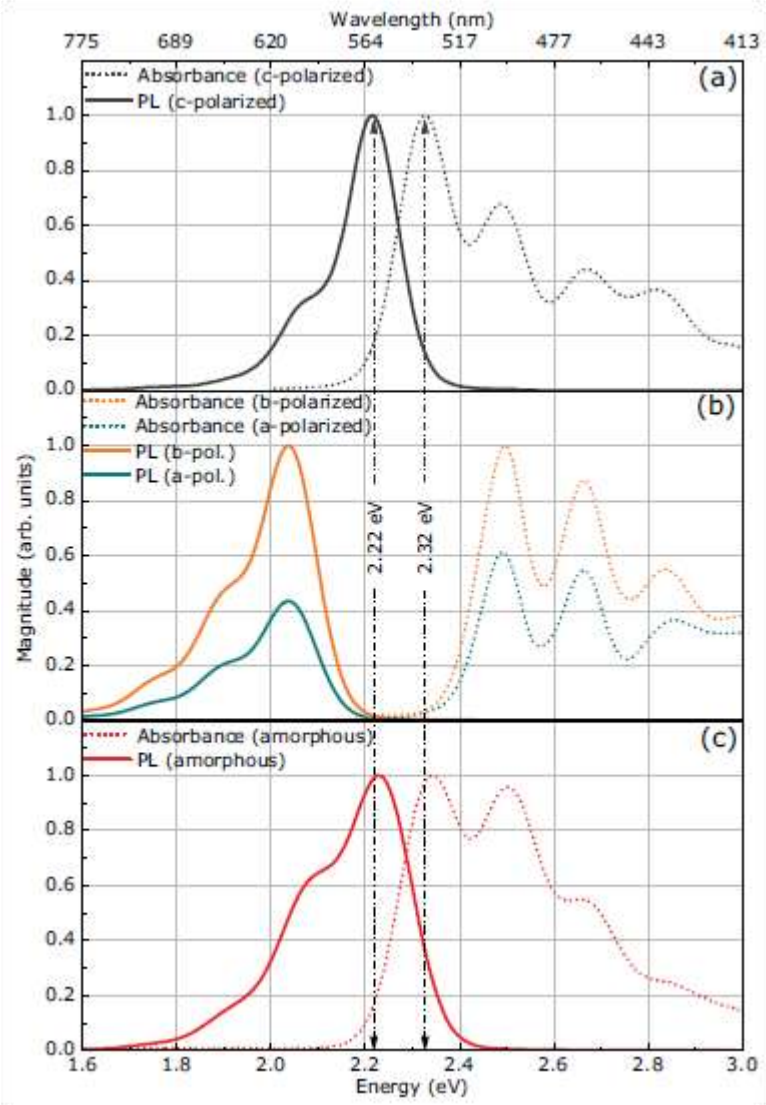

Figure 2-14 Intrinsic absorbance and PL spectra of rubrene. a) c polarised absorption and emission spectra, b) ab-polarised absorption and emission spectra. c) Spectra f amorphous rubrene, obtained by melting rubrene in the absence of atmospheric influences. [56]

One of the most notable differences in PL which is not evident in Figure 2-14 is the intensity difference of c-polarised emission. This is seen to be at least an order of magnitude more intense than light polarised in the ab-plane for the same excitation energy.

Further discussion of the photo luminescent spectra in the study of defects is discussed in Section 2.4 .

2.3.4 The exciton

Some of the most interesting properties of molecular crystals are those pertaining to the mobile excitation energy which results from photo excitation. This mobile excitation energy is termed an exciton. An extensive discussion of excitonic processes in molecular crystals is presented in a recent review by C. Bardeen.[58] The discussion of exciton interactions is an extremely prevalent one when considering rubrene, due to the unknown nature of rubrene's extremely long exciton diffusion lengths.[20, 21] I will here provide a basic description of the exciton followed by a discussion of the processes as presented by Bardeen. A more basic understanding of the types of exciton found in molecular crystals can be found in Chapters 2 and 8 by Fox.[59]

Upon photon absorption a molecule within the crystal of rubrene is excited into a higher energy state raising an electron from the Highest Occupied Molecular Orbit (HOMO) to the Lowest Unoccupied Molecular Orbit (LUMO) (analogous to the valance and conduction bands respectively in inorganic semiconductors). This involves the promotion of an electron from its ground state to its excited state leaving behind a positively charged vacancy, a hole.

The promoted electron and hole being oppositely charged feel a Coulombic force between them binding the two. It is this bound electron hole pair that is termed an exciton, the exciton is depicted in Figure 1. Within inorganic materials the exciton formed is predominantly a Wannier-Mott exciton which has a large radius with the constituent hole and electron able to orbit each other over a distance of many atomic sites; in comparison the excitons formed in organic materials, known as Frenkel excitons, are tightly bound to a single molecular site. The larger distance associated with the Wannier-Mott exciton leads to a binding energy that is often smaller than or on the order of k_bT which can be approximated to be 250 meV at room temperature.. Excitons in these materials are therefore short lived and the separation of the hole and the electron, known as charge dissociation, readily occurs. Due to the much smaller radius of the Frenkel exciton formed in organic materials the binding energy is much larger (between approximately 0.4 eV and 1.4 eV [60]) creating a strongly bound exciton. Further details of each of these types of exciton can be found in Chapter 4 of Fox.[59]

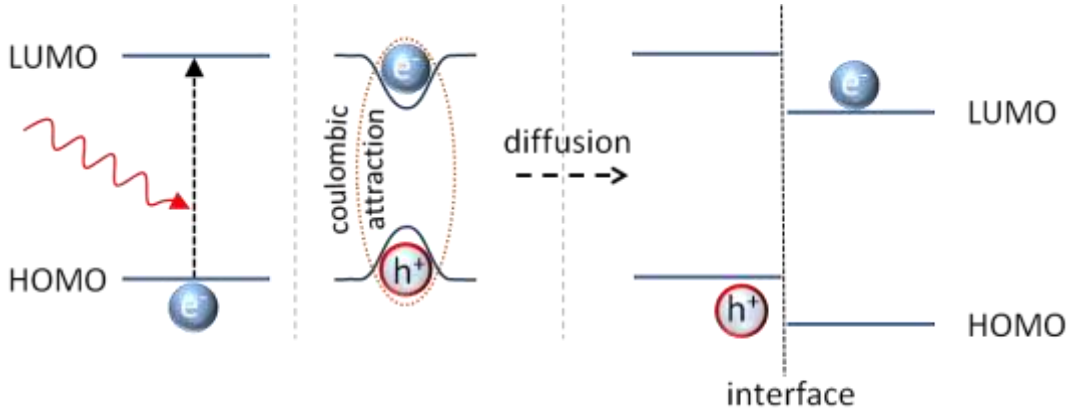

Figure 2-15 Cartoon depictinig photo-excitation creating an exciton (bound hole-electron pair) fllowed by diffusion to a initrface where charge seperation occurs.

Before the exciton can dissociate (ionise) and produce free charge carriers the binding energy must be overcome and therefore energy exchange must occur to the exciton. In inorganic materials thermal excitation can overcome the binding energy. Within organic materials the binding energy can be overcome at an interface where the difference in the energies of the adjacent HOMOs and LUMOs are sufficiently large enough as shown in Figure 2. This will lead to charge separation and is the basis of organic photo-voltaics, often termed excitonic solar cells. Further understanding of this generalised process can be gained from the review by Bernede,[58] and information directly related to rubrene can be gained from the work of Najafov *et al.* aswell as that of Karak *et al.*[61, 62] The exciton binding energy in rubrene has not been reported, though for comparison, in tetracene where the molecular orbital is similar to that of rubrene there is a binding energy of ~400 meV.[63] In order for charge separation to occur the difference in LUMO will therefore have to be on the order of 400 meV or higher.

If the exciton does not disassociate within the life time of the exciton the hole and electron will recombine relaxing the molecule down to ground state. This is a radiative process and produces the previously discussed luminescence. Other excitonic processes will be discussed further in section in the proceeding section. A general view of excitonic processes can be gathered from Fox chapters 4 &8,[59] and a detailed discussion of excitons in molecular crystals can obtained from Bardeen et al.[58]

2.3.5 Excitonic processes

In a recent review Bardeen discusses the excitonic processes which occur in molecular crystals.[58] In this section I lay out this discussion paying attention to the diffusion of triplet state excitons that are thought to facilitate the long exciton diffusion exhibited in rubrene. Within molecular crystals two types of optically accessible excitons exist, the Frenkel exciton and

the charge transfer exciton. The charge transfer exciton is a localised state, where the coulombically bound electron-hole pair can extend over several sites, the excitonic wave function of which resembles that of a hydrogen atom. [58] In the formation of a Frenkel exciton the states concerned are neutral and therefore the electron-hole pair exist on the same site.[58]

Initially the exciton will undergo diffusion. Newly created excitons are able to move through the crystalline matrix carrying their energy. The diffusion length of an exciton is of importance when designing organic photovoltaic cells, often termed "excitonic cells". It effectively defines the thickness of the active region at which an exciton can be created and reach the interface where ionisation can be induced and a current produced,[64, 65] (see Section 2.4.2).

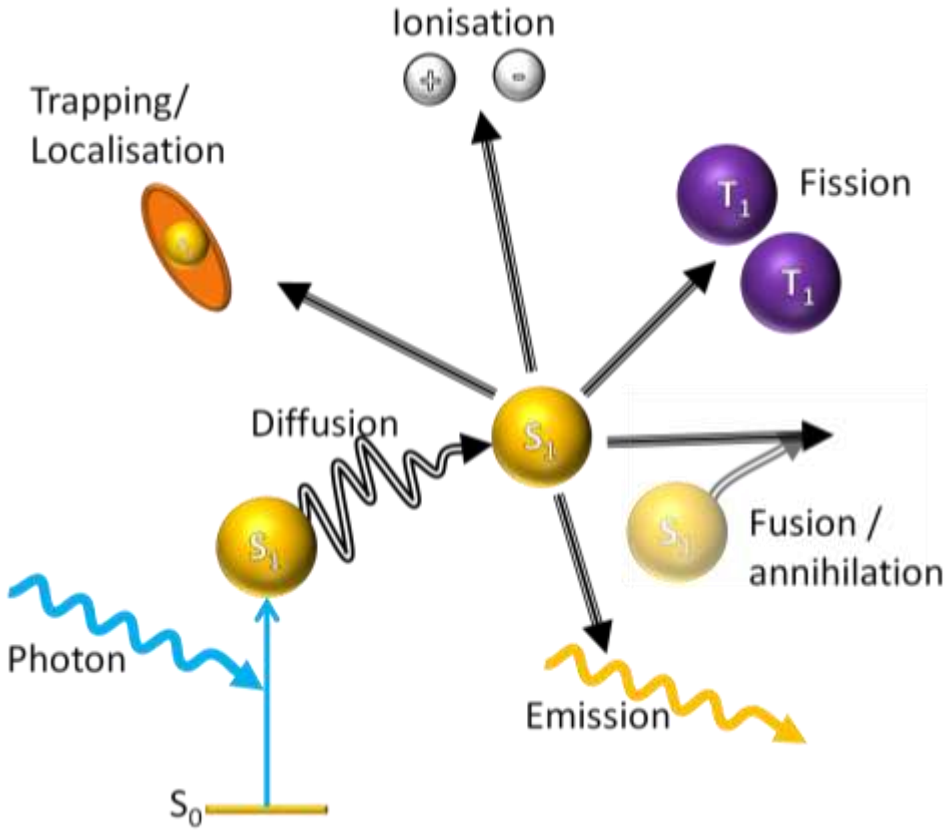

Figure 2-16 Schematic illustration of the dynamic processes that can occur after an exciton is created by the absorption of a photon, modified from [58]

Ionisation pertains to the dissociation of the molecular exciton into an electron and a hole. The formation of charge transfer or Frenkel excitons produces stable species with a relatively large binding energy (0.5 eV or higher, [58]). If the exciton has enough energy it may auto ionize, alternatively it can diffuse until it meets a component which will stimulate dissociation. The understanding of how molecular interfaces stimulate exciton dissociation is one of interest.[66]

Some recent studies discussed by Bardeen,[58] imply the direct creation of high mobility free charge carriers. This though is in contradiction to theoretical calculations and early work on anthracene and other molecular crystals. Photoconductivity experiments by Najafov *et al.* on rubrene single crystals certainly point to the bound exciton being the majority species formed after photo excitation.[21] Bardeen states "To date, there has not been a consistent effort to perform optical measurement and transient conductivity experiments under the same experimental conditions". The situation pertaining to the nature of the exciton and its dissociation is therefore an unclear one and one which needs to be addressed.

Figure 2-16 depicts the most common processes which occur after a photon is absorbed and an exciton created. As discussed by Bardeen these are namely diffusion, trapping, ionisation, fission, fusion and emission.

The emission of an exciton refers to the radiative decay of the excited state as discussed in section 2.3 .

Trapping and localisation are able to occur when, in some cases, the initially excited state has Frenkel character but rapidly relaxes into a lower energy state, with a more localised charge transfer character. This process is termed "self-trapping".[58] Trapping can also occur when an exciton interacts with a defect within the material. This can allow for an excitonic state to exist which is not within the delocalised exciton band structure and therefore "traps" the exciton at the site of the defect.

Fusion can occur due to the high density of excitonic sites within a molecular crystal, which make it possible for excitons to encounter each other. When an encounter occurs, it is possible for the excitons to fuse into a single high-energy exciton. The resultant exciton can then rapidly relax back down to its lowest singlet state. This effectively removes the presence of both excitons involved and is therefore often referred to as annihilation, resulting in a rapid decay in the excited state population.[53] It is also possible to form the existence of new, longer living, higher energy state via exciton fusion.[39]

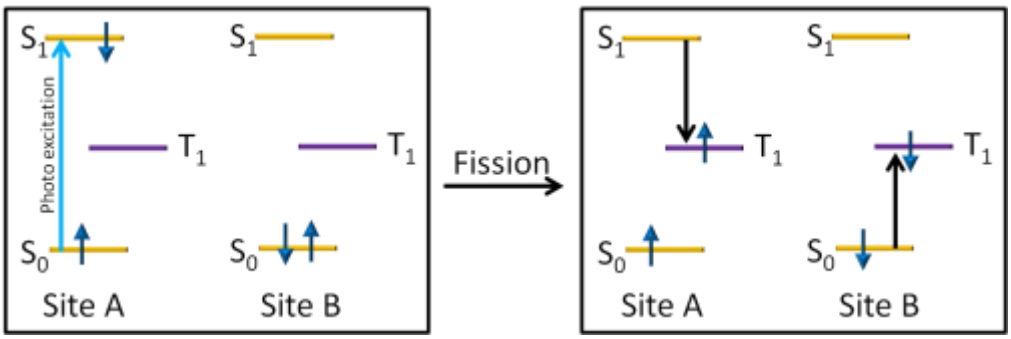

Figure 2-17 Singlet fission: **Left,** The site on the left undergoes an initial excitation to S_1. **Right,** The excited excitonic site shares its energy with a second site creating a T_1 state on each site. Note for conservation of energy this requires for $\boldsymbol{E(S_1) \geq 2 \cdot E(T_1)}$. Blue arrows indicate the spin direction of the respective electrons. Modified from [67]

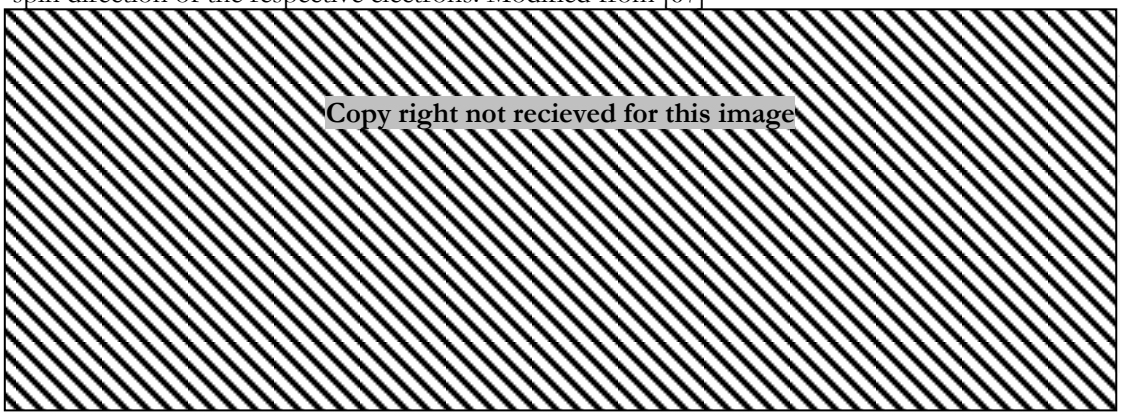

Figure 2-18 Measurements of the long exciton diffusion within rubrene, it is believed the long excitonic diffusion is due to the fission of singlet state exciton producing long lived triplet excitons. **a)** Contour plot showing the distribution of PL after localised excitation at the surface of rubrene, a direct measurement of excitonic diffusion. Intensity distribution of excitation light (top) and the PL (bottom).[20] **b)** Distribution of intensity for the excitation laser (full red circles) and PL (open blue symbols) along b axis for the experiment shown in a) [20] **c)** Schematic of the experiment undertaken by Najafov *et al.* which used the polarisation and wavelength dependence on absorption coefficient and therefore depth of exciton photo generation to show an exciton diffusion in the c plane of 2-8 μm. [21]

One of the most interesting excitonic processes pertaining to rubrene is the fission of singlet states. The 1→2 reaction in which a singlet spontaneously splits into a pair of triplets, has been observed in several molecular crystals such as anthracene, tetracene, pentacene, isobenzofuran, and polyenes.[58, 68, 69, 70, 71] Figure 2-17 schematically shows the exciton fission process as described by Smith and Michel who in their recent review discuss the process of singlet fission in several organic materials.[67] The singlet fission process is spin allowed and can be thought of as two molecular sites with electrons of opposing spins (↑↓, ↑↓), where one site is in its ground state, transferring to two excited states with the electrons within each site having parallel spin (↑↑,↓↓). This is depicted by the blue arrows in Figure 2-17. In order for the conservation of

energy it should be noted that the energies (*E*) of the respective excitons must fulfil the condition $(S_1) \geq 2 \cdot E(T_2)$. One of the major benefits of singlet fission is in the harvesting of energy within an excitonic photovoltaic cell. Within these devices a photon whose energy is well above the band gap will non-radiatively decay to the band edge losing the excess energy to the 'phonon bath'. As proposed by Bardeen if the high energy exciton could undergo fission creating two near band edge excitons these could in turn produce an extra-hole pair. As Bardeen discussed a similar idea could be applied to the fusion of excitons created by below band gap photons promoting them above the band gap, this therefore leads to a more complete and efficient use of the entire solar spectrum.

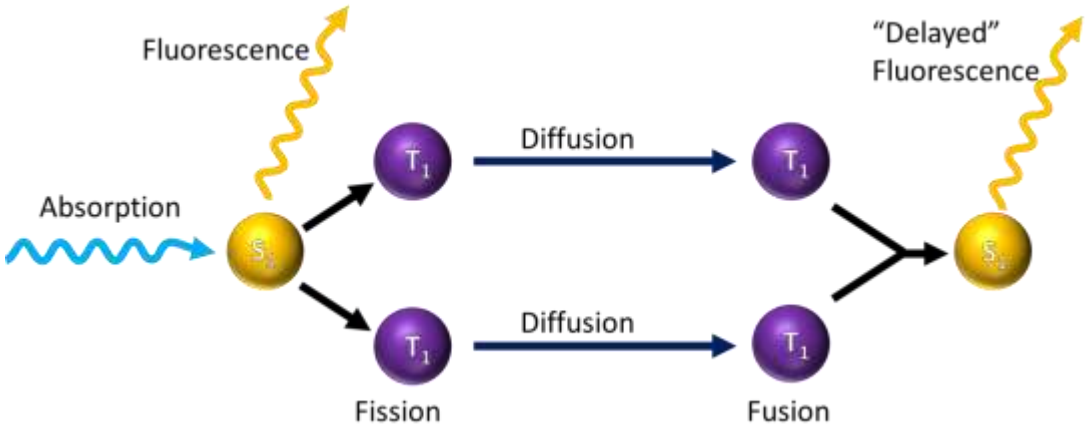

Figure 2-19 Schematic showing how the fission of singlet excitons can lead to long diffusion lengths when accompanied by Triplet fission then leads to delayed fluorescence. Modified from [58]

As previously referred to it has been shown that rubrene has an unusually long exciton diffusion length. Figure 2-18 details two experiments which have shown evidence of this. Figure 2-18 a) and b) both show data from the experiments by Irkhin and Biaggio which directly images the exciton diffusion by capturing on a CCD the distribution of photoluminescence intensity after localised excitation.[20] They concluded an exciton diffusion length of 4.0±0.4 μm in the b-axis of rubrene. Figure 2-18 c) shows a schematic of the experiment undertaken by Najafov *et al.* which measures the photocurrent, a function of the number of excitons reaching the organic semiconductor interface, produced by light incident at different polarizations. As the absorption coefficient is polarisation dependent the depth at which exciton generation occurs can be modulated. Najafov *et al.* have modelled the depth at which exciton generation occurs and shown that exciton diffusion along the c-axis must exist at a length of 2-8 μm.[21] It is proposed by both Irkhin and Najafov that the long exciton diffusion is due to the fission of singlet

excitons upon photo excitation creating two triplet excitons. As the direct relaxation of the triplet state to the ground state is spin forbidden the triplet exciton has a longer life time than the singlet being on the ps and ms scale respectively.[72] Figure 2-19 shows how the fission of a singlet exciton leads to two long lived triplet states; due to the long life time of these states they are able to diffuse longer lengths than the short lived singlet states. Figure 2-19 also predicts the presence of delayed fluorescence; this is seen to exist in rubrene as shown by Najafov *et al.* in Figure 2-20. The insert in Figure 2-20 shows the time dynamic of the PL at 610nm. There is an instantaneous maximum due to short lived singlet states followed by a longer time scale delayed fluorescence. The main plot shows the instantaneous spectra recorded a few ns after excitation and the delayed spectra recorded at a later time. This delayed fluorescence shows an absence of emission at 550 – 580 nm. This implies that there is some variation in the recombination of short live singlet excitons and singlet excitons formed from triplet fusion. Ma *et al.* have also looked at the time dynamics of photoluminescence in rubrene and also conclude the existence of the singlet fission process. Ma *et al.* also suggest that the production of triplets may be formed from an upper excited state.[55] The schematic shown in Figure 2-21 details the energy levels in rubrene used in the formation of triplet states as presented by Ma *et al.*. They show that due to the energy levels existing in rubrene the fission of the lower excited state will only occur when thermally assisted. It is also possible for more energetic singlet states to undergo fission with excess energy being lost as phonons within the material. Of relevance in this diagram is the energy levels of the S1 and T1+T1 states, details on the other energy levels can be gained from the work of Ma et al.[55]

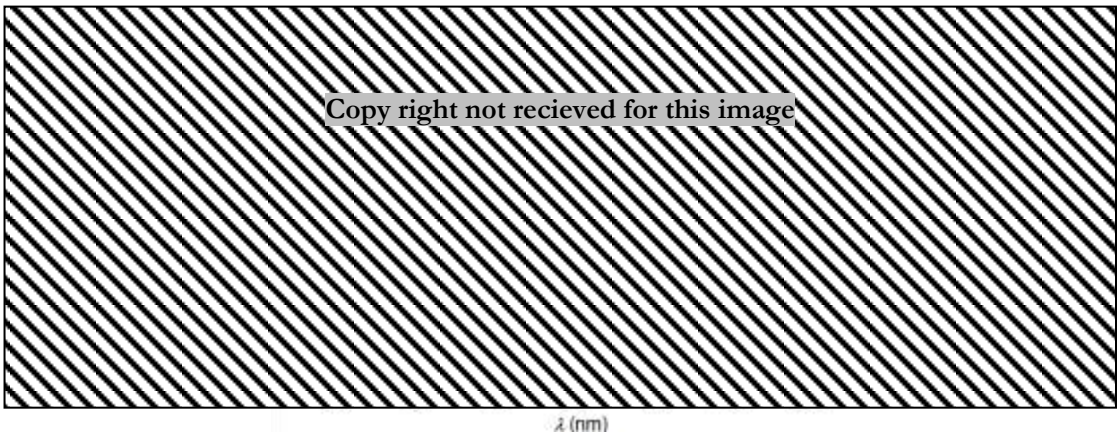

Figure 2-20 Time resolved photoluminescence in rubrene. Time resolved PL measured after a 20ps pulse duration. Green circles shows peak PL at a few ns, Red triangles show the PL integrated over the range 0.7-2μs. The inset shows the time dynamic measured at 610nm. [21]

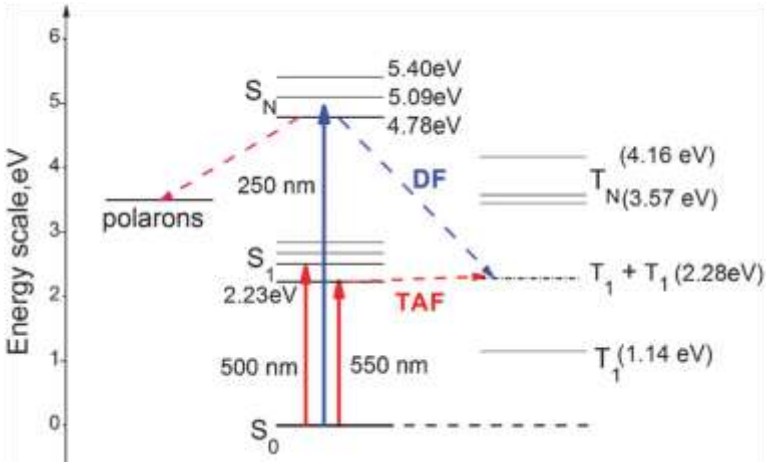

Figure 2-21 Energy levels within the rubrene single crystal showing transitions which can produce triplet excitons. DF = direct fission, TAF = thermally activated fission. [55]

2.4 Chemical alterations to the properties of rubrene

2.4.1 Introduction of defects into the material

In the previous sections I have briefly touched on how the presence of defects can affect the properties of rubrene, for example by the introduction of electronic states or localisation and trapping of excitons. In the following section I will discuss the introduction of defects due to environmental conditions, specifically the oxidation of rubrene. The effect of the ambient environment has been reported by many researchers, including myself, to affect the optical and electronic properties of rubrene. [22, 23, 30, 38, 73, 74, 75, 76]

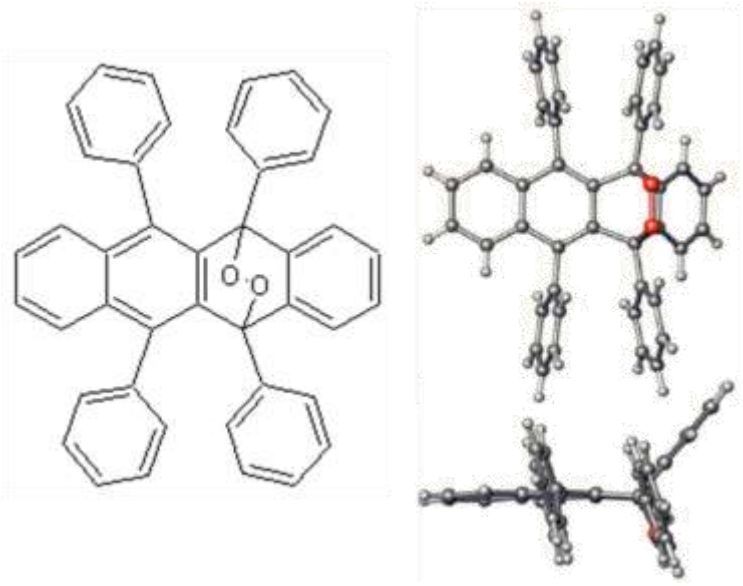

Figure 2-22 Chemical structure and 3D model of rubrene endoperoxide, $C_{42}H_{28}O_2$. [38]

Rubrene is known to readily oxidise when in the solution or amorphous phases, this is accelerated by the presence of light.[33, 77] It has been shown that oxidation of rubrene forms a rubrene peroxide $C_{42}H_{28}O_2$. The most common form of this molecule is produced by the incorporation of two oxygen atoms within one of the central benzene rings as shown in Figure 2-22. The incorporation of the oxygen molecule at this site on rubrene considerably alters the molecular backbone producing a bend of 49.4°.[38] If the oxygen molecule binds elsewhere forming a different form of oxide the structural variations of the molecule will vary. The steric deformation of the molecule is thought to impede its inclusion within the crystalline matrix of rubrene. For this reason rubrene crystals are not seen to oxidise to the same extent as the solution or amorphous phase, nevertheless, oxides have been shown to be incorporated.[22, 30, 78] The deformation of the molecule and breaking of the conjugation due to the incorporation of oxygen will disrupt the delocalisation of the π molecular orbital and therefore change the electronic states of the molecule. If this produces a state which lies within the HOMO-LUMO band gap it should produce a spectral signature within the photoluminescence spectrum. This is proposed by Mitrofanov *et al.* and supported by their experimental data which is summarised in Figure 2-23.[30, 38]

Mitrofanov *et al.* undertook photoluminescence spectroscopy using both continuous wave single photon excitation ($h\nu$ = 3.815 eV) and pulsed two-photon (2P) excitation ($2h\nu$ = 3.30 eV). For samples which were held in vacuum, (prevented from interacting with the environment,) they saw typical spectra for rubrene single crystals. Spectral bands located at: 2.18 eV (denoted band I) along with related vibronic bands assigned to carbon-carbon bond stretching, ($E_{I-n} = E_I - n\hbar\omega_{c-c}$, 2.00 and 1.83 eV) ; 2.11 eV (denoted band II) with a vibronic band at 1.93 eV; and a final band (III) at 2.05 eV. The temperature dependence of these was such that band I dominated at lower temperatures decreasing by at least 3 orders of magnitude as the temperature increased from 20 – 300 K. At T > 70 K band II became prevalent in the spectra followed by a temperature dependence similar to band I, and at T>100 K band III dominated the spectrum. This is the characteristic spectra for 'as grown' samples of rubrene such as those used in the experiments. Mitrofanov *et al.* studied samples which had been exposed to the ambient environment. As rubrene peroxide has been reported to form at the surface of rubrene crystals 2P spectroscopy was undertaken at a depth > 1μm. This ensured the location being studied had not been contaminated and the spectra measured were not influenced by any oxygen incorporation. The bulk spectra showed the same spectral features as those seen on the vacuum held samples, confirming the spectra was characteristic for that of pure rubrene. PL spectra were then acquired at the surface of samples held in an oxygen atmosphere, at normal pressure (held

at 100℃ for 14 hrs). The spectra of these samples showed a substantial difference to that of pure rubrene; band I and its vibronic series were seen at a reduced intensity accompanied by a series of bands (I') shifted by ~40 meV. Strong emission was also seen as a new band became present at 1.92 eV (denoted O). This band was seen to dominate the spectra of the oxidised samples above 200 K while band III was strongly suppressed. These results are presented in Figure 2-23 a). Figure 2-23 b) shows how the O band was only present at the surface of oxidised samples and was not seen within the bulk of samples held in either an oxygen rich or vacuum atmosphere. The O band was also not present in the spectra acquired from the surface of vacuum held samples. The 2P excitation depth profile (Figure 2-23 b)) clearly shows an increase in the intensity of band O as excitation moves towards the surface of samples held in an oxygen atmosphere. Mitrofanov *et al.* conclude that these results show the presence of an oxygen-related state providing a recombination path for molecular excitons which results in the emission of the O band. They hypothesize that this band gap sate is due to; a rubrene molecule perturbed by a neighbouring oxygen molecule; a rubrene peroxide molecule formed after reaction with oxygen; or a rubrene molecule perturbed by the presence of a rubrene peroxide molecule.

Mitrofonav *et al.* present further work,[38] which looks at the effect of sample preparation on the oxygen-related state. Figure 2-23 c) (i) shows the PL spectra of rubrene crystals grown in the presence of different gases. It shows how the oxygen state can be incorporated during growth if oxygen is present. However, when grown in the presence of only pure argon no O band was measured. Figure 2-23 c) (ii) shows how the spectra vary with position in the growth chamber; it shows clearly how the incorporation of defects and impurities is dependent on the growth position in the continuous temperature gradient. The highest quality crystals are grown at a specific temperature and can therefore be selected from the relevant position within the growth chamber. Figure 2-23 d) shows how the post growth incorporation of the oxygen state is dependent on the quality of the crystal. A sample containing crystallographic defects seems to more readily incorporate the oxygen than a pure high quality crystal grown by vapour transport. Mitrofanov *et al.* also report that some samples not exhibiting the O band after growth remained the same after at least a year in normal ambient environment. They conclude that, due to the different configuration of the rubrene peroxide molecule, for it to be incorporated within the crystal some sort of vacancy, to allow steric deformation, must be required. They suggest a vacancy provided by a structural defect would allow the required steric relief for incorporation of a peroxide molecule.

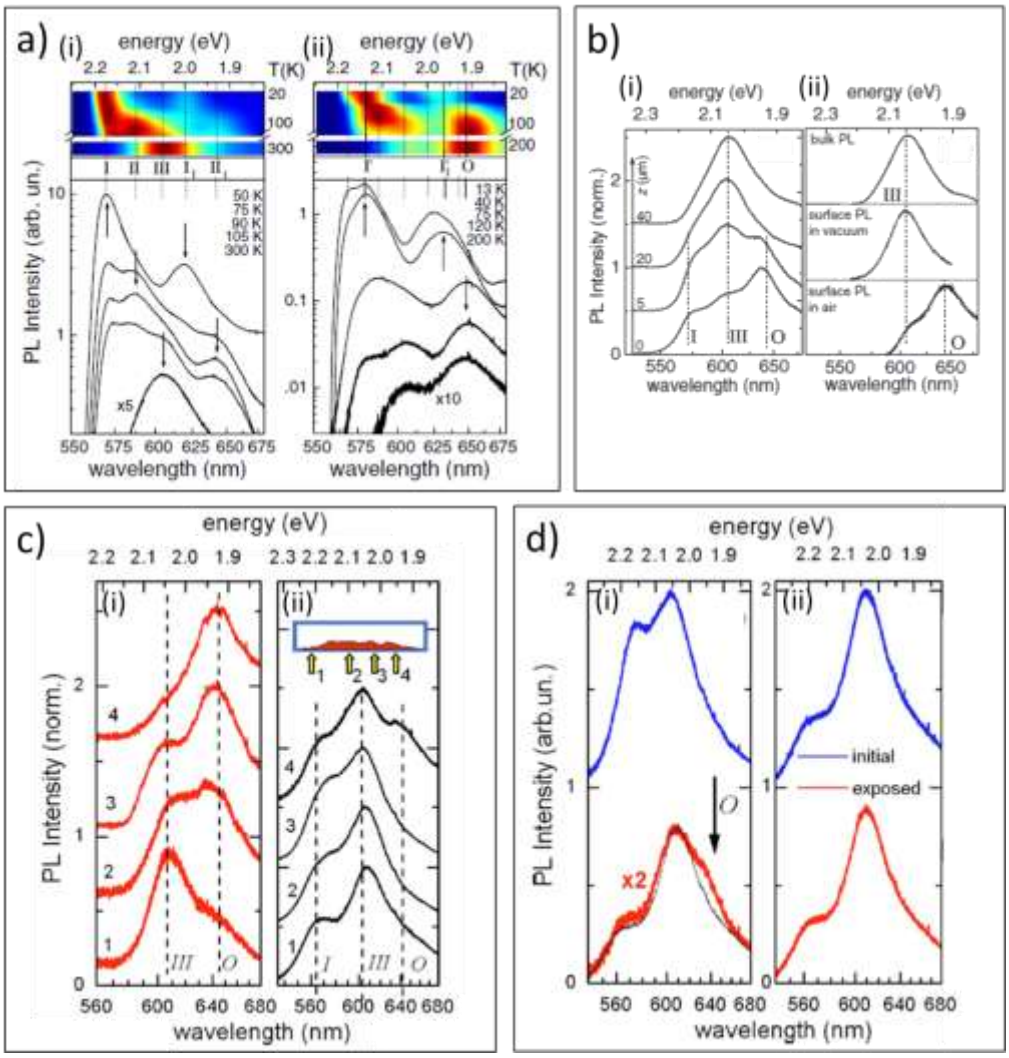

Figure 2-23 Data presented by Mitrofanov *et al.* which indicates the formation of an in-gap state induced by the incorporation of rubrene peroxide both at the surface and within the bulk of crystalline rubrene depending on sample treatment. **a)** PL at varying temperatures for, (i), an as grown crystal held in vacuum and, (ii) an oxidised rubrene crystal contained in a sealed capsule containing oxygen at a normal pressure. [30] **b)** (i) PL spectra measured using two photon spectroscopy at different depths within a rubrene crystal which has be left in air. (ii) Bulk spectra compared to surface spectra of a sample stored in vacuum and in air.[30] **c)** (i) PL spectra of samples grown via vapour transport in different gases, 1) pure argon gas, 2,3) unintentionally contaminated argon gas, and 4) an argon/oxygen mixture. (ii) PL spectra of crystals which originated from different locations within the growth chamber, the respective locations shown by the insert are at x = 7, 20, 30 and 40 mm with gas flowing in the direction of increasing x. The temperature gradient of the growth chamber was such that, $T_1 > T_2 > T_3 > T_4$.[38] **d)** PL spectra recorded before and after 7 hours of laser beam exposure in air for a commercially synthesized crystal containing defects (i), and a high quality vapour transport grown crystal (ii). The PL of the exposed commercial crystal has been multiplied by 2 for clarity.[38]

It should be noted that there is debate in the literature as to the origin of the emission at 650 nm which is the location of the O band reported by Mitrofanov *et al.*.[30, 38] Chen *et al.* have recently reported that the band is not due to the presence of a chemical defect, but rather a structural deformity within the crystal due to the presence of amorphous phase rubrene and does not require the presence of any additional chemical component.[79] As with Mitrofanov *et al.* they show the variation of spectra due to position in the growth chamber, but attribute the difference in spectra to structural variance. They rule out the interaction of oxygen as PL measurements were taken from samples which had not been removed from the Ar atmosphere in which growth occurred. To show the relationship between the intensity of the 650nm luminescence and the amount of amorphous phase in a sample Chen *et al.* measured the PL of a melting rubrene crystal. The sample was held in an inert stream of gas as the temperature increased to 380℃ and was returned back to room temperature. During this process the sample changed from a well faceted single crystal to a molten amorphous bead. This was accompanied by a spectral change, moving from being dominated by the peak at 615 nm to 650 nm emission. From these findings Chen *et al.* conclude that the 615 nm and 650 nm PL emission peaks are attributed to radiative relaxation of the same molecular exciton but are emitted from different phases. They suggest that within crystals showing the 650 nm emission amorphous inclusions exist which trap diffusing triplets, increasing the probability of triplet fusion. This results in an increased density of singlet excitons in an amorphous environment which then radiatively decay. The red shift from 615 to 650 nm is attributed to an increased density of rubrene molecules in the amorphous phase.

2.4.2 The effect of surface functionalisation and defect incorporation on electronic properties.

As well as the incorporation of defects within the material, the effect of interfacial chemistry has been studied and shown to affect the electric and electro-optic properties of rubrene. The work of Najafov *et al.* has shown that both the conduction and exciton dissociation properties of rubrene at the surface are sensitive to the presence of additional material layers. In this study Najafov *et.al* showed that almost 90% of the photo-electric current is accounted for by dissociation of exctions at the surface and therefore any change in surface chemistry will have a great effect on the efficiency of exciton dissociation.[21] Figure 2-24 a) shows the experimental results of Najafov *et al.*. These results show that coating the crystal surface with a thin layer of an optically transparent dielectric can drastically alter the photocurrent. These coating are known to form a trap-free interface with organic crystals.[19, 80] In the case of the dialectic parylene-N the photocurrent dropped from 100 nA to 10 nA. Conversely to this, deposition of parylene-D

resulted in a 1.5 increase in photoconductivity. This shows the importance of understanding the surface environment and how it affects excitons within rubrene.

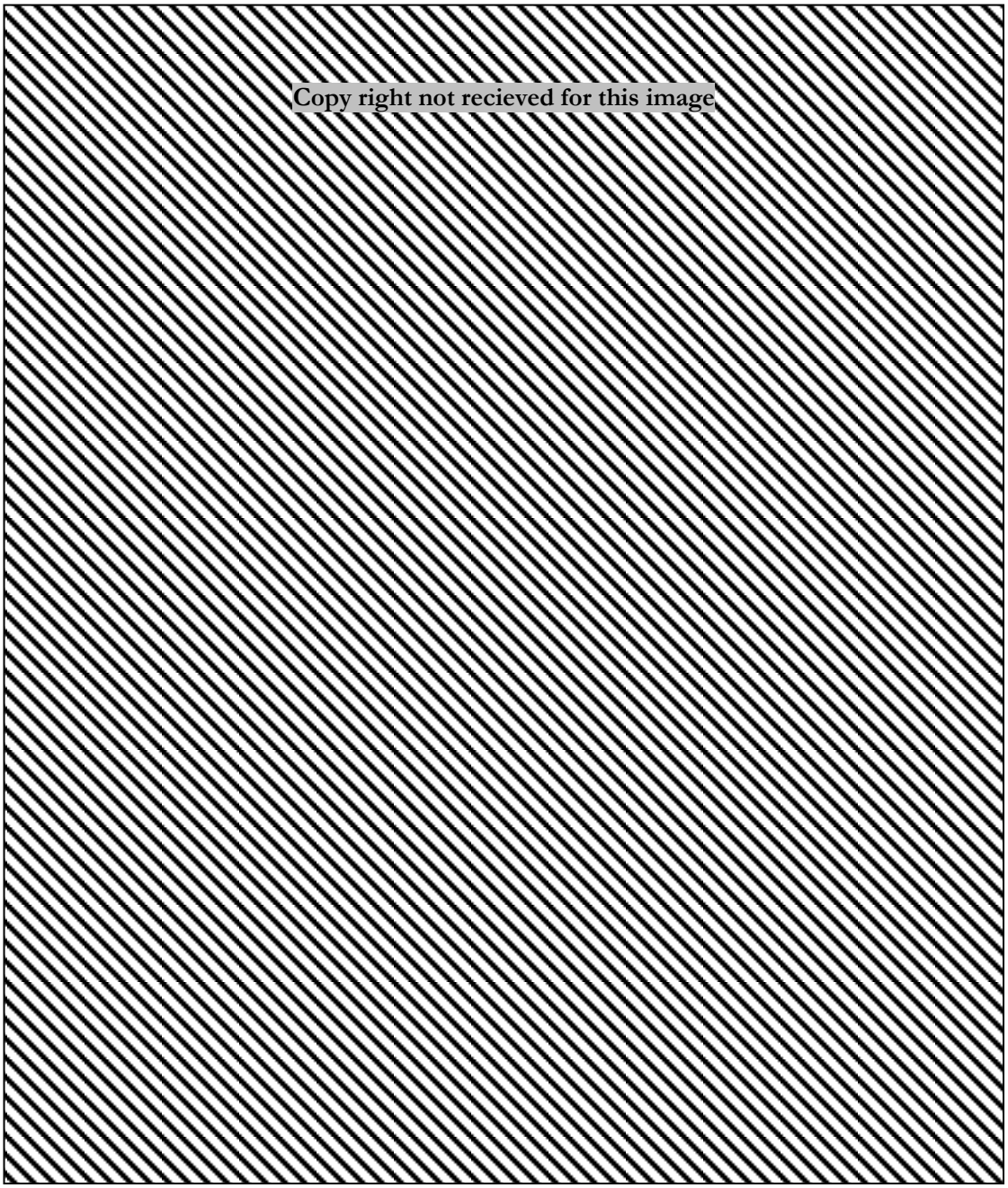

Figure 2-24 The effect of surface chemistry and oxidation on electrical characteristics. **a)** The effect of surface functionalisation is shown by the variable photo current measured for rubrene samples coated by films of each respective molecule. Photoexcitation at 495nm occurred for a duration of 2-4 minutes with a contact bias of 20 V.[21] **b)** left) dark current-voltage characteristics and right) photo current spectral response for both an oxidised rubrene sample an a sample held in vacuum. [30] **c)** Plot of mobility and gate threshold voltage with respect to oxidation and vacuum annealing time for a rubrene FET. Open symbols show field effect mobility, closed symbols show threshold voltages. Inset shows carrier density. [74]

Work by Mitrofanov *et al.* and So *et al.* has looked at the effect of oxidation on the electronic properties of the rubrene.[30, 38, 74] Figure 2-24 b) shows the increase of both photo- and dark-current due to the oxidation of rubrene samples. Mitrofanov *et al.* suggest the increase in dark current is due to the formation of an oxygen related state ~0.25 eV above the HOMO band. In equilibrium this state can 'capture' electrons leaving free holes in the HOMO band, ie. Oxidation produces p-type doping of rubrene. The increase of photocurrent is suggested as being due to impurity assisted exciton dissociation. Figure 2-24 c) shows a similar result to that of Mitrofanov *et al.* produced by So *et al.* concerning the oxidation of rubrene single crystal FETs. It is shown that a higher concentration of introduced oxygen reduces the threshold voltage, V_{th}, of the FET. The measured mobility is unaffected and therefore the reduced V_{th} and increased conductivity is due to the increase in charge carriers due to oxidation. This observation is in agreement with those of Mitrofanov et *al.* and again implies the p-type doping of rubrene due to oxidation. This again shows that for successful design of efficient rubrene based devices the effects of the chemical environment must be understood.

2.5 Conclusions

Within this chapter I have discussed the major physical processes governing the properties of rubrene that make it an ideal candidate for photovoltaic and field effect transistor devices. As has been made clear these processes are easily mediated by the presence of a third component, be that a chemical reactant incorporated post growth, due to environmental exposure, or a structural defect developed during the growth of the crystal. No matter the source of these components, the effect which they have upon the material ultimately will alter how rubrene performs within a device. To optimise both performance and design of any rubrene based system a full and comprehensive understanding of the materials properties needs to be reached.

The studies which I will present herein further the understanding of processes which occur due to exposure of rubrene to the environment. In particular, I will look at the inclusion of environmental components within the material. By utilising nano-imaging techniques I study the local variances that occur due to environmental exposure and produce a detailed picture of how surface modifications such as the observed inclusion of oxygen may occur. To resolve the disputed interpretations of data within the literature I will present a technique with chemical specificity, time of flight secondary ion mass spectroscopy (ToF-SIMS) which has the potential to produce a complete understanding of chemical variances within the material. ToF SIMS clearly shows the incorporation of oxygen at the surface of rubrene. Finally by undertaking two

photon excitation coupled with site specific acquisition of photoluminescence, I present a developed method by which imaging of the sample with spectroscopic resolution can probe the nature of the exciton, its diffusion and the effect of defect inclusion upon its nature.

Chapter 3

Techniques and sample preparation

The studies presented in this thesis centre around three main experimental techniques: atomic force microscopy (AFM), time of flight secondary ion mass spectroscopy (ToF-SIMS) and optical spectroscopy. Within this chapter I will introduce and describe these three techniques. I will then go on to discuss the preparation of samples used within this set of studies.

3.1 Atomic force microscopy

The atomic force microscope (AFM) was developed in 1986 for imaging, measuring and manipulating surfaces at the nano-scale.[81] It allows surface imaging with a resolution 1000 times better than the optical diffraction limit. Information is gathered using a feedback loop created between a mechanical probe at the sample surface and piezoelectric elements used to facilitate accurate nano-scale movements of the probe. A schematic of the elements of an AFM can be seen in Figure 3-1.

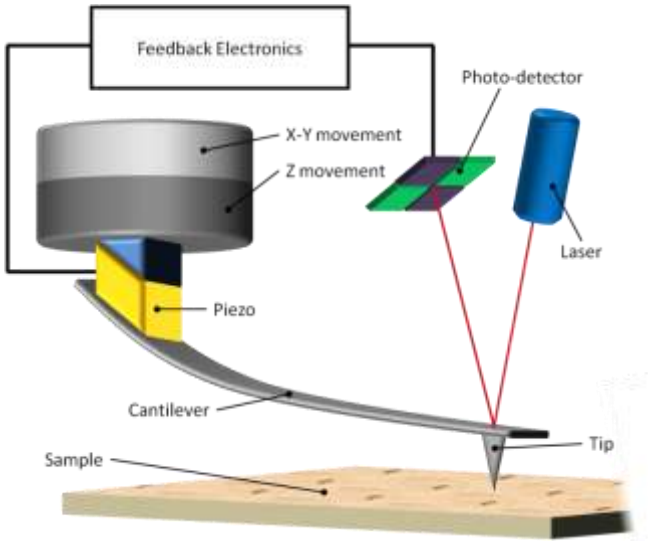

Figure 3-1 Schematic of a typical Atomic Force Microscope. As the deflection of the cantilever changes due to forces between the tip and the sample the position of the reflected laser beam moves on the photo diode. A feedback loop is created between this sensor and the piezo electrics manipulating the probe's position

The microscope can be used in contact mode where the feedback loop is used to achieve a constant deflection of the probe. Alternatively tapping mode can be used where the probe is driven at a frequency 5 % less in amplitude away from the resonance, typical frequencies are around 50 kHz. In this mode the oscillating tip will experience damping due to its proximity to the surface and the feedback loop is used to achieve a constant oscillation frequency. In tapping mode a reduced amount of energy is transferred between the sample and tip. This decreases the probability of surface deformation due to the tip.

All AFM studies were carried out using a VEECO Dimension 3100. This AFM has a lateral resolution of ±0.01 % due to piezo movements which increases to ±10 nm at the nm scale where the effects of tip convolution are apparent. The height resolution of the dimension AFM is on the pm scale for all feature sizes. Tapping mode was used to image the surface of rubrene. It was important to ensure that as little force as possible was applied to the surface. This allowed observation of surface changes without any mechanical degradation of the surface. To accomplish this, on initial contact with the surface the feedback set point was increased gradually until the tip lifted away from the surface. The set point defines the target deflection of the tip, a decrease in set point corresponds to an increase in force between the top and surface. One the tip had disengaged from the surface the set point was reduced slightly to reengage contact and then again increased slightly. At this point minimum force was applied to the surface. This reduced tip-surface interactions and decreasing the likely hood of deformation occurring to the surface. This was extremely important in experiments studying the evolution of the surface. It was imperative to ensure that any changes monitored were due to the natural development of the surface and not caused by the continual scanning of the AFM tip.

3.2 Conductive atomic force microscopy

The AFM can be further modified to allow electrical characterization of a sample's surface; this is undertaken with a metallic coated tip which remains in contact with the surface and is known as conductive atomic force microscopy (C-AFM). Electrical characterisation is accomplished by applying a potential difference between the sample-chuck and a metal coated probe while measuring the current flow between the two. To ensure a good electrical contact is maintained between tip and surface this technique works best when the AFM is used in contact mode. Figure 3-2 shows a schematic of C-AFM.

This technique simultaneously produces a topographical image and a conduction map of the surface. It is possible to stop the tip scanning and while the tip remains in contact with the surface the voltage is ramped 'in situ', creating I-V curves at specific locations on the surface.

This is particularly of interest in comparing the electrical characteristics of different surface features. As the technique is undertaken in atmospheric conditions many factors vary from measurement to measurement. Varying conditions such as humidity affect the conduction between the sample surface and the tip. These variations between measurements therefore renders the technique a qualitative one rather than quantitative. The C-AFM studies were undertaken using a VEECO Dimension which provides ramping of voltages between ± 12 V. The addition of a C-AFM and TUNA§ module was required for the electrical measurements.

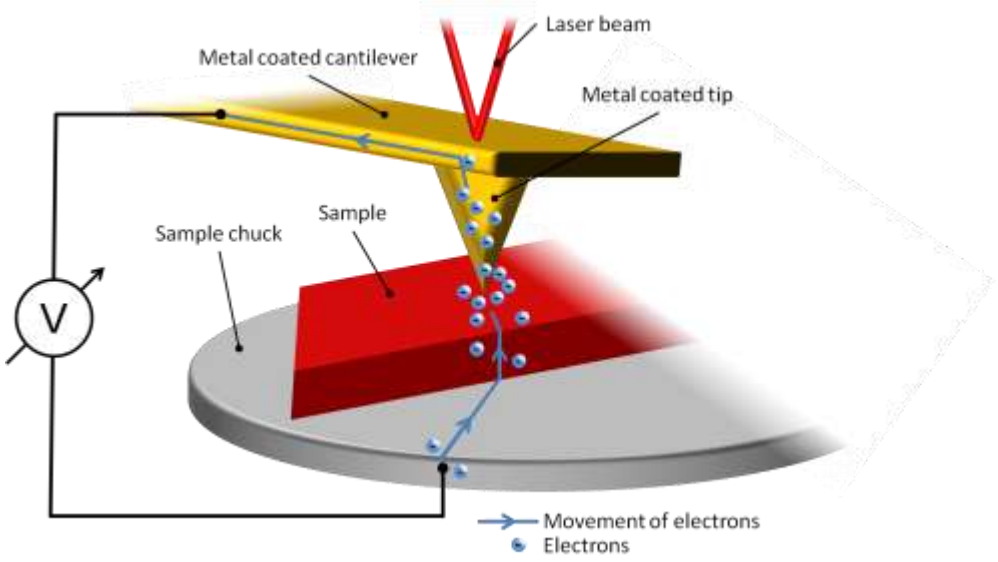

Figure 3-2 Schematic showing the flow of charges in an AFM used in conduction mode. The schematic shows the case for positive tip bias.

3.3 Time of flight secondary ion mass spectroscopy

Time of flight secondary ion mass spectroscopy (ToF-SIMS) provides a technique for mapping the atomic and molecular composition of a material in three dimensions. It offers lateral resolution of up to 100nm and sub a.m.u mass resolution. During measurements the sample is subject to short, 1ns, pulses of primary ions. These primary ions transfer energy to the surface of the material, resulting in ionized molecules being ejected from the surface. These ejected ions are known as secondary ions. After ejection the secondary ions are accelerated by an electrostatic field to a common energy (2keV) and travel over a drift path to a detector. The time of flight through this drift path allows analysis of the charge to mass ratio, (the ToF occurs within the 100µs pulse separations). Recording the time at which particles arrive at the detector provides a

§ TUNA, is a current measuring module for the Veeco AFM, it is a more sensitive module than the standard C-AFM module allowing smaller currents (80 fA – 120 pA) to be measured than that of the C-AFM module (pA - µA range).

mass spectrum from which the molecular ions present in the secondary ion beam can be deduced. Figure 3-3 and Figure 3-4 shows schematic diagrams of the technique and instrument.

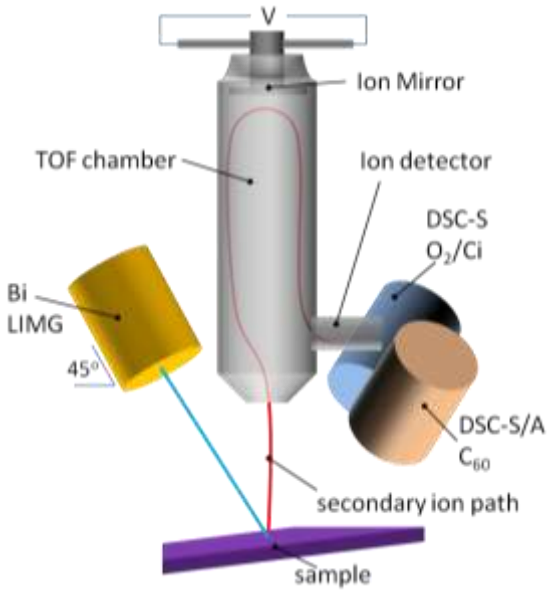

Figure 3-3 Schematic of ToF-SIMS instruments used within this study (ION- TOF V)

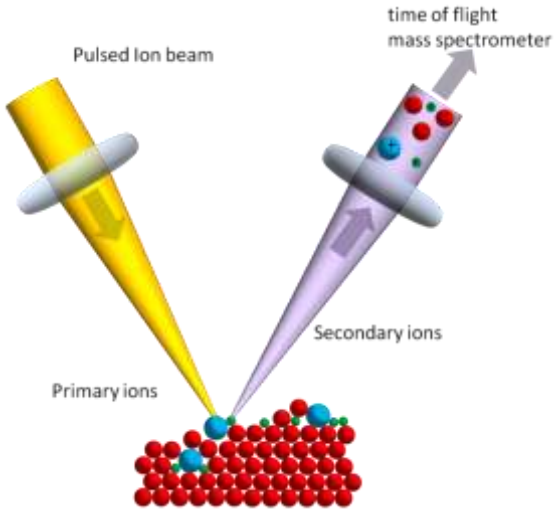

Figure 3-4 Schematic of primary ion and secondary ion interaction with the surface of rubrene.

Using ToF-SIMS the distribution of molecules in both the lateral and medial directions can be mapped. By focusing the primary ion beam onto a small area on the surface it is possible to analyse an area of interest. The beam can then be rastered to produce an image of the lateral distribution of molecules over the surface. By changing the primary ion beam source from a probing beam, to a higher intensity invasive beam, the surface can be sputtered away. Sputtering between mass spectrum acquisitions allows a depth profile of the molecular composition to be

acquired. It is important that in any single analysis the dosage of primary ions does not reach the static limit[**]. Staying below this limit ensures statistically that no molecular site on the surface is analysed more than once. This ensures primary ion irradiation only occurs to the top exposed monolayer.

ToF-SIMS is ideally suited for studying chemical defects in the material, identifying which additional foreign molecules are present. It is possible to analyse the density of these chemical defects and map their distribution. This provides an excellent tool for analysing the chemical environment around structural defects and surface artefacts.

The studies presented within this thesis were undertaken using an IONTOF ToF-SIMS V instrument. The Instrument was fitted with a 25 keV Bi^+ analytical ion beam, a 10 keV C_{60}^+ ion beam, which can be used for either analysis or sputtering, and a Cs^+ sputter gun of varying ion energy. An electron flood gun (20 eV) was applied to the surface to avoid charging of the sample surface during analyses. When mapping the chemical composition the beam moved in a random pattern rather than consecutively analysing neighbouring areas. This allowed any charge to dissipate before returning to a neighbouring location.

3.4 Scanning optical microscopy

The long exciton diffusion lengths within single crystal rubrene have previously been imaged at its surface and indirectly measured in the c-axis of the crystal. To advance understanding of excitons within rubrene and examine their diffusion processes, a technique was devised which would image spatial variations in excitonic recombination. This section will give an overview of the principles used within the experimental design. Further specific details will be covered in Chapter 6 .

Photoluminescence (PL) spectroscopy offers the ability to view the result of excitonic recombination. It therefore offers an opportunity to track any variation in recombination which may be occurring. In order to measure the variation of the photoluminescence spectrum around an excitation point, a scanning optical microscope was developed. The microscope was designed around three techniques; PL spectroscopy, two photon (2P) excitation and confocal microscopy.

2P excitation, as discussed in Section 2.3.2 , allows the excitation point to be moved throughout the sample. Figure 3-5 a) shows a diagram expressing the confined area of 2P excitation which

[**] The static limit is the dosage at which statistically ions are probing locations a second time and therefore analysing sub surface layers.[93]

only occurs at the focal point. Figure 3-5 b) shows how the interaction of two photon can lead to the resultant fluorescence which forms the PL spectrum.

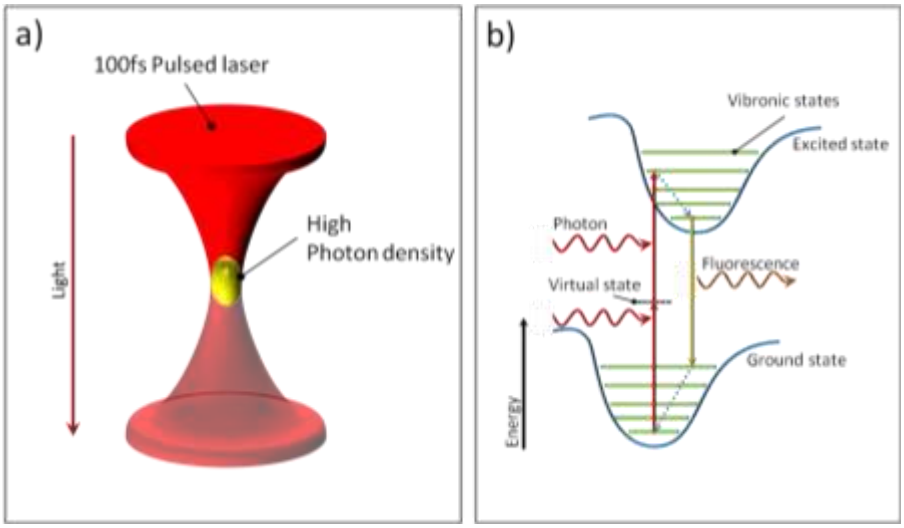

Figure 3-5 a) Indicates the area of high photon density at the focal point of the laser beam, This is the area at which the probability of two photon excitation occurring becomes non-negligible. **b)** Shows the basic energy transitions occurring within 2P excitation and the resulting photoluminescent.

Confocal microscopy allows the spatial selection of the PL being acquired. This technique prevents non-focused light from coupling through a system. It is accomplished by having a second focal plane within the system that contains a pinhole. Within this second focal plane, light focused on the pinhole can propagate through the system, whereas light that is focused elsewhere is unable to pass the plane of the pinhole. This confocal principle is shown in Figure 3-6.

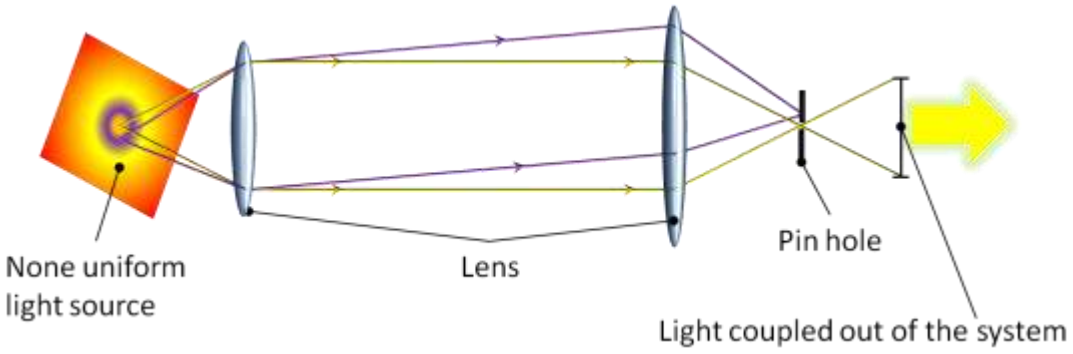

Figure 3-6 Diagram explaining the Principle of confocal microscopy. Only light projected onto the pinhole will be coupled out of the system.

For mapping of the PL at specific loci the sample was placed beneath the excitation laser. It was then positioned so that excitation occurred at the desired location, either within the bulk, at the surface, or at the site of a feature. The resulting PL propagated through a confocal microscope system and the focused light was coupled into a spectrometer which measured the PL spectrum. By scanning the pinhole and recording the PL at each position, a map was created where each element of the map contained the entire PL spectrum. A detailed explanation of the system design is contained within Chapter 6 along with a presentation and discussion of the results obtained using the microscope.

3.5 Sample preparation

3.5.1 Sample mounting

There were two type of sample mounting used within these studies. For techniques which required electrical grounding of the sample an aluminium block was used as the substrate. Before affixing the sample to the substrate the Aluminium was buffed with abrasive paper to remove the any insulating oxide. These studies include ToF-SIMS where charge was required to dissipate and also C-AFM where an electrical connection was required between the sample and the instrument. The sample (typical dimensions of 2 mm × 1 mm × 0.3 mm thick) was mounted using conductive graphite paint (earlier studies used silver epoxy EPOTEK410 though this created a less reliable contact). Although only required for ToF-SIMS and C-AFM studies, due to ease and in order to provide continuity, this mounting process was used for all studies except optical spectroscopy. Figure 3-7 shows a schematic and image of a sample mounted using this method.

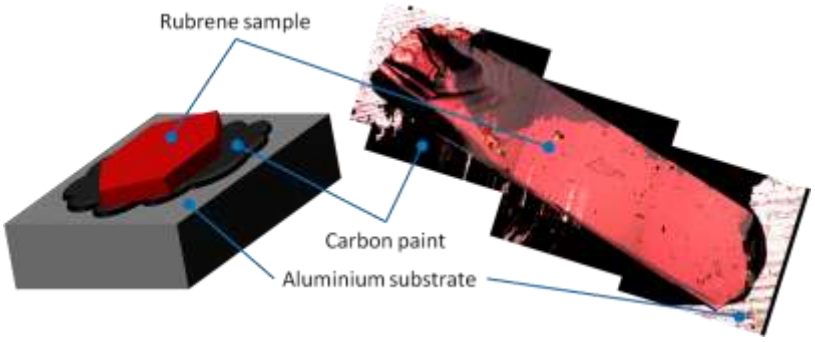

Figure 3-7 A schematic and image showing the mounting of samples. The Conductive carbon paint and aluminium substrate allows grounding of the sample for conductive measurements.

For photoluminescence experiments it was important to prevent scattering and reflection from the substrate. The sample was therefore mounted 'hanging' as shown in Figure 3-8. The sample

is placed between two pieces of 'sticky tape' which then protrudes off the end of a glass slide. It is important to ensure that the sample remains parallel to the plane of the glass slide. This ensure the incident laser and PL acquisition will occur normal to the ab-surface of the sample.

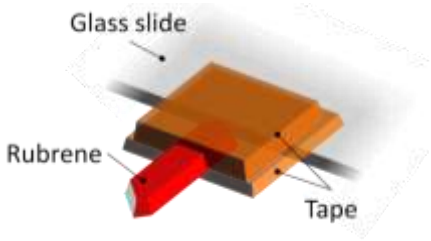

Figure 3-8 A sample mounted for photo luminescent studies. The lack of substrate below the sample prevents any reflection of the excitation beam.

3.5.2 Cleaving

For several of the studies presented within this thesis an environmentally unexposed surface was required. This surface was prepared by cleaving a sample, exposing a new surface from within the bulk. Cleaving provides two major benefits over the 'as-grown' surface. The newly formed surface is free from environmental contamination, allowing controllable studies of chemical doping processes. The newly created surface also provides large molecularly flat terraces which can be reproducibly created. The resulting surface is described in more detail with AFM images in Chapter 4 .

To allow cleaving, the crystal was affixed to a rigid substrate using a conductive epoxy or carbon paint. Once dried a 'cleave post' was glued to the surface using an epoxy. Once this had dried lateral force was applied to the post removing the top of the crystal and producing a new surface from within the bulk. Best results were achieved when force was applied parallel to the b-axis of the crystal. The 'cleave post' was a metallic post of diameter ~ 1.5 mm and length 5 mm. Figure 3-9 provides an image of the configuration used within the cleaving process.

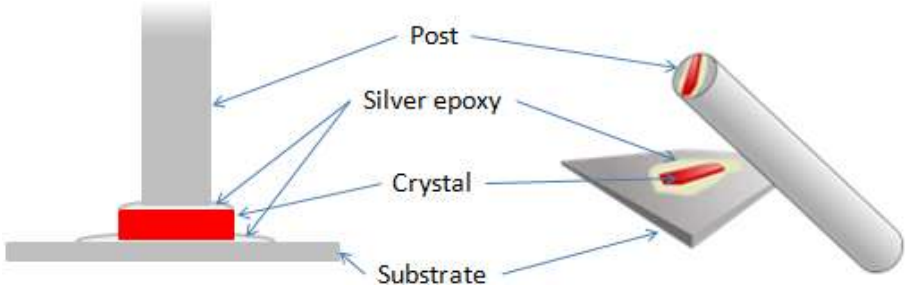

Figure 3-9 A schematic explaining the cleaving process. Once all epoxy is dried, force is laterally applied to the post, resulting in the crystal cleaving. The top part of the sample remains on the post and a fresh unexposed surface is produced atop of the sample on the substrate.

Chapter 4

A topographical study of the evolution at the surface of rubrene

Data presented in this chapter has been included in the following publications,

Thompson, R. J., et al. "Evolution of the surface morphology of rubrene under ambient conditions." *Applied Physics Letters* [76]

Thompson, R. J., et al. "Morphology of cleaved rubrene and its evolution in an ambient environment." *SPIE Photonic Devices+ Applications*. [75]

4.1 Surface evolution

In this chapter I will describe the work undertaken to investigate the evolution of the surface morphology of rubrene single crystals. The study investigates samples which have initially not been exposed to the ambient environment. Imaging of the surface shows how the topography and electrical properties vary at the location of features which develop over time. The results in this chapter shed light on the natural evolution of the surface of rubrene under ambient conditions. These results suggest that the surface processes seen to occur will have a significant impact on the performance of rubrene electronic devices, such as, field-effect transistors and photo-voltaic cells.

The topography and electronic properties at the surface of rubrene were studied with atomic force microscopy (AFM) and conductive atomic force microscopy (C-AFM). Regular images were acquired for more than 20 samples, over the course of 24 months. To study the evolution of cleaved surfaces in the presence of an ambient environment, topographs of the same area were obtained continuously for periods of up to 3 days; these areas were regularly revisited over a period of more than 1 year.

4.1.1 The cleaved surface

Previous studies of rubrene have reported large variations of both electronic and optical properties.[21, 25, 30, 38, 73] These variations are shown to be dependent on the post growth

treatment of the sample. In order to avoid these affects the surface is prepared by cleaving rubrene as described in Section 3.5.2 . This provides two major benefits over the as-grown surfaces: The newly formed surface is un-oxidized allowing controllable studies of chemical doping processes; and large molecularly flat terraces can be reproducibly created, potentially allowing reliable device fabrication away from step edges.

The two topographic AFM images in Figure 4-1 show both the surface of the sample and the counterpart surface of the crystal, remaining on the cleave post. These were recorded immediately after cleaving. As both images are taken from an area which originates from the same location in the original crystal they are therefore mirror images of each other. These images clearly show that cleaving process simply divides the original crystal in two parts without noticeable loss of matter.

In order to locate the same area on both surfaces the cleaved region was first located using an optical microscope. Large features were then located on each surface using an optical microscope. Using a higher magnification optical microscope (~100X) more detailed features are seen, these are believed to be step edges the height of many molecular layers and are found to mirror the features on the opposing surface. By locating mirroring step edge "constellations" on the two surfaces an approximate matching area can be found. Using the largest scan on the AFM (100μm) located at this position allowed the accurate location and imaging of the substrate and post surfaces originating from the same location within the bulk.

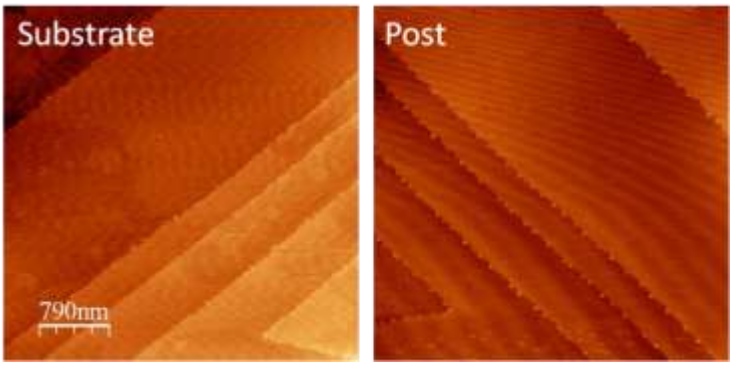

Figure 4-1 AFM images of the surface of a recently cleaved sample. The left image shows the surface of the sample remaining on the substrate. The right image shows the counterpart surface of the sample remaining on the cleave post (recorded ~2 hours later). The mirror image produced shows that the cleaving process separates the sample with preferential cleaving in the ab-plane and no loss of matter occurs. (image recorded by S.Hudziak, B.Yadin & Z.J. Grout)

A cleaved surface can be seen in Figure 4-2(a), after cleaving, the surface consists of local regions of terraces with sizes up to 100 μm × 100 μm, these are separated by step edge boundaries. The

majority of steps have a height ~1.4 nm, corresponding to one rubrene monolayer, other larger steps are seen at multiples of this height. The steps aligned along regular orientations as seen in Figure 4-2(a). This is in contrast to step edges on the as-grown surfaces which tend to be rough and meandering,[82, 83] such as that shown in

Figure 4-2(b).

Figure 4-2(c) shows an as-grown (not cleaved) surface after storage for 3 years, exemplifying the extreme of how post-growth development can roughen and degrade the surface, probably due to oxidation and unintentional deposition of debris. After growth the samples were stored in a sample box kept in normal laboratory conditions, no intentional oxidation occurred. The unknown nature of the observed post-growth development has implication for rubrene's suitability for device applications. The pristine cleaved surface gives us an excellent unexposed starting point to monitor and understand the surface development of rubrene from the moment it is exposed to its environment.

It was seen that the pristine cleaved rubrene surfaces underwent extensive reorganisation of material at the surface, first noticed on a time scale of 30 minutes after cleaving. This indicates that the cleaved surface is not a stable system and one which quickly evolves in the ambient environment.

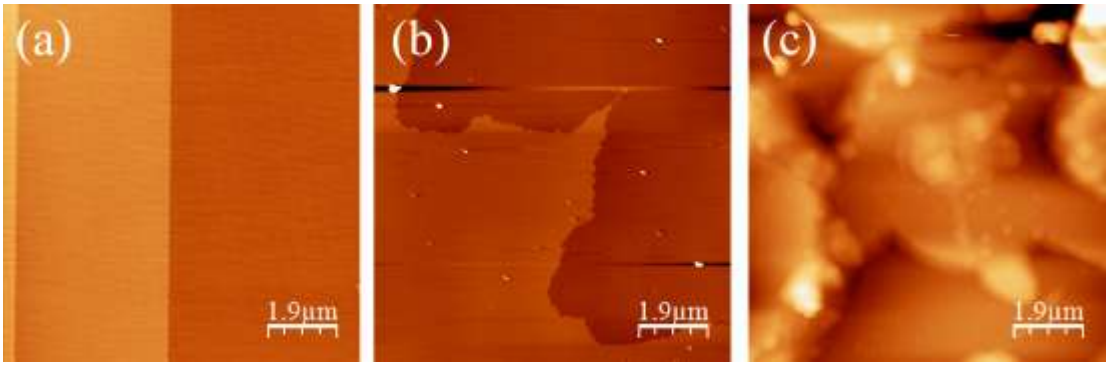

Figure 4-2 Topographic AFM images (tapping mode) of single-crystal rubrene surfaces; **(a)** a freshly cleaved sample showing three molecular terraces, **(b)** an as-grown sample 2 weeks after growth, and **(c)** an as-grown sample approximately 3 years after growth. The colour scale maximum is 10 nm, 13 nm and 400 nm respectively. [76]

4.1.2 Bead development

The first of two distinct surface features seen to develop on the freshly cleaved surface is the growth of small 'beads' of matter. These can be seen to appear at the step edge boundaries and are imaged as bright circular protrusions as highlighted in Figure 4-3. Beads were initially seen between 30 minutes and several hours after cleaving. When initially detected they had an average

height of 3 nm and a bead-to-bead spacing of 250 nm – 600 nm ranging from sample to sample. Figure 4-3 shows a line profile along a step edge. Within the profile the beads can clearly been seen with an average spacing of 480 nm. The evolution of the beads is shown in Figure 4-6, as clearly seen continual growth of the beads occurred. One hour after cleaving, Figure 4-6(a), rubrene shows a clean surface; one day after cleaving, Figure 4-6(b), the edge is decorated with beads and has elongations growing from the step onto the lower terrace (discussed in section 4.1.3); after 7days and 11 months, Figure 4-6(c) and (d) respectively, the step edge shows substantial overgrowth, some beads have merged and large features are seen to grow from the step edge. The growth occurred in both illuminated and un-illuminated conditions. The average height of beads for several samples is plotted in Figure 4-5 with respect to time. The majority of samples have a constant rate of bead growth for up to two years, with no detectable saturation. In a minority of cases the beads had a reduced rate of growth reaching a maximum. This can be seen in Figure 4-5 with the sample plotted as red crosses. In the cases where this was seen to occur, a second surface feature was seen to grow directly below the beads. This feature was a 'finger', as discussed in the following section. The beads in this minority of cases appeared to be supplying material to this second feature.

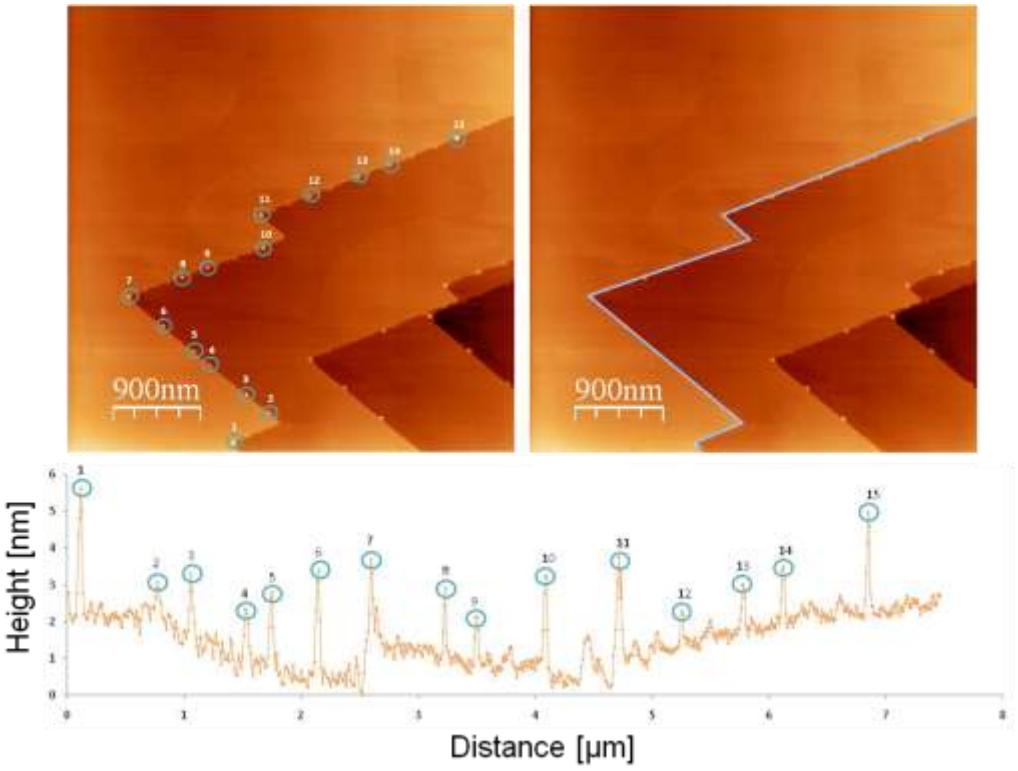

Figure 4-3 Two copies of the same AFM image of a recently cleaved sample. The left hand image highlighting individual beads and the right hand image highlighting (blue line) the path that is shown in the cross section below the images.

The measurement of bead height and spacing was undertaken using the software WSXM,[84] the cross section profile in Figure 4-3 allows easy measurement of the bead spacing. The height of beads was measured by drawing two cross sections parallel to the direction of tip scanning (this ensured no height error due to comparing data between two adjacent lateral scans). One cross section was located to intersect the highest point of a bead and passed over both levels adjacent to the step, this gave the height of both bead and step. The second cross section was located adjacent to the bead and gave the step height. The bead height was calculated as the difference between highest point of the first cross section and the measured step height. An example of bead height calculation can be seen in Figure 4-4.

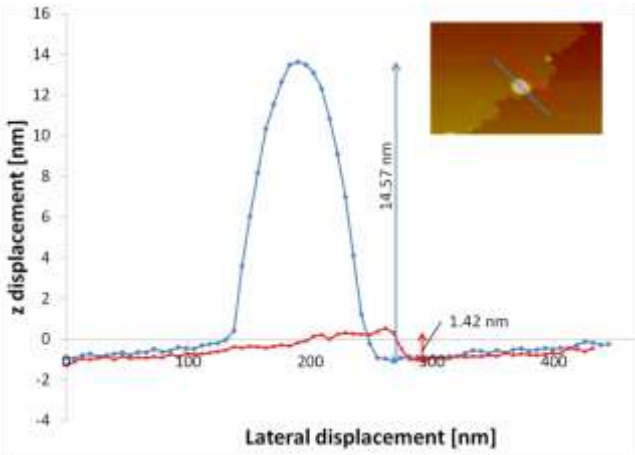

Figure 4-4 Example of the calculation of bead height. The line profiles are taken from locations identified in the insert. Bead height is calculated as the height of the bead plus step, taken from the blue profile minus the step height taken from the red profile. In this example the bead height would be calculated as 13.15 nm.

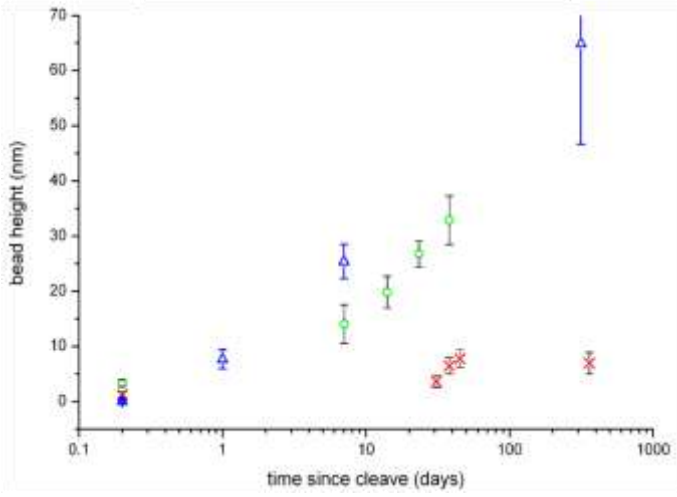

Figure 4-5 Bead formation after cleaving for several samples shown as the bead height vs time. Average bead height is evaluated using topographic AFM images as explained in the text; error

bars show one standard deviation taken over a sample size of approximately 50. Blue triangles correspond to the sample shown in Figure 4-3. [76]

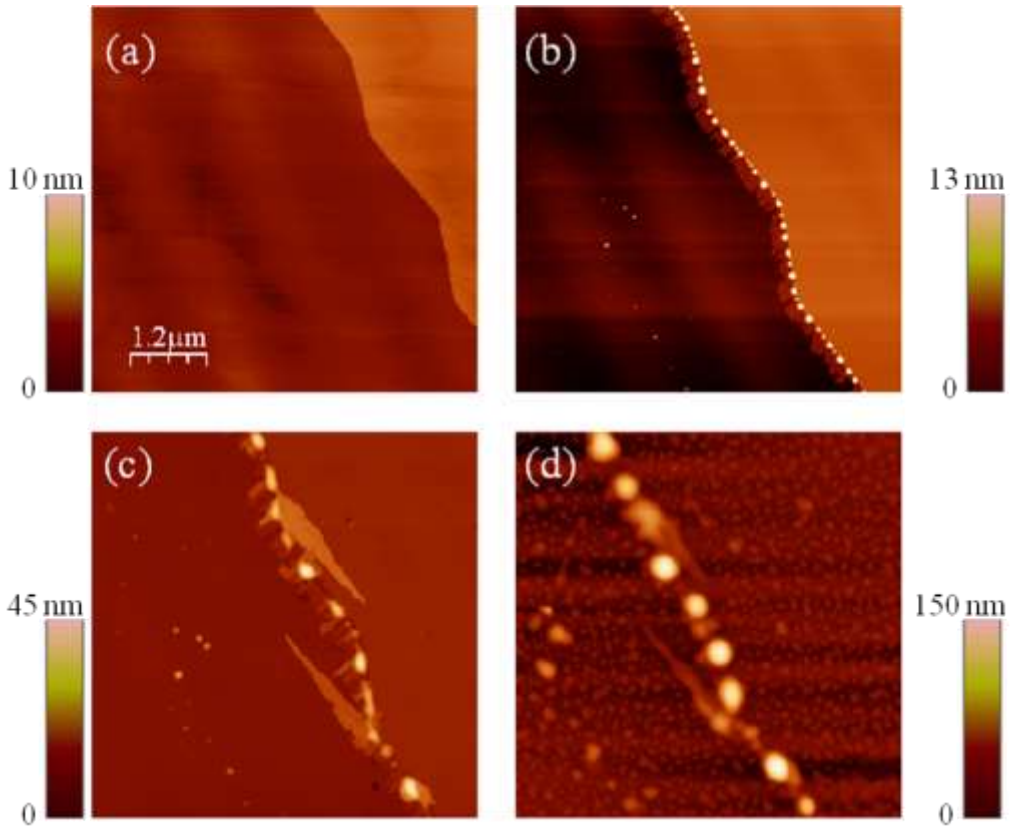

Figure 4-6 Topographic AFM images showing the development of beads on the surface with time: (a) 1hour after cleaving, (b) 1 day after cleaving, (c) 7 days and (d) 11 months after cleaving. The colour scale (black to white) is 10 nm, 13 nm, 45 nm and 150 nm for images (a) ,(b), (c) and (d) respectively.[76]

4.1.3 Finger development

Several hours after initial bead formation their development was accompanied by a second change in surface morphology; the formation of 'fingers'. Like the beads, the fingers originated at step edges. However, the fingers took a completely different form, creating protruding narrow (width in the range of 20 – 100 nm measured by AFM), one molecule high features, as seen in Figure 4-7 and Figure 4-8. Fingers were seen to appear several hours after cleaving and their growth originated from the base of the step edges. The fingers were molecularly flat and at the same height as the single monolayer steps ~1.4 nm. It can be seen clearly in Figure 4-7, Figure 4-8 and Figure 4-9 that the fingers have an anisotropic growth. Figure 4-9 shows the geometry of the crystal, from this the crystallographic axes can easily be deduced. It is seen that the preferred growth direction aligns along the a-axis of the crystal. Fingers were seen to have a length to width ratio of up to 7:1 and grow to lengths in excess of 1 μm. It should be noted that as

exhibited in Figure 4-9 surface development is seen on the terraces though this only occurs on a minority of samples.

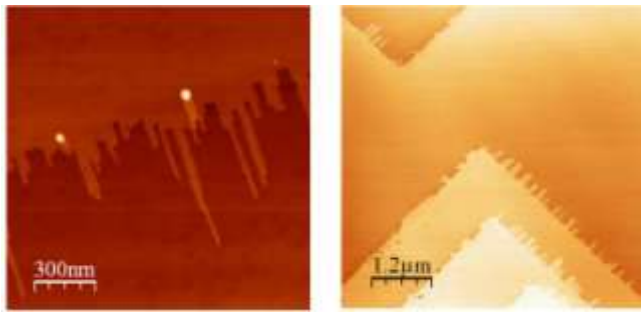

Figure 4-7 AFM images showing the growth of fingers. The second figure clearly shows the anisotropic growth of the fingers.(Note the crystallographic orientation of these images is not the same)

The height of the fingers implies that they are constructed of either rubrene or a rubrene species, such as rubrene peroxide, where the perturbation of the structure is of such a small degree it is not resolvable using AFM. The fact they show a smooth molecularly flat surface and orientate themselves with a crystallographic axis implies that they have crystallographic packing. Fingers have been seen to grow from the base of beads and a reduction in the bead height was observed. Examples of this can be seen in Figure 4-8 f) and g). This observation suggests that material from the beads can migrate to form the fingers. In the case of the sample seen in Figure 4-5, labelled with red crosses almost every bead was coupled to a finger. In this case the average growth rate of beads reduced over time and the beads reached a maximum height. This in turn infers that the beads are composed of the same material as the fingers, although, unlike the fingers, there is no evidence that the structure of the beads exhibits crystalline ordering. It should be stressed that the coupling between bead and finger growth is not seen in all cases. Comparison between Figure 4-8 f) an g) shows evidence of step edge roughening and recession. The beads were seen to remain in a fixed position and can therefore be used as a reference point. This recession and roughening of the edge also leads to a hypothesis that the molecular reorganisation was redistributing molecules from the step edge to form the fingers. Figure 4-10 details the suggested processes which are hypothesised to occur when the crystal is cleaved. These processes include the incorporation of an ambient environment component stimulating initial growth. Roughening is then seen at step edges as the fingers are formed. Finally, in a small number of cases material migrates from the bead to the finger.

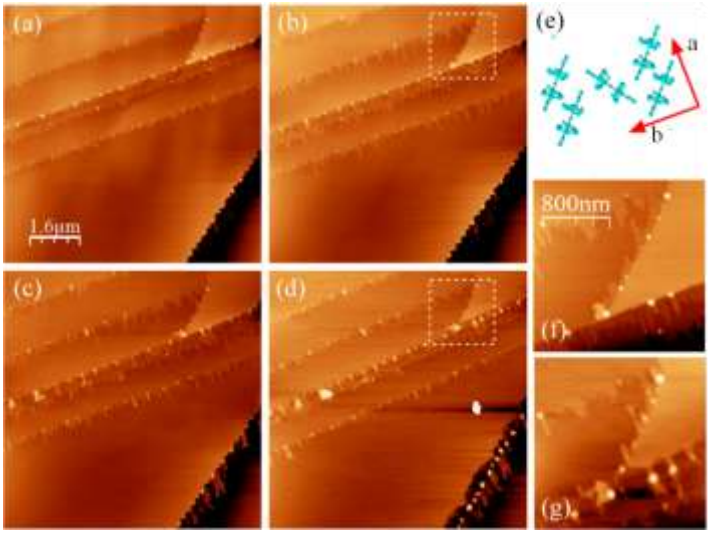

Figure 4-8 Topographic AFM images (tapping mode) showing the change in surface morphology of a rubrene surface (a) 4.5 weeks, (b) 5.5 weeks, (c) 6.5 weeks and (d) 11 months after cleaving. Images (f) and (g) are enlargements of the same area indicated in (b) and (d) respectively. The colour scale (black to white) for images (a) and (b) is 13nm, for (c) and (d) is 17nm, and for (f) and (g) is 20 nm. Schematic (e) shows the crystallographic directions a and b and the orientation of rubrene molecules.[76]

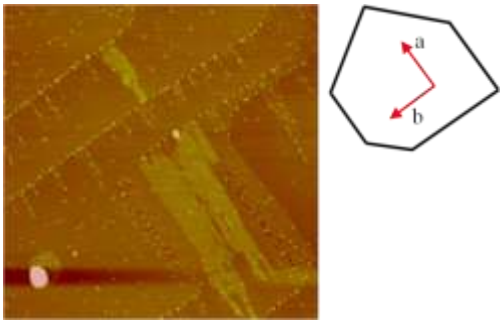

Figure 4-9 Topographic AFM image of surface several weeks after cleaving. The left diagram shows the orientation of the crystal. The crystallographic axes as labelled can be easily identified by the crystals geometry.

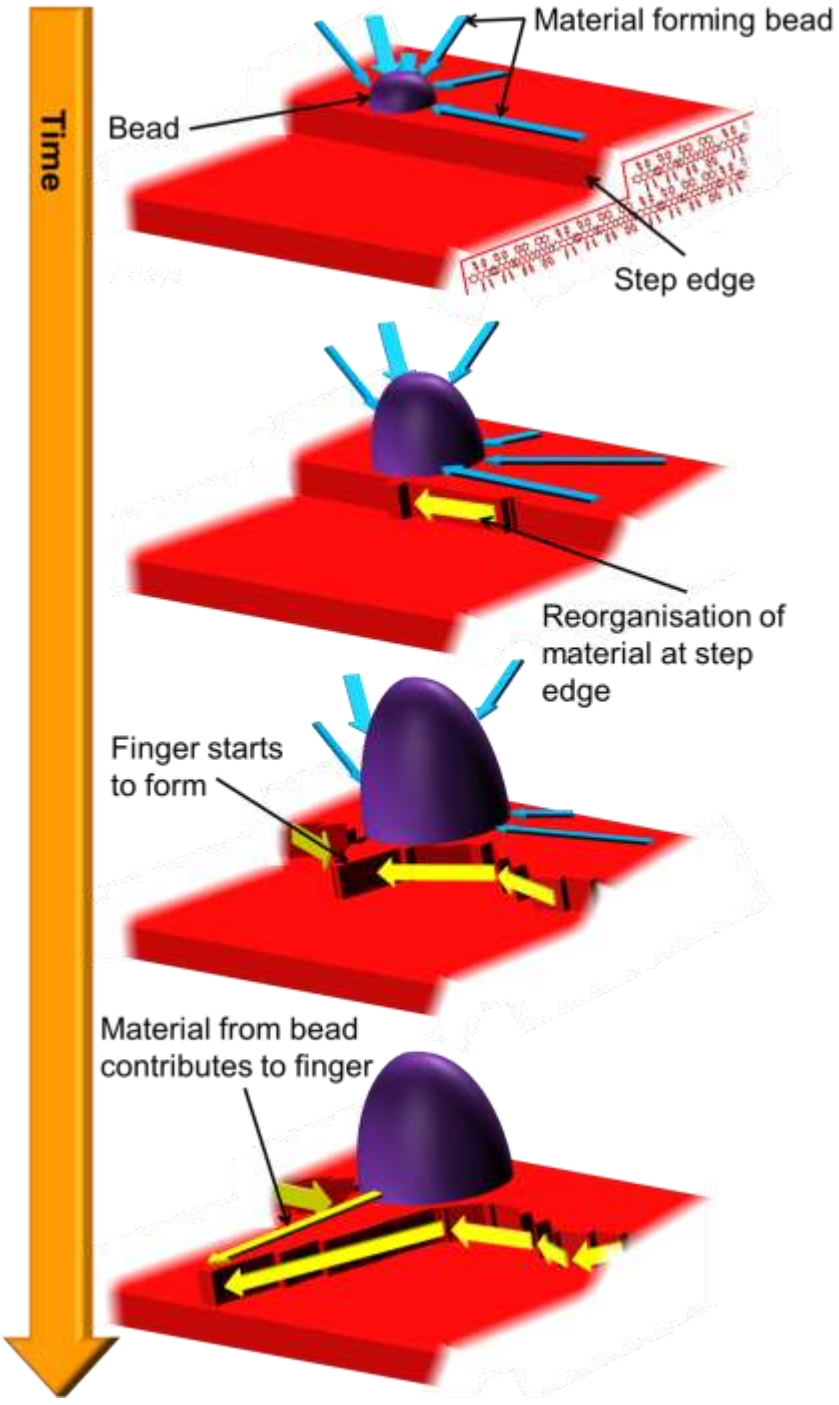

Figure 4-10 A schematic representation of the hypothesised processes occurring in the growth of 'beads' and 'finger". It should be stressed that both the growth of fingers and beads can occur at separate sites, and therefore the final step is not always of relevance

4.2 Environmental effects on surface evolution.

In order to understand the origin of beads and fingers, I investigated the effects of atmospheric conditions on surface development. Several rubrene samples were prepared for cleaving and then placed into an argon environment 3 mbar above ambient pressure. The samples were cleaved within the argon atmosphere and either removed immediately or left in the argon atmosphere for several days after cleaving. On immediate removal from the argon atmosphere the cleaved samples showed no difference to samples cleaved in normal atmospheric conditions and developed as such. The samples that were removed a week after cleaving showed no surface developments while being in the argon atmosphere. This is evident in the AFM image in Figure 4-11 which was recorded immediately after removal from argon. As the plot in Figure 4-11 indicates on exposure to an ambient environment the samples which were cleaved and stored in argon, began to develop as though they had just been cleaved. In a few cases these samples showed an increased rate of bead growth, though always had a molecularly flat undeveloped surface on removal. The increased rate of growth was inconsistent within these studies and further investigation is required to understand this phenomena. The undeveloped surface on removal from argon shows that the growth of beads is initiated by the presence of an atmospheric component.

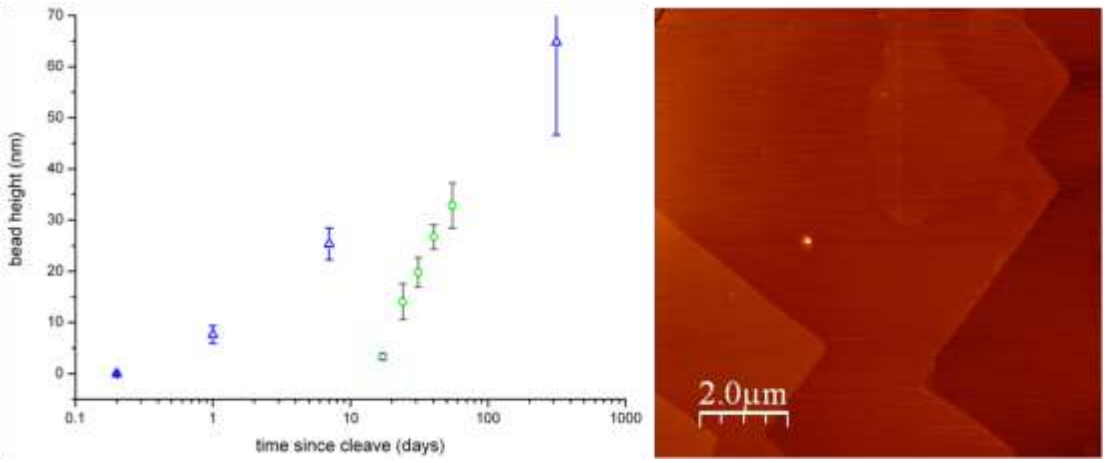

Figure 4-11 Plot showing the height increase of beads on samples cleaved in an argon atmosphere, one sample was immediately removed into an ambient atmosphere (blue triangle) and the other removed after 10 days. **Left,** shows an AFM image of the surface after being removed from the argon atmosphere.

4.3 Electrical characteristics of the surface.

In order to probe how the electrical characteristics of the cleaved surface vary from that of an as-grown surface, and observe how these characteristics change with the development of the surface conductive atomic force microscopy (C-AFM) was used. C-AFM as discussed in section

3.2 is a modification of AFM where current flow is measured while a potential difference is applied between the sample and tip. C-AFM is a technique which is rarely cited in literature, especially for the study of organic electronics where surfaces degradation due to tip interaction is seen to occur easily. Much time and effort was therefore spent developing the method of implementing C-AFM on rubrene samples.

For a good continuous channel of conduction to be made between the tip and sample, the AFM must operate in contact mode. This mode of operation exerts a greater force to the surface than the tapping mode which was used for imaging. The surface of rubrene appears to be easily susceptible to surface damage from scanning. For this reason scanning in contact mode was not ideal but could be achieved if the feedback set point was altered to produce minimum surface-tip interaction as described in section 3.1 (For the microscope used, when in contact mode decreasing the set point reduced the force applied by the tip). Undertaking a reproducible method of engaging the tip also acted to ensure that the surface area of the tip which was in contact with the surface was constant between scans. This is important as increasing the force of the tip interaction increases the amount of contact with the sample surface, therefore increasing the current flow.

Initial conduction experiments showed that the measured current would diminish with respect to time. It was also seen that when a continuous scan returned to an area that had previously shown conduction, no current flow would be detected. It was hypothesized that charging was occurring on the surface and the charge was unable to dissipate. To allow dissipation of the charge and increase conduction a conductive track was created using carbon paint between the sample mount and the ab-plane top surface. This bypassed the large bulk resistance of the c-axis. The addition of the conductive track removed the effect of charging providing a measurable current. Bypassing conduction through the bulk also acted to remove the inconsistency between samples introduced by the series resistance of the bulk which was dependent on the dimension of the crystal.

After undertaking many C-AFM measurements on several samples, it was evident that performing measurements in atmospheric conditions did not provide data which allowed comparable quantitative analysis. This was due to uncertainties of the series resistance produced by varying environmental factors such as humidity and temperature. It was also extremely difficult to ensure that the force applied remained constant when changing samples and AFM probes. Although quantitative comparisons of different measurement were not possible the

results of a single scan can be compared. Qualitative comparisons could also be made between data recorded from different scans.

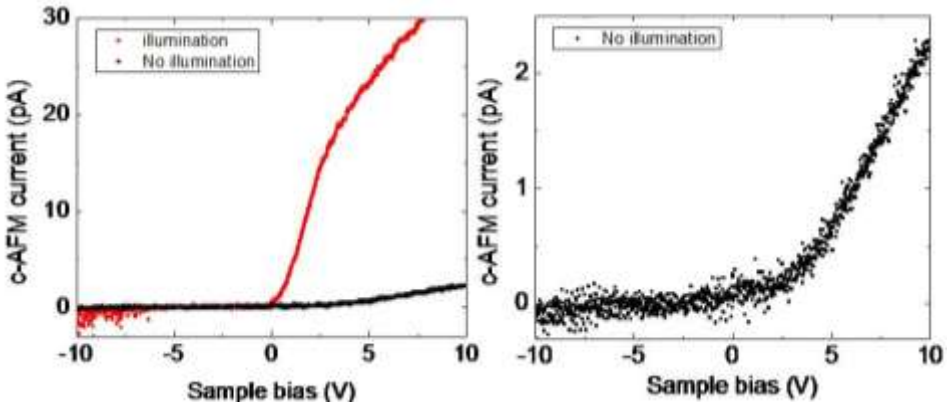

Figure 4-12 I-V Characteristics recorded by C-AFM under illumination (red) and without Illumination (Black). The right shows the dark I-V data on a smaller scale.

In order to perform I-V spectroscopy the tip was positioned on the surface and the potential difference was ramped. This IV spectroscopy showed a degree of hysteresis as seen in Figure 4-13, this was reduced with slower ramping but was never removed entirely. The hysteresis implied that even with a direct surface contact, charge took a relatively large time to disperse. Forward ramping can be seen in Figure 4-12. It shows that conduction occurs both with and without illumination though the photo-current constitutes a substantial component as highlighted by the difference between the two traces.[75]

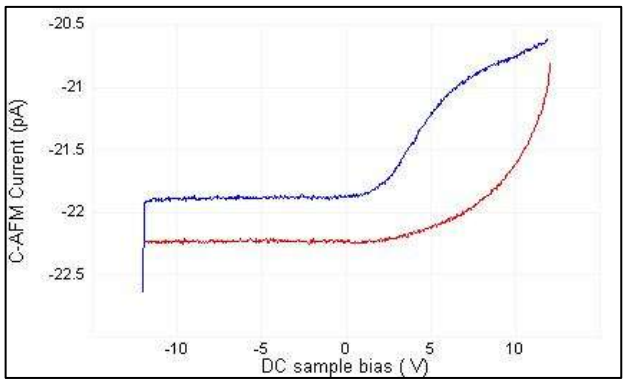

Figure 4-13 Example of hysteresis seen when ramping the voltage while in situ while undertaking C-AFM. (A current offset is seen due to internal resistance of the TUNA module)

Figure 4-14 shows a topographical image, (a), and conduction map, (b), that were acquired simultaneously. By analysing and comparing these images, we can see that on terraces there is a

uniform conduction, as previously has been seen on as-grown surfaces.[85] As the probe approach step edges and the location of beads the conduction is seen to vary. Figure 4-14 (b) shows a prolonged increase in conduction to the left of beads. This is not a real effect but caused due to the slow response of the system. It is a repercussion of the settings required to reduce the tips interaction with the surface. When the tip passes over a raised feature such as a bead, the feedback loop corrects the height of the tip and returns it once is has passed over. When trying to ensure as little interaction with the surface as possible while still maintaining contact for conduction this process becomes less and though not resolvable in the topography it has a visible effect on conduction. In this case the scan direction was from right to left. This effect is removed when the scan is vastly slowed down as has been done for the measurements presented in Figure 4-14(c) &(d).

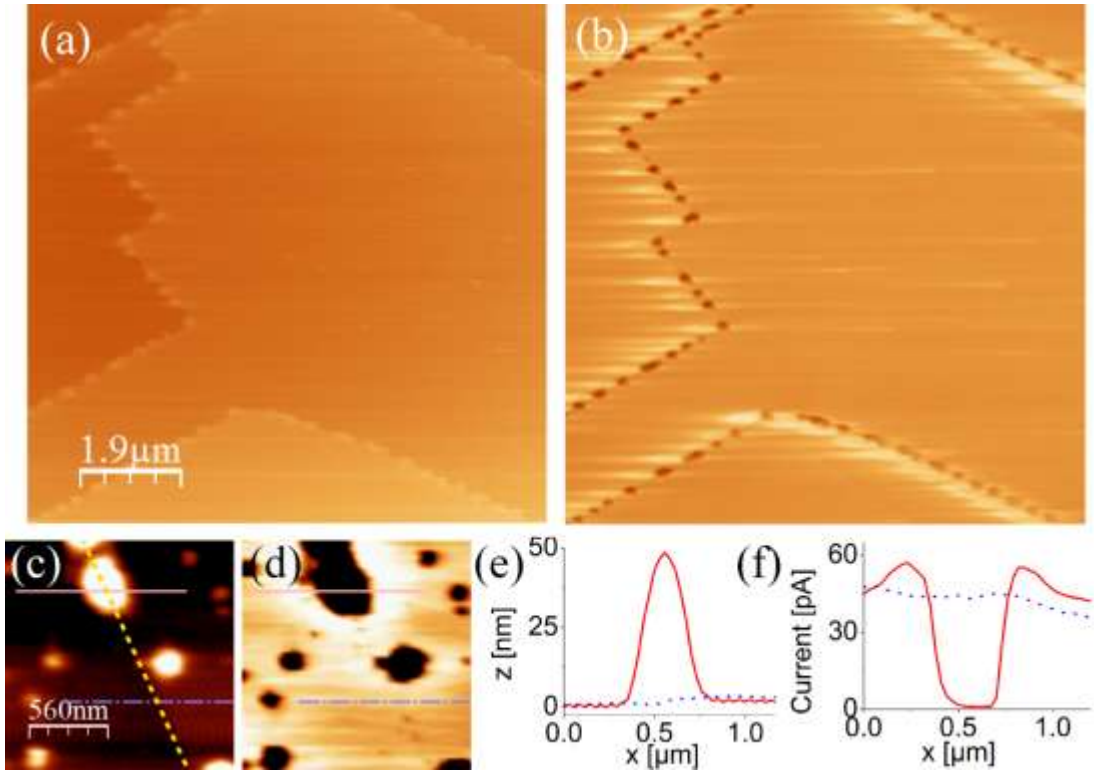

Figure 4-14 Rubrene surface 2 months after cleaving: (a) topographic AFM image (contact mode) with a colour scale (black to white) of 100 nm, (b) C-AFM image of the same area as (a) with a colour scale (black to white) range of 200 pA. (c) and (d) show a topographic image and a C-AFM map respectively near a step edge, highlighted in (c) for ease of identification. (e) and (f) show topographic and conduction profiles respectively of the indicated paths in figures (c) and (d).[76]

Figure 4-14 (c) and (d) show a topographical image and conduction map respectively at a much smaller scale than (a) and (b). (e) and (f) show line profiles taken from the indicated locations on (c) and (d) respectively. The red line indicates the profile located over a bead, the blue dotted line indicates the profile located over a step edge, (the step edge is highlighted by a yellow dotted line). The first thing that can be noticed and is also clear from Figure (b) is that at the location of a bead there is no detectable conduction. Interestingly, it can be seen that in close proximity to the bead the conduction increases. This effect can be confirmed as an actual effect and not an imaging artefact as the increase is seen at a distance of ~0.05 μm away from any topographical variance. This distance is large enough to prevent any interaction between the tip and the feature. The step edge appears to have no effect on conduction.

The reduced conductivity within the beads may be due to a lack of a crystallographic structure that prevents the overlap of pi-orbitals between molecules, inhibiting charge transport.[86] The increase of conductivity in close proximity to the bead is an intriguing observation and could imply that the bead causes band bending on the surface directly below the bead, either as a result of an inter-facial effect or due to the bead being charged by the AFM tip.

4.4 Conclusions

A method has been developed for cleaving rubrene crystals. This method allows reproducible production of surfaces that are previously unexposed to the ambient environment. These surfaces regularly have large terraces, with sizes up to 100 μm ×100 μm that are intersected by straight step edges with regular orientations. This cleaving method provides an ideal surface for investigations of pure rubrene surfaces and their reaction to the environment. AFM studies show that the cleaved rubrene surface undergoes significant changes in the normal atmospheric environment. These changes suggest that the pure rubrene surface is more reactive compared to the as-grown rubrene surface. The cleaved rubrene surface can serve as a reproducible and reliable standard for determining pure rubrene surface signatures.

Two distinct processes are identified as occurring when the pure rubrene surfaces are exposed to an ambient environment: the formation and three-dimensional growth of nanoscale beads; and the formation and two-dimensional growth of narrow, monolayer high fingers. As these processes exhibit a dependence on the environmental conditions, they imply the incorporation of an atmospheric component, likely oxygen or water, into the material. The exact structure and composition of the beads remains unknown. The material initially forming the beads is not noticeably migrating from other locations on the surface. It is obvious however that step edge boundaries play an important role in the formation of both beads and fingers. The step edge

offered a different chemical environment to terraces, as well as allowing a degree of molecular steric deformation. Both of these properties of the step edge can make a reaction of rubrene with the environment more favourable. The conductive atomic force microscopy studies show that the beads exhibit an insulating behaviour, with an increase in conductivity at the interface between the bead and rubrene. The topography and conduction of the bead indicate a lack of crystallographic structure. However, as the finger growth is in some cases coupled to the beads, it is implied that beads and fingers consist of the same material, suggesting the beads are amorphous clusters of rubrene or oxidized rubrene molecules.

The results from this study suggest that the model of the as-grown crystalline rubrene surface needs to be refined in order to explain its passive behaviour compared with the observed behaviour of the cleaved surfaces. A better understanding of the as-grown rubrene surface, which is often considered to be pure, is essential to determine origins of the charge transport modification in rubrene.

The experimental investigations presented here, show phenomenology of the morphological changes on the cleaved rubrene surface and how these changes affect the charge transport on the microscopic scale. The experimental results confirm that the modifications of surface conductivity are likely to be controlled by the presence of crystallographic defects, such as grain boundaries and step edges. AFM studies however fall short of providing detailed information about the chemical composition or molecular arrangement inside the beads and fingers. I discuss in Chapter 5 and Chapter 6 the techniques of time of flight secondary ion mass spectroscopy and photoluminescence spectroscopy, both are techniques which can help understand the environment at these structural defects.

Chapter 5

ToF-SIMS Studies of rubrene

Data presented in this chapter has been included in the following publications,

Thompson, R. J., et al. "Revealing surface oxidation on the organic semi-conducting single crystal rubrene with Time of Flight Secondary Ion Mass Spectroscopy." *Phys. Chem. Chem. Phys.* (2013). [87]

In this chapter I will discuss the application of Time of Flight Secondary Ion Mass Spectroscopy (ToF-SIMS) to investigate the surface of rubrene single crystals. The data provides direct measurements of molecular and atomic species present on the surface of rubrene. The abundance of these molecular and atomic species has been mapped showing an inhomogeneity of rubrene oxidation at the surface. These maps indicate that increased oxidation occurs at the location of crystallographic defects. We also discuss the effect of using differing primary ion beams and determine that C_{60}^{3+} and Bi_3^+ are the preferred analysis beams for mass spectroscopy and spatial profiling respectively. Ar cluster sources are also seen to be ideal for depth profiling the material.

5.1 Chemically specific studies of rubrene

As we have shown in Section 4.3 and as exemplified by Najafov *et al.*[21] and Mitrofanov *et al.*[30] the surface of rubrene plays a vital role in the control of charge carrier concentration and mobility as well as exciton recombination. Importantly it has been debated in the literature whether there is a natural surface oxidation which affects these properties.

The studies discussed in Chapter 4 show that when cleaved, the fresh rubrene surface reacts with the environment. This environmental reaction leads to the three dimensional growth of beads and two dimensional growth of fingers. The beads were seen to affect charge carrier behaviour at the surface. It was conjectured that the small scale topographical variations were an effect of oxidation. Mitrofanov *et al.* have shown the presence of oxygen during growth increases the dark- and photo- conductivity of rubrene.[30] It is also well established that the surface

chemistry of rubrene plays a large role in the photoconductivity, for example Najafov *et al.* show that the deposition of parylene-D increases photoconductivity by a factor of 1.5.[21] It is clear from these previous studies that for rubrene to be used as a reliable material in electronic devices, the surface modifications, whether intentional or naturally occurring, need to be understood.

The majority of research into the chemical evolution at the surface of rubrene has so far relied on indirect methods such as photoluminescence spectroscopy, high pressure liquid chromatography, and Laser Desorption Ionisation ToF mass spectroscopy.

Photoluminescence (PL) spectroscopy has been undertaken in several studies on rubrene and uses the peaks present in the emission spectrum of the excited material to identify energy transitions. These transitions can be modified by the presence of different chemical species. Once the origin of a transition is deduced this leads to a 'spectral signature' indicating the presence of specific chemical species.[30, 38, 79] It should be noted that the origin of the energetic transitions evident in the electromagnetic spectrum of rubrene is debated. In particular the origin of the 650 nm PL band is speculated to originate from the chemical presence of oxygen,[30, 38] and also conversely said to be due to the presence of amorphous, non-crystalline, pockets of pure rubrene within the crystal.[88]

High Pressure Liquid Chromatography has been used to measure the purity of rubrene crystals. The sample is dissolved in chloroform and a pressure driven process is used to separate the different molecules within the solution. These molecules can then be analysed by mass spectroscopy showing the molecular composition of the rubrene sample.[78]

Laser Desorption Ionization Time of Flight mass spectroscopy (LDI-ToF) has been reported as used to quantify the purity of thin organic films and single crystals by measuring the abundance of rubrene oxide.[89, 90] The LDI-TOF technique uses a laser to ionise and liberate surface and subsurface molecules whose mass charge ratio is then analysed by time of flight spectroscopy.

By comparison ToF-SIMS offers an excellent opportunity to directly observe the molecular composition of the very top most exposed molecules and image the spatial variation of this composition. This therefore provides a valuable tool to study the resultant molecular composition as well as viewing any inhomogeneity present due to the incorporation of defects.

5.2 Mass Spectroscopy

ToF-SIMS analysis of rubrene has not been previously reported. Therefore, initial experiments were carried out to establish which primary ion source produced the best ion yields from the rubrene sample. In order to do this the experiments aimed to deduce the methodology required to produce the maximum number of secondary ions per primary ion, with as little damage to the surface as possible.

5.2.1 Analysis of the primary ion beam

The primary beam sources tested were: Bi^+, Bi^{2+} Bi^{3+}, Cs^+, $C60^+$, C_{60}^{2+} and C_{60}^{3+}. The results of the primary beams which produced a substantial yield are highlighted within Figure 5-1 show that for each primary ion beam the spectroscopic peaks of rubrene ($C_{42}H_{28}^+$) at m/z of 532 were observed, along with the isotopes of the molecule. The isotopic ratios are in agreement with the naturally occurring ratios of carbon isotopes.[91] This is of note as it shows the mass spectra are accurately calibrated and the intensities measured are accurate with no mass interferences.

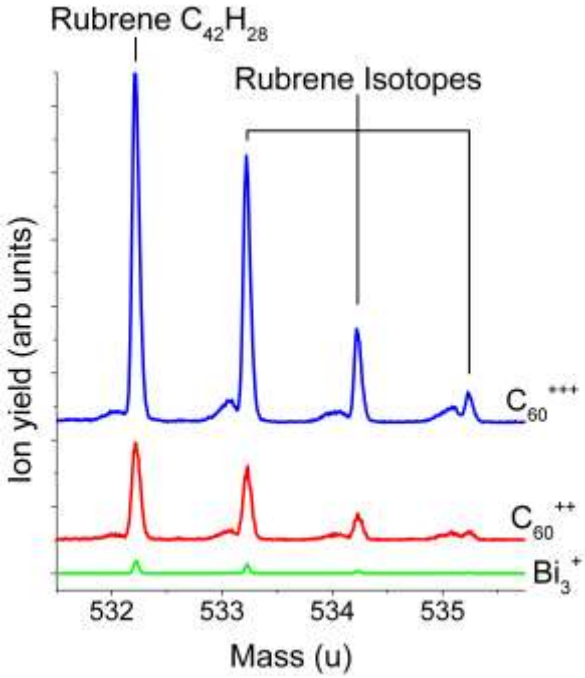

Figure 5-1 ToF-SIMS acquired mass spectra showing the peaks of the rubrene ion and its isotopes. The spectra was obtained using 3 different primary ions in order to deduce the best beam for studying rubrene surfaces. For clarity the spectra have been offset on the y axis, (Ion yield is calculated as the ion intensity divided by the primary ion dose for the respective analysis beam).

From Figure 5-1 it can clearly be seen that the primary ion beam which produced the greatest yield from the surface of rubrene was the C_{60}^{3+} beam.

With respect to comparing the ion yields produced by the two C^{60} primary ion beams, the results in Figure 5-1 agreed with studies undertaken on other materials. These studies experimentally showed that the sputtering yields produced by a C_{60}^{n+} ion beam are directly proportional to n although no explanation of this behaviour was provided.[92] This was observed on sucrose thin films, trehalose, and Ag substrates.

When considering Bi_3^+ it is clear that the yield produced over a prolonged measurement is far less than both C_{60} beams. It should be noted that at lower primary ion dosage, Bi_3^+ showed an increased flux of secondary ions greater than that of the two C_{60} beams. The intensity of the secondary ion count rapidly dropped to the background count by the time a dose density of 1×10^{12} ions·cm^{-2} was reached as can be seen in Figure 5-2.

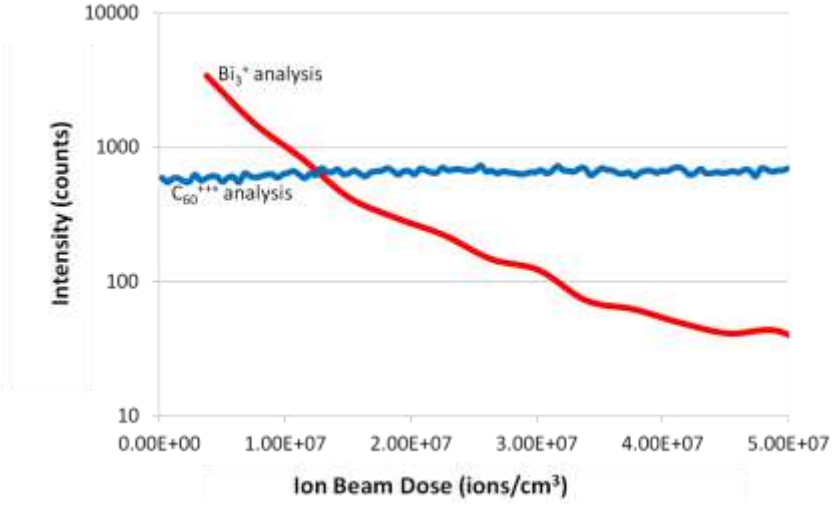

Figure 5-2 Plot showing the intensity of rubrene secondary ions with respect to primary ion beam dosage for Bi_3^+ and C_{60}^{3+} primary ions beams.

The diminishing rubrene ion signal indicates that the Bi_3^+ ion beam is causing physical and chemical modifications to the exposed surface.[93] Interestingly, the ion beam doses were still below the nominally quoted static limit of 1×10^{13} ions·cm^{-2} for polymer materials.[94]

The greater C_{60}^{3+} ion yields remain stable past doses of 1×10^{10} ions·cm^{-2}, indicating the static limit was not reached and surface damage did not occur. This agrees with the AFM images in Figure 5-3 which show the surface of an area analysed by ToF-SIMS and a nearby area which was not analysed. The primary ion dose density used was 1×10^{10} ions·cm^{-2}. Damage to the surface which has been seen when using the C_{60} beam includes the deposition of carbon on the surface and the removal of large amounts of sub surface material, destroying the surface integrity. This result is consistent with previous SIMS studies of other organic molecules where it

is understood that cluster sources are required for successful removal of large molecules.[95, 96, 97] Molecular dynamic simulations have also shown that the large C_{60} cluster ions do not penetrate deeply, instead removing large areas of material from the surface. The use of the C_{60}^{3+} primary ion beam at large dose density allows a large data set to be amassed. This therefore potentially allows valid statistical data to be accumulated for relatively low concentrations of impurities.

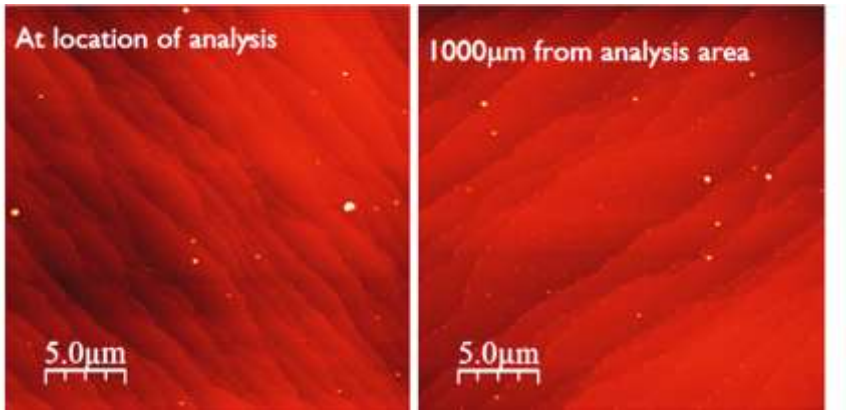

Figure 5-3 Two AFM images taken on the same sample, the AFM image on the left shows an area when ToF-SIMS analysis has occurred and the right shows an area away from the analysis. The AFM image shows no noticeable damage to the surface. The surface is still structured with monolayer steps of rubrene with similar roughening to those expected for an 'as-grown' sample. The primary ion dose density used was 1×10^{10} ions·cm^{-2}.

5.2.2 Mass spectrum at the surface of rubrene

The typical mass spectra obtained from the surface of rubrene are shown in Figure 5-4. The mass spectra were obtained using a C_{60}^{3+} primary ion beam with a beam current of ~0.01 pA. The analytical area was 300 µm × 300 µm with 16 × 16 pixels and a beam size of ~50 µm. Both negative and positive secondary ions were collected and are shown in the upper and lower spectra of respectively. In each case the number of ions incident on the surface was limited to 1×10^{10} ions·cm^{-2}; this insured statistically that each ion impacted an area un-affected by previous ion impact.

The two spectra clearly show different fragmentation patterns. In negative secondary ion mode the peaks with the highest yield are the small hydrocarbon fragments below m/z=150. Only a small peak is observed at m/z=532 corresponding to the rubrene molecular mass, $C_{42}H_{28}^-$. Negative polarity analysis reveals the presence of the electronegative rubrene peroxide ions at m/z=565 ($C_{42}H_{28}O_2^-$). In the positive secondary ion mode, again a range of fragments are observed in the lower m/z range but with much lower ion yields. The positive rubrene

molecular ion, $C_{42}H_{28}^+$ at m/z=532 is much clearer with a higher ion yield than in the negative

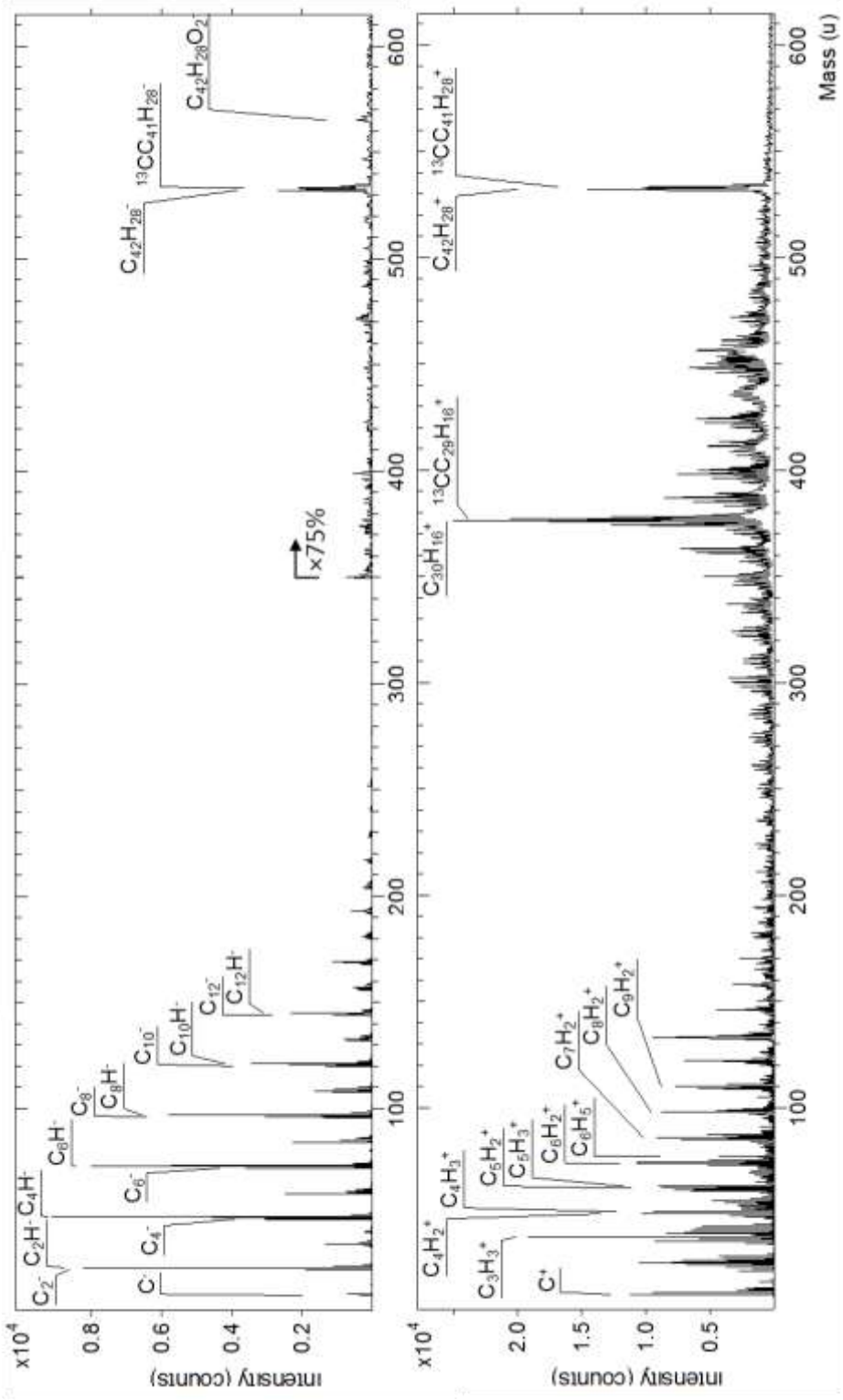

Figure 5-4 Rubrene mass spectra acquired by ToF-SIMS using a C_{60}^{3+} primary ion beam. The top spectrum shows all negative ions, allowing for tracking of electronegative oxide molecules. The bottom spectrum shows all positive ions.

regime, though the peroxide ion is now not observed. Fragmentation of the parent molecule is also clearly occurring in the positive regime, as the highest yielding ion is observed at m/z=376 ($C_{30}H_{16}^{+}$). This fragment appears to be the parent molecule of rubrene, with two benzene rings removed. This fragment is not observed in the negative ion mode. The positive secondary ion mass spectrum clearly shows that upon impact fragmentation does occur. The positive secondary ion mass spectrum shows preferential fragmentation of the molecule $C_{30}H_{16}$.

5.2.3 The effect of temperature on yield

It has been shown that a reduction of sample temperature can reduce the loss of molecular information and fragmentation of organic polymer based materials during SIMS.[93, 96, 98, 99] It was therefore conjectured that the effect may be similar on rubrene and the effect of temperature on analysis was investigated. The sample temperature was lowered to -150 ºC using liquid nitrogen in thermal contact with the sample stage. Mass spectra were acquired for a series of temperatures from -140 ºC to 20 ºC using a controlled heating stage. As can be seen in Figure 5-5, for the case of rubrene, a negligible temperature effect was observed for both polarities of ions. The reduction on temperature therefore had no effect on the physical properties required to improve the SIMS signal of rubrene single crystals.

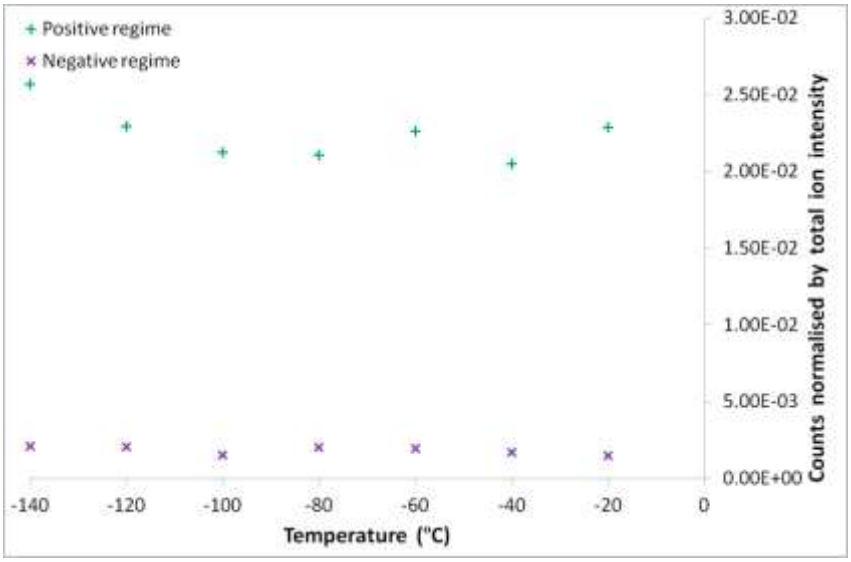

Figure 5-5 Plot showing the effect of temperature on the secondary ion yield of intact rubrene ions during ToF-SIMS analysis using C_{60}^{3+}. Temperature was seen to have negligable effect on the fragmentation and yield of the rubrene molecule.

5.3 Surface imaging

Ion mapping can be accomplished by rastering the analysis beam and building up a chemically resolved image of the surface as described in Section 3.3 . The C_{60} beam which was used in the

previous section for producing mass spectra over long acquisition times is not suitable for imaging. This is due to it large beam size, ~50 μm, imaging therefore was undertaken using the Bi beam. As discussed in Section 5.2.1 exposure of the Bi beam produces a loss in molecular integrity at the surface, even after relatively small primary ion beam doses. Due to this, throughout imaging, the secondary ion profile was monitored to insure the rubrene molecular signal did not drop to a back ground count.

5.3.1 Imaging of natural surface oxidation

After initial experiments successfully showed the possibility of producing ions maps of the surface of rubrene, analysis was under taken on an unintentionally oxidized surface. Ion mapping was carried out on a rubrene as-grown ab-plane surface. For high lateral resolution the Bi_3^+ ion beam was used. The ion beam current was ~ 0.1pA scanned over an area of 250 μm × 250 μm with 1024 × 1024 pixels. Negative secondary ions were collected to obtain a good signal from the electro negative oxide related molecules.

Figure 5-6 shows ion maps for each of the labelled ions. The pixel intensity in Figure 5-6 a) to e) indicates the number of the collected ions of each respective molecular species and their isotopes. The images have been normalized pixel by pixel with respect to the total ion count as discussed in the previous section. The total ion count (the entire recorded mass spectrum integrated at each pixel) is shown in Figure 5-6 f).

As expected we clearly see the presence of the rubrene molecule ($C_{42}H_{28}$) which is detected over the entire surface as shown in Figure 5-6 a). As well as the rubrene molecule four oxide related ions have been tracked, shown in Figure 5-6 b) – e). Rubrene oxide ions ($C_{42}H_{28}O^-$), Figure 5-6 c), are observed to exist almost uniformly over the entire surface with a small contrast seen. In comparison, rubrene peroxide ions ($C_{42}H_{28}O_2^-$), Figure 5-6 b), have a much greater contrast with an increase in counts at defined locations (brighter areas indicate a higher concentration of ions). It is believed that these locations correspond with the presence of crystal defects. These defects are also indicated (albeit with much lower contrast compared to Figure 5-6 b), d) and e)) in the preferential sputtering seen in Figure 5-6 f) which shows the total ion count, a good indicator of topography. In Figure 5-6 e) we map the presence of a molecule of mass 487 amu. It is believed that this corresponds to $C_{36}H_{23}O_2^-$, a rubrene peroxide molecule which has lost one of its exposed phenyl rings. This sort of fragmentation is likely to occur on the impact of primary ions. The molecule shows locally increased concentration in correlation with Rubrene peroxide, Figure 5-6 b). In Figure 5-6 d) we show the spatial variance of oxygen ions. It is speculated that these ions come from oxidised rubrene molecules which have completely fragmented on impact.

Again the correspondence with the areas of surface defects is clearly seen. Note the high relative count for oxygen containing species near defects; the majority of molecules detected at these spatial locations contain oxygen. In agreement to this locally increased concentration of oxidation, rubrene ions ($C_{42}H_{28}^-$), Figure 5-6 a), are depleted at the same locations.

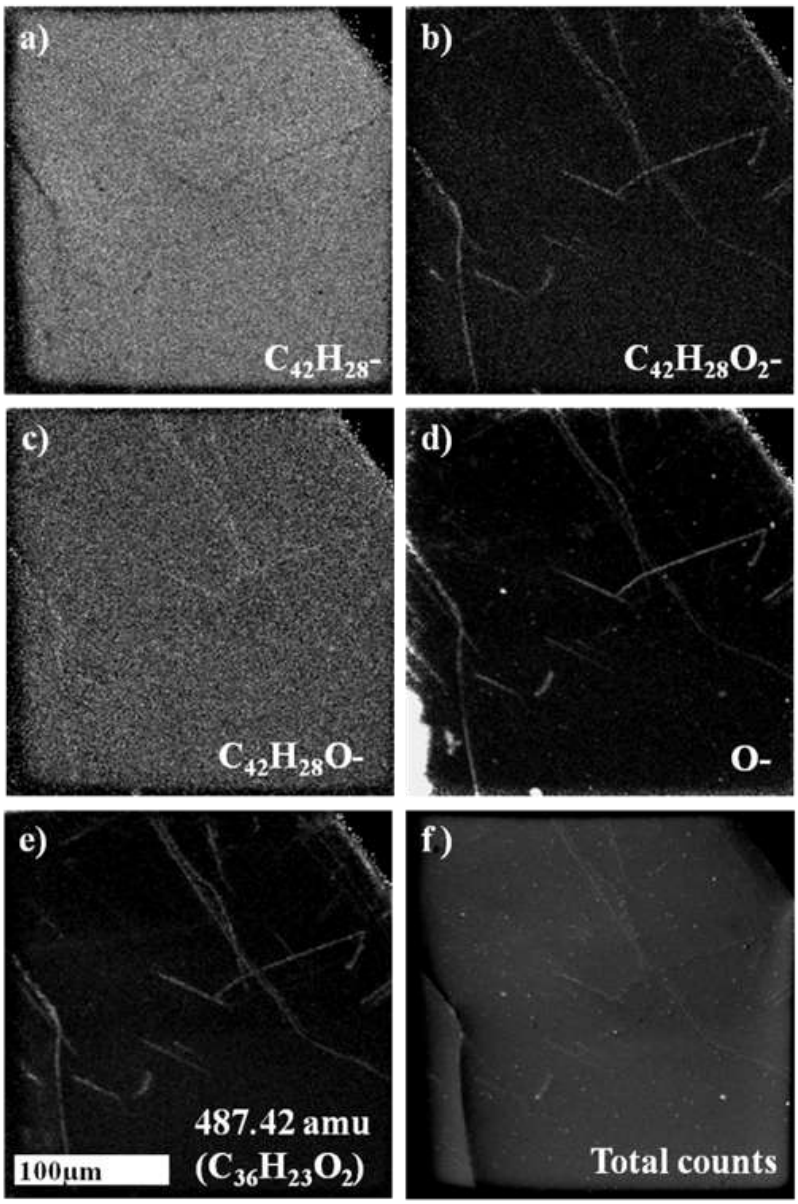

Figure 5-6 A series of ion maps each showing a 250 μm × 250 μm area of an as grown surface of rubrene. Each image spatially maps the intensity of the respective ion and its isotopes and is normalised pixel by pixel against the total counts image. The pixel intensity represents the normalized count intensity, with the exception of f) where total counts are represented. Pixel intensity runs from black being 0 to white being maximum normalized counts. The tracked molecule and maximum normalized counts for each respective figure are: **a)** rubrene 0.15; **b)** rubrene peroxide, 0.16; **c)** rubrene oxide, 0.1; **d)** oxygen, 0.50; **e)** 487.42amu (suggested to be $C_{36}H_{23}O_2$) 0.75 **f)** total counts.

The observation of local oxidation at the surface of rubrene is of importance, as oxidation is a degradation process which can potentially ruin electronic devices. We want to discover the location of localised oxidation and understand why these specific areas are preferred. The rubrene peroxide, oxygen and $C_{36}H_{23}O^-$ ions show a large contrast over the sample surface. By comparing these with the total ion count image, we can see topographical formations at these points, which would be typical of micro cracks, grain boundaries or other crystal defects. For rubrene peroxide to form in the crystal a steric deformation of the molecule is required. As discussed in Chapter 4 , this can occur at step edges. Or, as discussed by Mitrofanov *et al.*[38] and exemplified in the results seen in Figure 5-6, at the location of structural defects.

5.4 Depth profiling

Little is known about how surface oxidation may extend below the surface of organic single crystals and as of yet a suitable technique to probe this has not been devised. In understanding how the process of oxidation extends below the surface we aim to recognise its effect on surface and sub-surface conduction channels as well as gaining a better knowledge of the depth at which these conduction channels exist. One possible solution to investigating sub-surface oxidation is the use of higher energy primary ions to sputter away the surface, providing a means of depth profiling.

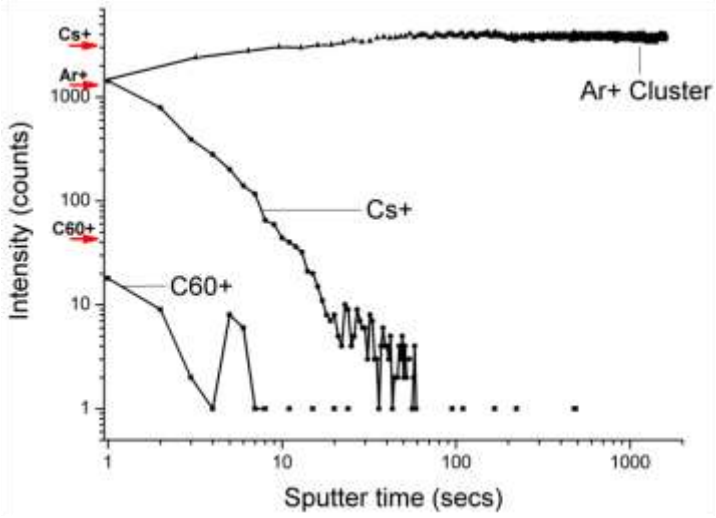

Figure 5-7 A plot of Secondary ion counts vs Sputter time. Respective primary ion beams are used to sputter away the surface interlaced with Bi_3^+ analysis. Arrows on the y axis indicate the initial intensity of the labelled sputter profiles. The C_{60}^+ and Cs^+ quickly damage the underlying surface destroying the whole molecule signal (note the x-axis is presented with a logarithmic scale).

Depth profiling of organic semiconductors is not a trivial matter due to the high possibility of damaging the underlying surface. Within the literature different ion beams are proposed for different materials depending on the structure and thicknesses.[100, 101, 102] However, in these previous studies SIMS depth profiling was not performed on any single crystalline organic materials

Within this study depth profiling was carried out using Cs^+, C_{60}^+ and Ar^+ cluster ion sputter beams. The angle of incidence for the Cs and Ar beams was 45°, whereas the C_{60} beam was 60°. The Ar cluster size was estimated to be ~2500 ions. In all cases the analytical beam was Bi_3^+. The sputter beam conditions for the depth profiling are shown below in Table 5-1.

Table 5-1 Sputter ion beam conditions used on rubrene

Ion Beam Species	Ion Beam Energy /keV	Ion Beam Current /nA	Analysis Area /(μm)²
Cs^+	0.5	75	300
C_{60}^+	10	1.0	500
$Ar_{\sim 2500}^+$	5	1.5	300

A dramatic difference between the three sputtering ion beams is observed in Figure 5-7: In the case of both Cs^+ and C_{60}^+ ion beams, the rubrene molecular signal is lost very quickly. For the C_{60}^+ ion beam this occurs in the first 10 seconds, whereas the Cs^+ ion beam does little better, a stable rubrene signal is never obtained and after 20 seconds of sputtering the signal is gone. Impressively the recently developed Ar cluster ion beam†† is able to maintain the bulk molecular ion signal. The rubrene signal remains constant over the length of the analysis, up to a total sputter depth of 5 μm, indicating that the molecule is being sputtered intact.

It is suggested that the use of very large Ar cluster ion beam means that upon impact, the energy of the ion beam is distributed over the whole of the cluster. In this instance the Ar ion beam impacts the rubrene with approximately 2 eV/atom, compared to 50 eV/atom and 166 eV/atom for the Cs and C_{60} ion beams respectively. Most of the beam energy is deposited in the subsurface region of the rubrene, and deeper layers of the material remain undamaged from the ion beam impact. The decrease in kinetic energy leads to an increase in the ratio of ejected intact molecules to fragments.

†† The Ar_n^+ cluster beam is a new development for the ToF-SIMS instrument. Experimental data was therefore undertaken at IONTOF and the National Physics Laboratories. The formation of Ar_n^+ clusters was first successfully undertaken by Seki *et al.* in 2006,[108] Who have explained the formation of clusters is accomplished by the condensing of molecules during adiabatic cooling of high pressured Ar gas.

5.5 Extended studies of oxidation

5.5.1 Imaging of local anodic oxidation

For initial experiments a sample was prepared that would contain a known chemical element. To accomplish this local anodic oxidation of a rubrene sample was performed. This would provide a trace of oxygen in a known location on the surface.

Local anodic oxidation was performed using an AFM. The process involves a voltage being applied between the sample and the tip, as in C-AFM. When the voltage is large enough and an oxidant is present, an oxidation reaction is induced.[103, 104] The oxidant in this case is water vapour present in the air, which condenses on the surface of the sample. It was therefore important to ensure a high humidity for local anodic oxidation to occur. By scanning the tip, while held at voltage, it was possible to draw an image, in this case a filled rectangle. To ensure successful oxidation it was important to have a small tip velocity and a high voltage.

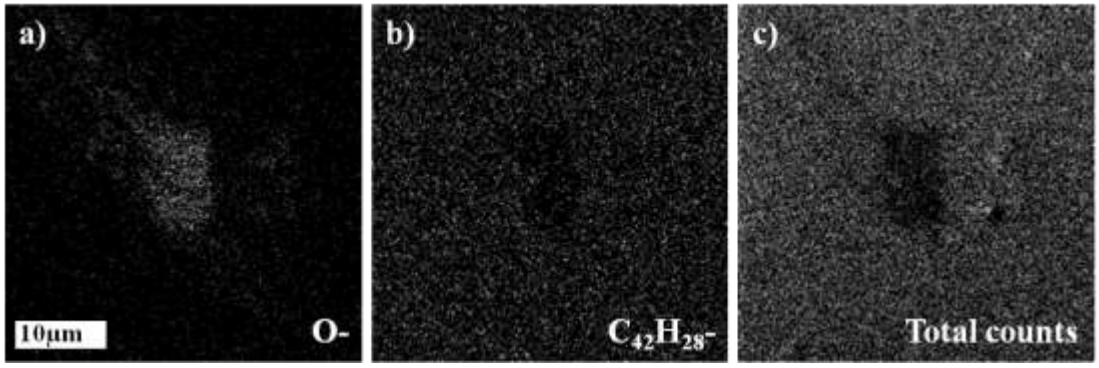

Figure 5-8 Three ion maps tracking the intensity of the labelled secondary ions over an analysis are of 40 μm × 40 μm at the surface of rubrene. The surface has intentionally been oxidized by local anodic oxidation. a) and b) have been normalized pixel by pixel with respect to the total counts. The grey scale (black to white) shows the normalize intensity for a) 0 - 0.122, O^- and b) 0 – 0.097,$C_{42}H_{28}^-$ and total intensity for c) 37.875 – 75.00, total counts.

Figure 5-8 shows the ion maps acquired at the area of local anodic oxidation. In order to track the oxygen signal acquisition was undertaken in the negative regime. It can be seen in Figure 5-8 c) that the total amount of counts at each pixel is not homogeneous over the analysis area. This can be caused by several effects such as preferential sputtering, due to topography, or a change to the structural or chemical matrix, making the ionization and liberation of surface molecules more or less likely, known as a matrix effect. To take account for any preferential sputtering, each chemical specific map produced was normalized pixel by pixel with respect to the total counts.

It can be clearly seen in Figure 5-8 a) that the oxygen signal is increased in the area where local anodic oxidation occurred. Less obvious, but never the less present, is the reduction in the rubrene molecular signal ($C_{42}H_{28}^-$) at the same area seen in Figure 5-8 b). Interestingly there was no obvious variation in the oxidized rubrene signal for either $C_{42}H_{28}O^-$ or $C_{42}H_{28}O_2^-$. This implies there was no chemical reaction between oxygen and rubrene, and the oxygen was incorporated into interstitial sites in the crystal. Such a process occurring during local anodic oxidation is unexpected and not observed on other crystalline semiconductors.[105] This leaves an interesting open question which requires to be addressed in future studies.

5.5.2 3D Imaging

After determining the best primary ion sputtering beam was $Ar_{\sim 2500}^+$, initial experiments were undertaken to measure the 3D distribution of chemical elements. This was undertaken using the ION-TOF V machine at The National Physic Laboratory. The fragmentation of rubrene was different when the surface was subjected to $Ar_{\sim 2500}^+$ bombardment. Understanding the origin of fragments and their parent molecule is not a trivial matter and will need the consideration of theoreticians before a full understanding of the 3D distribution of ions can be accomplished.

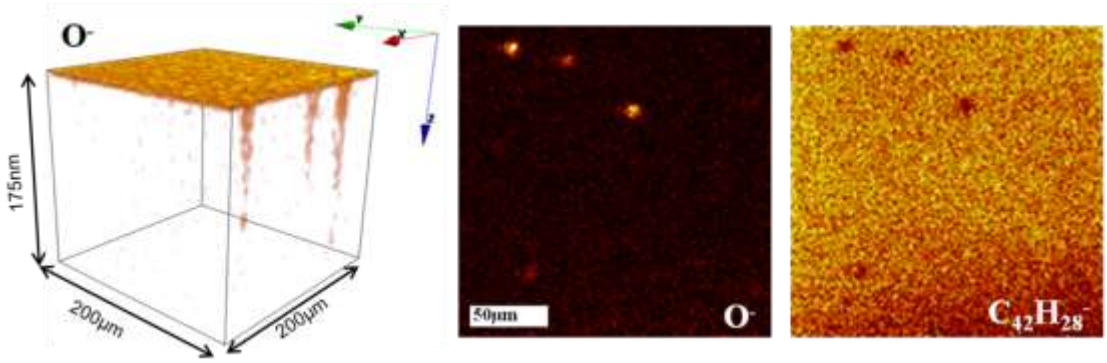

Figure 5-9 Initial depth profiling of cleaved rubrene (approximately 1 year after cleaving) 200 μm × 200 μm × ~175nm. The right two images show ion maps for the respective ions, these are summed over the entire depth analysed and normalized by the total counts at each pixel. The left image shows a 3D reconstruction of the O^- ion distribution to a depth of ~175 ± 25 nm. Features can be seen which extend below the surface. The analysis beam used was Bi_3^+ and an Ar_{2500}^+ sputter beam.

The rubrene molecule was strong enough to track and it was seen that for the depth measured (~175 nm) it remained constant as with the previous study, shown in Figure 5-7. Interestingly oxygen ions were present, as can be seen in Figure 5-9 these existed uniformly across the material for the first few monolayers. Below this oxygen ions were not present except at the

location of defects penetrating into the material. These defects are clearly seen in the 3D representation and summed oxygen ion map in Figure 5-9. The defects are also indicated by the depletion of rubrene as shown in the summed $C_{42}H_{28}^-$ ion map. Interestingly the distribution of rubrene peroxide did not correspond to the distribution of oxygen or rubrene and had a uniform distribution which was unaffected at the location of the defects. This raises an uncertainty to the origin of the O^- ions and is not dissimilar to the results seen in the local anodic oxidation study.

The data presented in Figure 5-9 shows the possibility of using this technique to investigate the subsurface effects of oxidation. Before a conclusive study can be accomplished though, further study needs to be undertaken to produce a full understanding of the effects of $Ar_{\sim 2500}^+$ bombardment on the fragmentation of molecules.

5.6 Conclusions

The data presented in this chapter was the first reported ToF-SIMS analysis on an organic single crystal surface.[87] A spatial profile of the rubrene surface shows the existence of a uniform coverage of rubrene-oxide, along with local increased concentration of rubrene-peroxide occurring at areas of topographical variance. These areas are believed to be crystallographic defects. We note that these are not observed in an optical microscope. The presence of the locally increased oxidation supports previous findings which suggest that oxygen can only be incorporated into molecules of single crystal rubrene at locations allowing for steric deformation of the molecules.

The experiments detailed show that ToF-SIMS studies of an organic single crystal require different experimental considerations in comparison to other studies on organic molecules. This is highlighted by the lack of temperature dependence seen within rubrene. These material specific considerations are also highlighted by the necessity for varying the primary ion beams, depending on the regime being used, either mass spectroscopy, spatial profiling or depth profiling. The study presents C_{60}^{3+}, Bi_3^+ and Ar cluster sources as the preferred primary ion beam in each of these respective regimes.

One application of ToF-SIMS that should be of particular value for the development of organic electronics is the study of surface degradation on organic crystals, particularly via oxidation. By combining the sputtering and spatial profiling techniques, further studies can produce a full understanding on how oxidation penetrates into the material. This can further lead to an understanding and modification of conduction paths at and near the surface of rubrene. By also

striving to reach the resolution limits of spatial profiling, it is hoped to study the chemical composition of nanoscale features resulting from local oxidation.

Chapter 6

Photoluminescence confocal microscopy

Within this chapter I present experimental details and describe the optical configuration for a scanning confocal microscope designed to image both the intrinsic and defect driven nature of excitons within rubrene. In order to achieve this, an experimental instrument has been designed to produce excitation by two-photon absorption. The instrument can independently measure the spatial distribution and spectra of the resulting photoluminescence (PL).

6.1 Experimental design

To probe the intrinsic nature of excitons in rubrene (not affected by the presence of defects), photoexcitation should occur within the bulk of the material. Probing within the bulk avoids the possibility of commonly occurring surface defects caused by factors external to the crystal. In order to do this, two-photon (2P) excitation was used. In 2P excitation the transition energy is twice that of a single absorbed photon, as shown in Figure 3-5. The material is therefore transparent to a single photon and only at the focal point of the excitation beam is the density of photons high enough for excitation to be of significance.

To map the PL the acquisition optics were set up in a confocal arrangement with a scanning aperture, positioned in the imaging plane. A schematic showing the optical set-up is presented in Figure 6-2. The laser light entered through a 'hot' mirror[#] which acted as a long pass filter. This allowed light of wavelengths longer than 700 nm to pass through and reflected shorter wavelengths such as that of the PL.

The excitation laser was a pumped Ti-Sapphire laser mode locked to produce a 100 fs pulse at 76MHz and was tuned to 800 nm. As currently there is no reported 2P absorption spectrum for rubrene[§§] an 800 nm excitation wavelength was chosen as it had successfully been used in 2P excitation experiments undertaken by Mitrofanov *et al.*.[30] I am currently undertaking further

[#] A 'hot' mirror is termed as such as it allows the larger wavelength IR to pass through the component.
[§§] Current experiments are being undertaken to plot the 2P excitation spectrum. These will provide a more appropriate wavelength for future studies allowing more efficient excitation.

studies to provide a 2P excitation spectrum. The same microscope objective was used for focusing the excitation beam and acquisition of the PL. The objective used had a quoted 40 × magnification with a numerical aperture of 0.5. The PL was guided by mirrors to a focusing lens which converged the light onto the second focal point of the system. An aspherised achromatic lens was used to ensure minimal chromatic and spherical aberrations. The lens had a 25 mm diameter with a 50 mm effective focal length. The PL was focused onto an imaging plane within which a fibre masked by a pinhole aperture selected the PL to be measured. The single mode fibre functioned at wavelengths up to 800 nm with a cut off at 550 nm. To ensure light only coupled to the core of the fibre the 3 μm pin-hole was affixed directly onto the cladding above the core. The pinhole ensured a high resolution could be obtained by minimising the cross section of focused light collected in each measurement. The far end of the fibre was coupled into a spectrometer where the spectrum of the collected PL was recorded. To ensure no laser light entered the spectrometer, a short pass filter prevented any light of wavelengths longer than 690 nm being coupled out of the fibre.

To create a map of the PL, the pinhole and fibre were mounted on a translation stage which was computer controlled with sub-micron resolution. The system was designed so that by scanning the fibre in X,Y and Z, a 3D map of the PL could be produced.

The spectrometer used was a Horiba Jobin iHR 320 with a diffraction grating of groove density 300 G/mm and maximum resolution of 0.043. A CCD array was used to capture the spectrum this was a Princeton instruments pixis CCD array with 1340 x 100 pixel sensor and was cooled to -50°c suing the internal electronic air cooler. Using a CCD array allowed the entire spectrum of rubrene to be recorded in a single exposure with the spectrum projected across the 1340 pixel width of the array. The conversion of pixel number to wavelength was calibrated using a Neon lamp, the calibration spectrum can be seen in Figure 6-1. The fit was undertaken using the Polyfit function in MatLab, (Thanks are given to Alex Macfaden for performing this) 7 identifiable peaks were used for the fit. From the calibration curve a conversion equation was derived. Wavelength could be converted from pixel location using $\lambda = 0.199p + (\lambda_m - 670)$ where p is the pixel number running from 1-1340, and λ_m, the central wavelength which was entered using the spectrometer controll software. For measuring the spectrum of rubrene λ_m, was set to 600nm

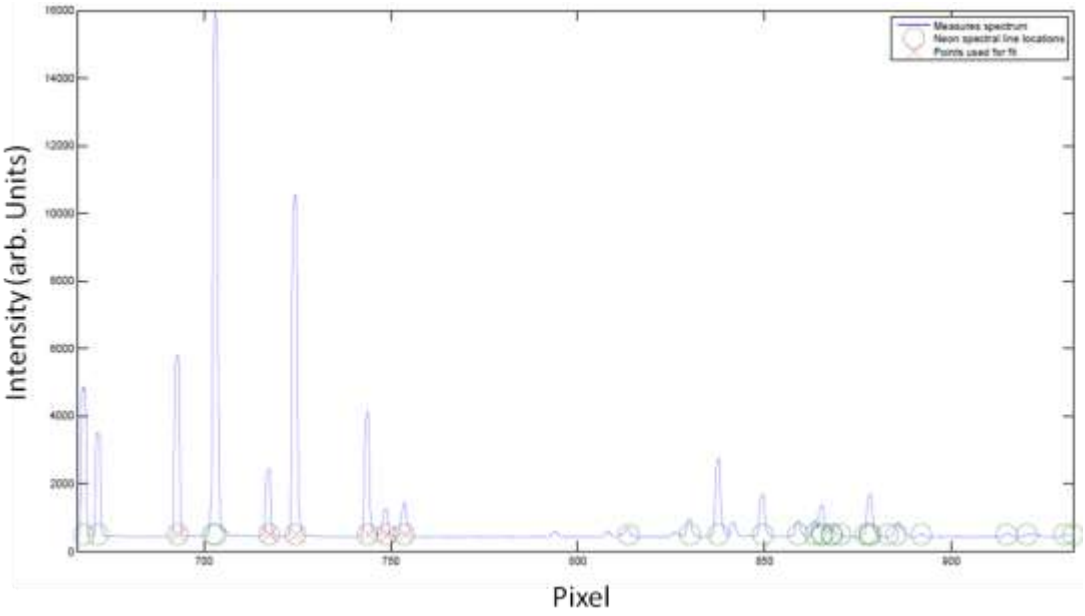

Figure 6-1 Neon lamp spectrum measured using the spectrometer and CCD array set up used to calculate the pixel to wavelength conversion equation. (Plot produced by Alex Macfaden.)

Figure 6-2 Diagram of the optical arrangement used in the two-photon scanning confocal microscope. The laser (800 nm) enters through a 'Hot' mirror which is transparent to light of

wavelengths greater than 700 nm and reflective to those below. The laser is focused with the same optical objective which collects the PL. The PL is guided through a confocal arrangement and projected on an imaging plane. A scanning pinhole and fibre spatially select the acquired PL.

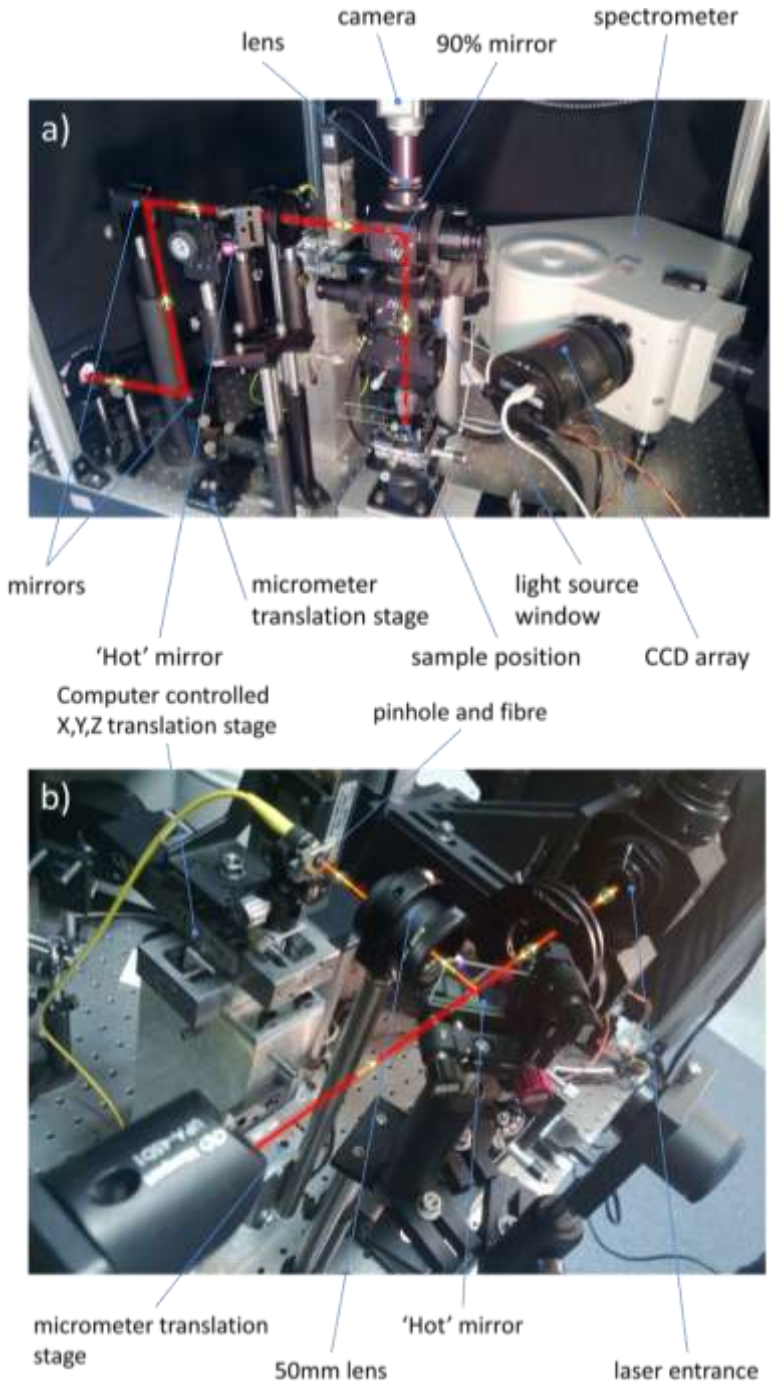

Figure 6-3 Two photographs showing the experimental set-up of the two-photon scanning confocal microscope. Beam paths are superimposed. A periscope arrangement raises the excitation beam to the level of the microscope. The laser beam is focused on the sample and the resultant PL is collected using the same optics. The PL is guided to the 'hot mirror' where it is reflected and then projected onto an imaging plane.

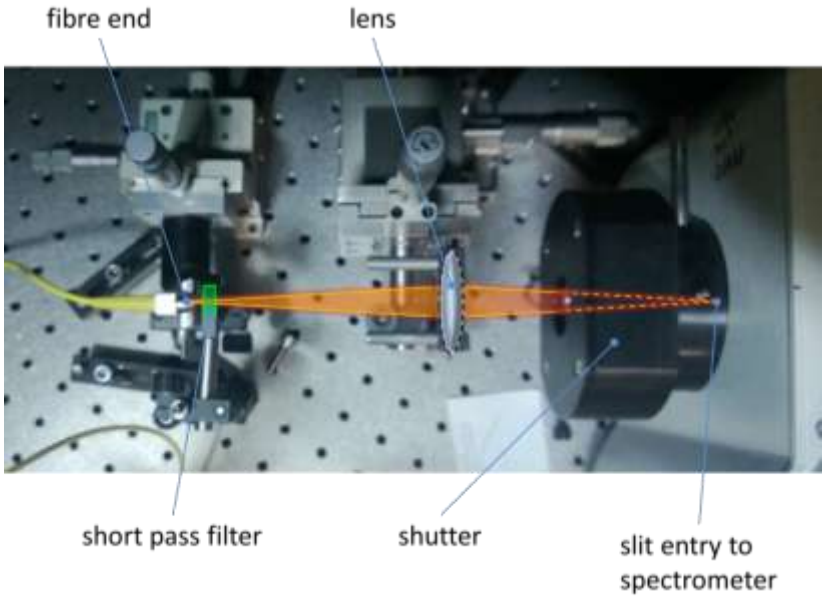

Figure 6-4 Photograph detailing the optical coupling of the photoluminescence from the fibre to the spectrometer. The short pass filter prevents any laser light from entering the spectrometer. The lens and spacing is selected to match the numerical aperture of the incident light with that of the spectrometer. The light path is superimposed

Figure 6-3 shows two pictures of the optical configuration. A periscope arrangement raised the excitation beam to the level of the microscope entrance. Once within the microscope the excitation beam was reflected down at the sample. The camera positioned directly above the microscope, labelled CCD in Figure 6-2, was used for alignment of the sample. To allow illumination during alignment, a light source was input through the 'light source window' and directed at the sample by the addition of a 50% mirror which was slid in and out for alignment and measurements respectively.

The spectrometer and CCD array used to record the PL spectrum can be seen within Figure 6-3 a). In order to reduce noise the CCD array was cooled to a temperature of -50 ºC. By using a CCD array the entire spectrum could be recorded in one exposure, reducing the acquisition time of the experiment.

Figure 6-4 shows the experimental setup at the spectrometer end of the fibre. A lens refocused the light emitted from the fibre onto the entrance of the spectrometer. The numerical aperture of the refocused light was matched to that of the spectrometer. The mechanical shutter controlled the exposure time of the CCD and a slit regulated light entering the spectrometer.

The entire optical system was contained within a black box to ensure minimal interference from external light sources.

6.2 Characterisation of the experimental system

In order to analyse the data and understand its relevance to the excitonic nature of rubrene, it was important to first characterise the optical system. Characterisation of the system involved calculating the magnification in order to define feature sizes. Estimation and measurement of the system's resolution was also required as any imaged feature would be a convolution of the resolution and the feature. In order to conclude if exciton diffusion was occurring, it was also important to estimate the size of the excitation beam.

The magnification of the system was calculated by imaging a reference grid of known periodicity[***] which was illuminated from behind. The fibre was replaced with a CCD and the resultant image can be seen in Figure 6-5. The magnification of the system was calculated using Equation (**6-1**).

$$\boldsymbol{M = \frac{\Delta X}{\Delta x}} \qquad (6\text{-}1)$$

Δx is the size of the reference measurement in the focal plane of the microscope objective (0.04 mm), in this case a multiple of the grid's period. ΔX is the size of the reference measurement in the imaging plane, this was measured as 0.38 mm giving a magnification of M=9.5.

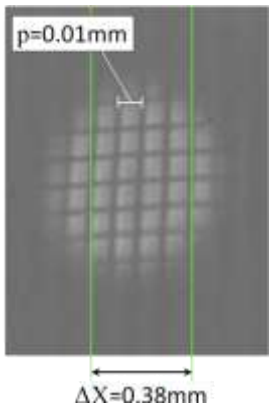

Figure 6-5 Image of a back illuminated reference grid with period 10 μm, ΔX is the distance between the two green lines in the imaging plane.

The size of the excitation spot produced by the focused laser beam was calculated by assuming a uniform wavefront illumination of the entire microscope objective. This assumption was made as the laser beam was clipped and the incident light wavefront resembled more a plane wavefront than a Gaussian beam. It is well known that the point spread function of a focused

[***] The reference grid used is chrome on glace grid array with a period of 10 μm. Thorlabs R1L3S3P.

plane wavefront is an Airy disk pattern. More information on the airy pattern and its formation can be gained from Chapter 10 of Hecht.[106] The intensity profile, $I(x)$, of an Airy disk is described by Equation (**6-2**). Where $I(0)$ is the maximum intensity, J_1 is the 1st order Bessel function, NA the numerical aperture and λ the incident wavelength. The calculated normalised intensity profile can be seen in Figure 6-6.

$$I(x) = I(0)\left(\frac{2\,J_1\left(2\pi\,\mathrm{NA}\,x/\lambda\right)}{2\pi\,\mathrm{NA}\,x/\lambda}\right)^2 \qquad (6\text{-}2)$$

As the excitation process required the interaction of 2 photons, the probability of excitation scaled with the square of intensity. Figure 6-6 shows the excitation probability distribution over the Airy function. Both functions were calculated for a 0.5 numerical aperture with an 800 nm excitation wavelength as used within the study. The full width half maximum (FWHM) of the excitation beam was calculated as 0.8 μm and the FWHM of the probability distribution was 0.6 μm.

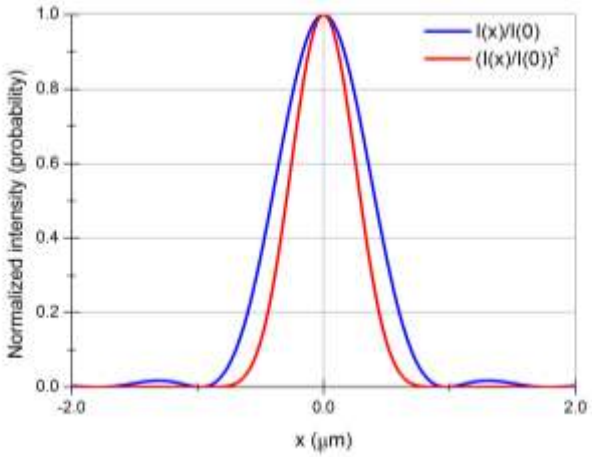

Figure 6-6 Blue - Normalised intensity profile of the focused excitation beam, calculated as an airy disk with numerical aperture 0.5 and wavelength 800 nm. Red – square of the Intensity profile giving a profile of the normalised probability of excitation.

Using the same equation and by substituting λ with 700 nm (approximately the longest wavelength within the PL spectrum) the resolution of the objective when collecting PL was calculated. This gives a FWHM of 0.7 μm. The same calculation was performed on the focusing lens to estimate the resolution of the projected image. The numerical aperture in this case was approximated as the ratio of the focal length and radius of the incident light beam. The incident beam was limited by the aperture of the microscope objective. For the 50 mm focal length used, a numerical aperture of 0.05 was estimated. This gave an airy disk FWHM of 7.2 μm. Using the

calculated value of the magnification this corresponded to a value 0.76 μm at the focal plane of the microscope objective and was the calculated resolution of the imaging system.

6.3 Determining the location of the surface

In order to record data at both the surface and within the bulk, it was important to devise a method of accurately locating the surface.

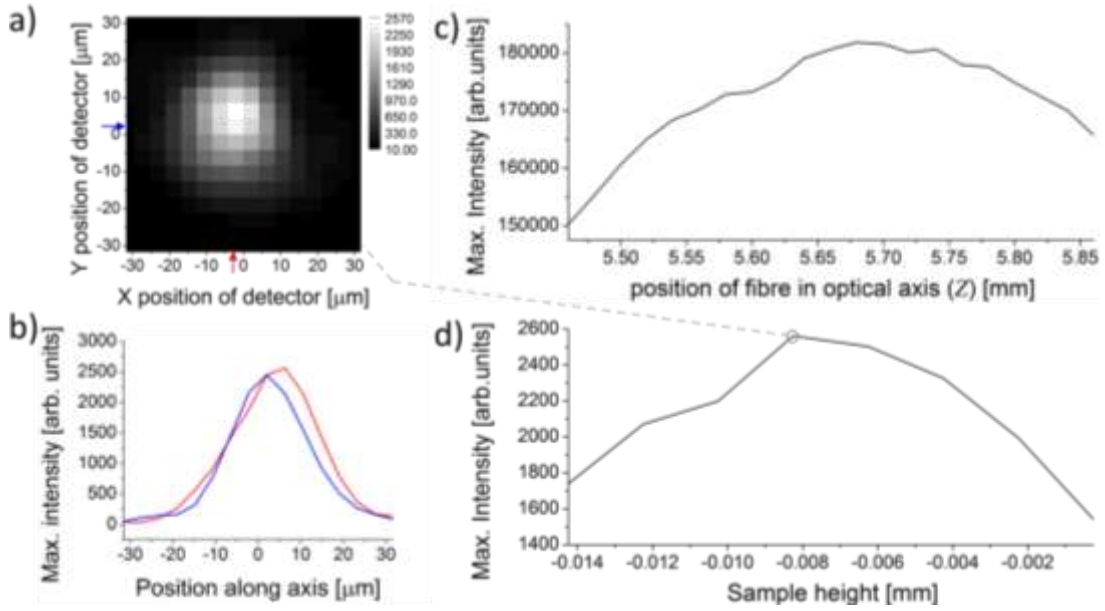

Figure 6-7 Imaging of the reflected laser beam in order to locate the surface of rubrene. **a)** Image of the laser beam reflected from the surface, each pixel represents the peak intensity of the spectrum. **b)** Profiles at the marked X (blue) and Y (red) positions. **c)** Plot of maximum pixel intensity against Z fibre position for a collimated beam incident upon the imaging lens. The Z position of the fibre is relative to the origin of the translation stage. **d)** Maximum pixel intensity plotted against sample height for a set of images of the laser beam reflected from the surface of rubrene. The detector is positioned at the maximum of plot c).

The data shown in Figure 6-7 details the method used for determining the location of the surface of rubrene. The reflected laser beam was used to determine when the surface of the sample was within the focal plane of the system. The fibre and pinhole (from herein referred to as the detector) were positioned in the focal plane of the imaging lens. This position was determined by illuminating the imaging lens with the collimated laser beam. The Z position of the detector was then scanned to locate the maxima as shown in Figure 6-7 c). Once positioned at the maxima the detector was within the imaging plane of the system. The sample was then illuminated with the laser and the reflected light imaged. Images were recorded as the sample height was scanned. When the image had maximum intensity and minimum spot size the surface was within the focal plane of the microscope objective and any photo excitation which occurred will be at the

surface. Having located the sample height at which the laser was focused on the surface this sample position was then used as a reference to determine the depth at which any future excitation occurred.

Of note in Figure 6-7 a) and b) is the image size of the reflected laser beam, the FWHM of which is 24 μm in the X direction and 25 μm in the Y direction. This corresponds to an average of 2.6 μm at the sample surface, a FWHM approximately three times larger than the calculated resolution of the system. The reflected laser beam was the smallest feature which can be produced within the imaging plane of the system and therefore an experimental measure of the system's resolution. The disparity between the calculated resolution and the measured resolution can be attributed to the assumption of perfect lenses. Any effects of spherical or chromatic aberration were ignored within the calculations. As will be shown later, although the resolution was less than the ideal system it was sufficient to see the effect of exciton diffusion.

6.4 Photoluminescence data

PL spectra were recorded at several positions both at the surface and within the bulk of as-grown rubrene samples. Figure 6-8 shows a typical photoluminescence spectrum recorded within the bulk of the sample. The confocal microscope system had a relatively small signal to noise ratio with only a small amount of the PL being coupled to the spectrometer for each detector position. To increase the signal to noise ratio Figure 6-8 shows an average of several spectra all acquired from a 1 μm × 1 μm area at the centre of the PL distribution.

The CCD detector had a combined read and dark noise offset which formed the baseline of the spectra, this is clearly seen in Figure 6-8 at an intensity of approximately 423. The transmission cut off point of the spectral filter at approximately 690 nm is also clearly seen with a sharp drop in intensity. The spectra shows a strong resemblance with previous reported data such as that discussed in Section 2.3.1 and as reported by Irkhin *et al.*,[56] Mitrofanov *et al.*,[30, 38] as well as many others. The maximum of the spectra is located at approximately 607 nm. This agrees with Irkhin *et al.* who show a dominant peak at 608 nm and Mitrofanov *et al.* who see a peak at 605 nm dominate the spectra at temperatures above 100 K. Within the spectra in Figure 6-8, a shoulder is present at shorter wavelengths located around 565 nm. This corresponds to the c axis polarised spectral band which Irkhin *et al.* report as being centred at 558 nm and Mitrofanov *et al.* see centred at 568 nm. The c component can enter the ab-polarised PL spectrum by scattering of light within the crystal and also by the collection of non-normal light in the numerical aperture of the microscope objective. As we move to longer wavelengths and lower energies the spectrum becomes less resolved. At these wavelengths vibronic modes start to overlap with other spectral

bands and due to the broadness of the spectrum we are unable to resolve these individual peaks. It is at these wavelengths that the presence of a peak has been reported to correlate with the presence of defects. This is shown by Mitrofanov *et al.* at a wavelength of 646 nm, and Chen *et al.* at a wavelength of 650 nm. The dominance of this peak is not seen in Figure 6-8 and therefore it is likely that the emission at these wavelengths is due to vibronic components. However, as will be shown later the presence of defects within the material increases the intensity of emission at these wavelengths with respect to the other spectral components.

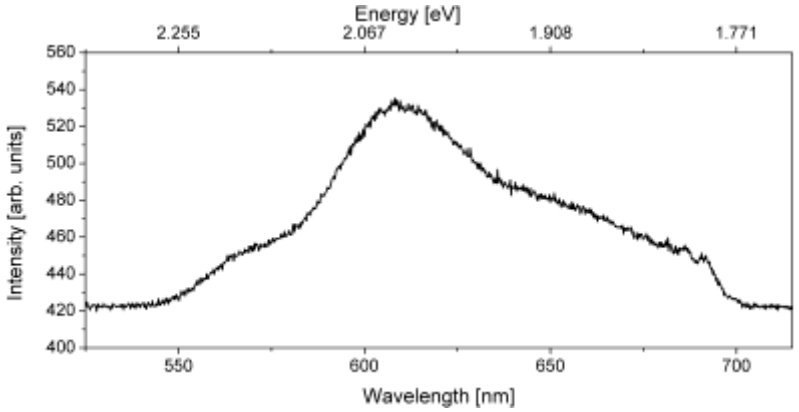

Figure 6-8 Photoluminescent spectrum acquired from ~40 μm below the surface. To increase the signal to noise ration the spectra is an average of multiple spectra recorded at 25 detector (pinhole and fibre) positions located in a 1 μm × 1 μm square at the centre of the PL distribution.

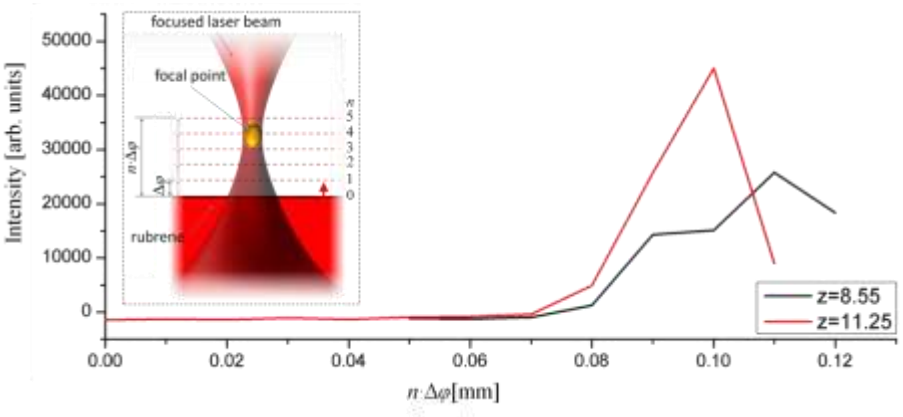

Figure 6-9 PL integrated intensity plot for increasing sample height recorded at two positions of the detector within the optical axis. The insert shows a schematic of the experiment undertaken. The related PL spectra and distributions can be seen in Figure 6-10 .

To understand the effect of focussing the excitation beam within the sample the PL distribution and spectra were recorded as the sample was incrementally raised and the focal point of the beam entered the sample. The insert of Figure 6-9 describes the experiment with the main plot

showing integrated PL intensity against sample height. The PL intensity is seen to rise indicating the sample height at which the beam is focused within the sample and excitation becomes probable. This experiment was carried out for two different z position of the detector.

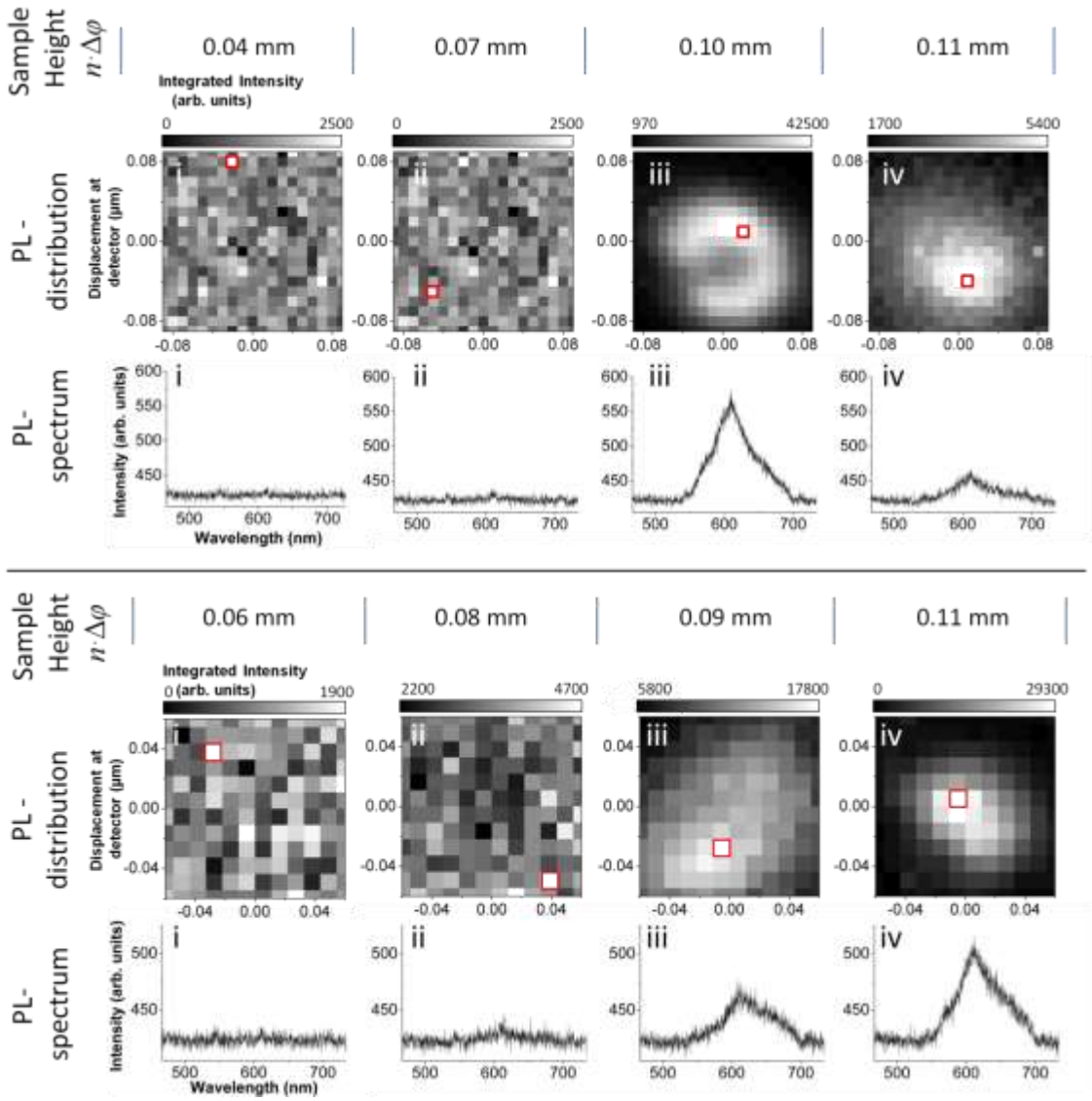

Figure 6-10 PL spectra and images for several sample heights. The top set of data show the spectra and images for the indicated labelled sample heights with a relative detector height of 11.25 mm, the red outlined pixels in show the location from which the respective PL was acquired. The lower set of data show the images and spectra for a relative detector height of 8.55 mm (the 0 mm height is furthest away from the imaging lens).

Figure 6-10 shows PL spectra and maps acquired as the sample surface was raised through the focal plane of the microscope objective. PL maps and PL spectra were recorded at each labelled sample height. The data displayed in the top portion of Figure 6-10 was recorded with a detector position 2.7 mm closer to the lens than the data presented in the lower portion. The pixel

intensity represents an integral of the entire PL spectrum for that respective location. Figure 6-9 clearly shows that 2P excitation only occurs within the high intensity focal point of the laser. This is indicated by the lack of PL at sample heights below 0.08 mm, at these sample heights the laser is focused above the crystal's surface.

Both sets of PL maps show the shape of the PL distribution changing with sample height. This variation was due to the introduction of spherical aberrations as the excitation beam was refracted at the surface of rubrene. Figure 6-11 shows how as the laser beam was refracted, the focal point would move deeper into the crystal with respect to the original focal length. The tight focal point would also become smeared out. As the sample surface was raised, and the angle of refraction therefore increased, the amount by which the focal length was shifted and the focal point smeared would increase. This shift in the position of excitation would in turn shift the imaging plane in which the PL distribution was projected. This led to the unusual variance in PL distribution which can be seen within Figure 6-10 .

The effect of spherical aberrations in shifting the imaging plane made it necessary to determine the correct Z position of the detector before acquiring PL measurements from within the bulk. This was done by first raising the sample to the desired position and then recording several PL maps at different Z positions of the detector. The detector was at the correct Z position when the PL had maximum intensity coinciding with the smallest distribution profile.

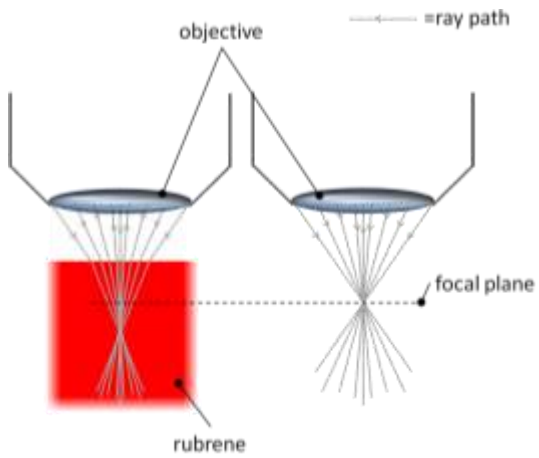

Figure 6-11 Schematic showing the effect of spherical aberrations. Left shows the case for focusing into rubrene (modelled Snell's law for a refractive index of 1.5)

Figure 6-12 shows the PL distribution and spectra recorded within the bulk, a) and c), and at the surface, b) and d). Both sets of data were acquired for the same sample. The surface in both cases was located by measuring the intensity of the reflected excitation beam. The bulk

measurements were recorded with the sample raised by 40 μm. In all cases the Z position of the detector was determined by finding the location at which the PL intensity was maximum and the spatial distribution minimum. The presented spectra in Figure 6-13 were acquired from the respective colour outlined pixels. Contour lines are shown at 75%, 50%, 25% and 5% of the maximum intensity.

The average full width half maximum (FWHM) of the bulk PL distribution profiles shown in Figure 6-12 a) and c) are 4.5 μm and 4.8 μm respectively. This FWHM is greater than that quoted for the resolution of the system (2.5 μm). As the excitation profile is smaller than the resolution limit, the PL therefore shows a distribution which is greater than the region of excitation. By comparing the PL distribution at both the surface and within the bulk, it can be seen that the size of the distribution increases within the bulk. The PL distribution recorded at the surface had an average FWHM of 5.0 μm and 5.3 μm for the cross section profiles of Figure 6-12 b) and d) respectively.

Figure 6-13 shows a PL distribution recorded within the bulk of rubrene. Figure b) shows the fitted spectra with Figures c), d) and e) mapping the central intensity of each fitted peak. The PL distribution is markedly different from that displayed in Figure 6-12. Of note is both the non-symmetric diffusion pattern and the large distance from the excitation point at which there is still a relatively high intensity of PL.

In order to view the variation of the PL spectral components' relative intensities throughout the sample, three Gaussian peaks were fit to the PL spectrum. Equation (6-3) was used for fitting the PL, with I_B denoting the maximum intensity of each Gaussian peak where B denotes the respective band, E_B and σ_B denote the Energy position and width of each peak. E_B, and σ_B remained fixed during fitting.

Fitting was undertaken within the energy spectrum. Fitting in the energy spectrum allows the application of Gaussian functions. A Gaussian function is appropriate as the photoluminescence is the result of many electronic transitions. A Lorentzian which is appropriate for an isolated molecule is therefore not applicable as the many energetic transitions will have a normal distribution around a central mean value. The tails of the function are therefore not as abrupt as in the in Lorentzian and a Gaussian is used. The use of Gaussian and Lorentzian functions is explained in further detail in Chapter 2 of Fox.[59]

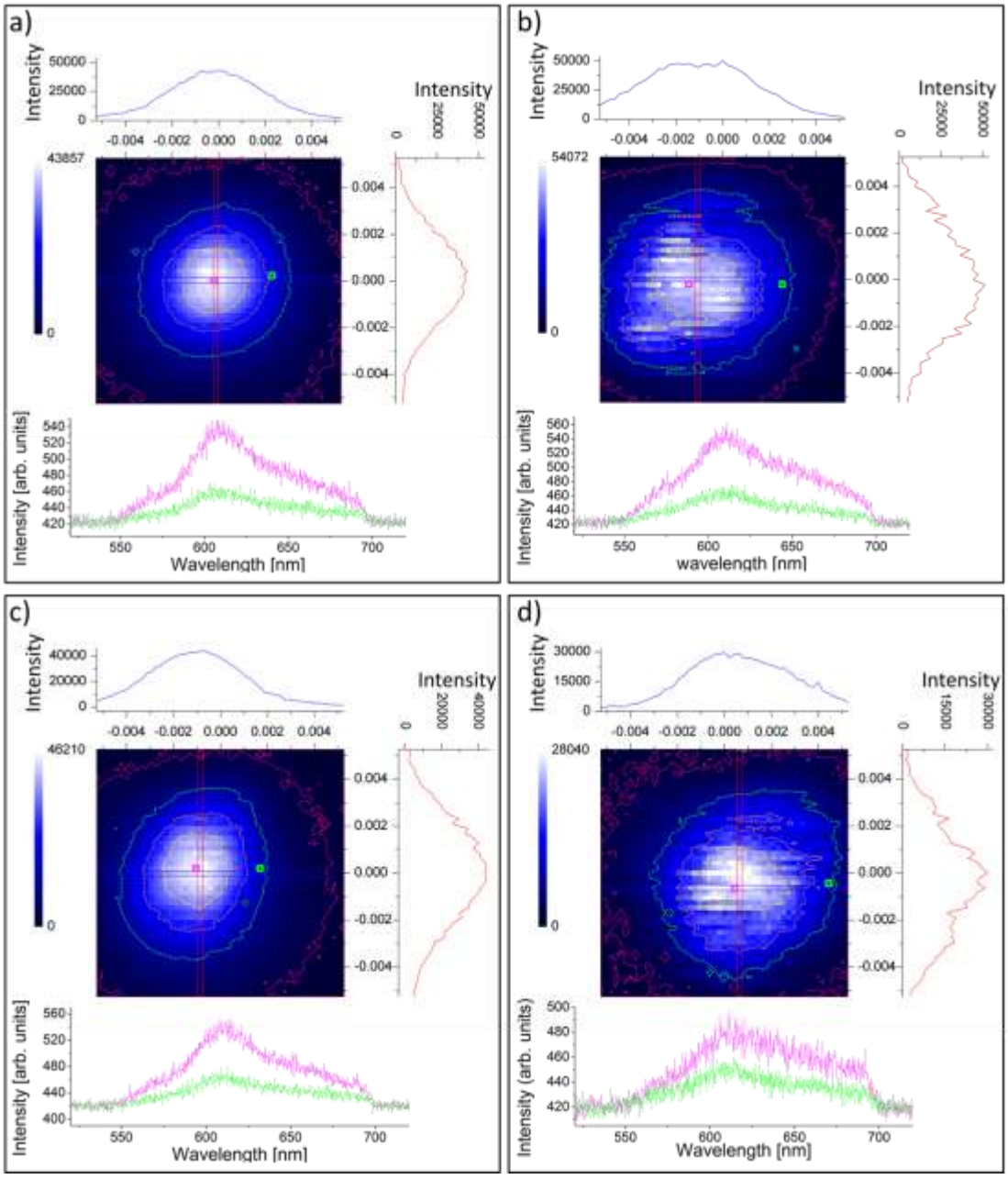

Figure 6-12 PL maps and spectra recorded at the surface and bulk of rubrene. The surface was located using the reflected laser beam. **a)** and **c)** were acquired at the surface with **b)** and **d)** at 40 μm below the surface. a) and b) were recorded at the same lateral location with c) and d) recorded at a location around 500 μm away on the same sample. Cross sections of each PL map are plotted for both directions; the location of the cross section is marked on each map. The spatial location of each spectrum is marked by a colour coded pixel outline. Intensity contour lines are plotted showing 75% - yellow, 50% - orange, 25% - green, and 5% - purple.

The relationship between the photon energy (E) and the wavelength(λ) was calculated using Equation (6-4) where hc=1240 eV·nm.

$$I(E) = I_I e^{-\frac{(E-E_I)^2}{2\sigma_I^2}} + I_{III} e^{-\frac{(E-E_{III})^2}{2\sigma_{III}^2}} + I_O e^{-\frac{(x-E_O)^2}{2\sigma_O^2}} + Offset \quad (6\text{-}3)$$

$$E = \frac{hc}{\lambda} \quad (6\text{-}4)$$

Table 6-1 Fixed parameters used in equation (6-3) to fit photoluminescence spectra.

Parameter \ Band	I	III	O
E_B [eV] (λ [nm])	2.17 (571)	2.06 (603)	1.92 (644)
σ_B [eV]	0.0391	0.0537	0.0732

The fixed values of E_B and σ_B are shown in Table 6-1. These were determined by fitting a strong PL spectrum acquired from the bulk. σ_B and I_B were allowed to vary freely while E_B remained fixed to the position of the three room temperature dominant peaks reported by Mitroanov *et al.*.[30] The final value of σ_B and E_B were set by then allowing all parameters to vary after being initialised with the results of the previous fitting.

The energy locations of the three bands are slightly different to those reported by Mitrofanov *et al.* as Equation (6-3) does not account for the smaller vibronic progressions. One of which is known to lie very close to the position of band O.

The relative intensity of each of the spectral components is not uniform. In comparison, the PL maps presented in Figure 6-12 show a roughly uniform relative intensity of the peaks. This variance in relative peak intensities is highlighted within Figure 6-14 which maps the ratio of the central intensities of fitted peaks corresponding to band O and band III. As can be seen the dominance of band O and III varied depending on the position within the sample.

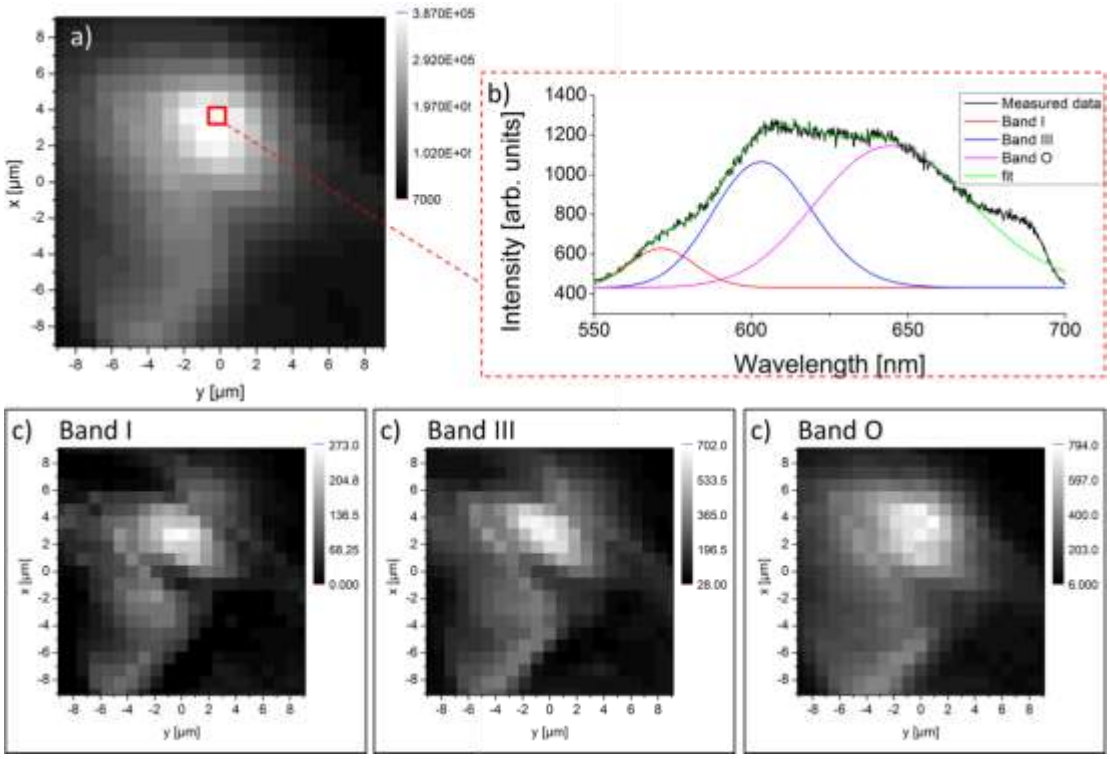

Figure 6-13 Image of PL intensity recorded within the bulk of rubrene at the site of a defect. **a)** Map of integrated PL intensity, **b)** fitted spectra for the indicated pixel in a), **c) d) e)** map of the Maximum Intensity for each respective fitted band.

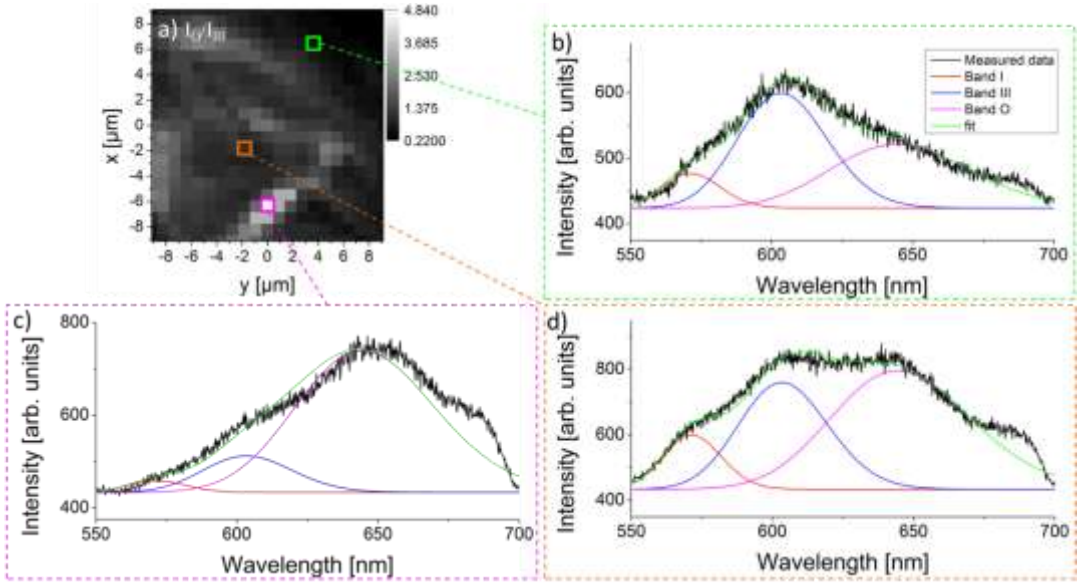

Figure 6-14 a) Map of the ratio of the fitted bands O and III for the images presented in Figure 6-13. **b)**, **c)** and **d)** show the PL and fitted peaks for the labelled pixels in a).

6.5 Discussion of data

Having designed a system to perform 2P excitation††† within the bulk of the crystal, successful acquisition of PL was accomplished. Figure 6-8 shows a PL spectra which is in agreement with previous reported spectra. The PL was emitted from within the bulk of the sample with excitation occurring approximately 40 μm below the surface. The spectra showed a dominant peak at 607 nm which was accompanied by a shoulder attributed to c-polarised emission at 558 nm. At higher wavelengths the PL was not resolvable into individual constituents. This spectra is characteristic of a pristine rubrene crystals with no defects and confirms successful acquisition of PL spectra produced by excitation within the sample.

The data presented in Figure 6-9 shows that the system, working as designed, is only producing excitons at the focal point of the laser beam. This is evident, as when recording the PL, while increasing the sample height, no emission is detected until a sharp rise occurs. The point at which the PL sharply increases occurs as the focal point of the excitation beam coincides with the surface of the sample. However, it is clearly seen that in order to fully understand the depth profiling of samples further characterisation is required. As light is focused below the surface spherical aberrations cause a smearing and shift of the focal plane. This leads to the imaging of apparent unusual PL distributions. This is caused as the system is not imaging at the new effective focal point of the system. Care must be taken for any experiments which are sensitive to sample movement along the optical axis of the system.

If we consider the data presented in Figure 6-12, Figure 6-13 and Figure 6-14 it is possible to build a picture describing some of the excitonic processes occurring within rubrene. The first observation of note is the distribution of PL within the maps in Figure 6-12. The PL distribution is larger than the laser profile presented in Figure 6-7 a). The PL distribution is therefore larger than the excitation profile. From this we can conclude that the excitons must be diffusing from the point of excitation before they radiatively decay. This is in agreement with previous studies by Irkhin *et al.*,[20] which show exciton diffusion occurring within the ab plane of rubrene. The exciton diffusion shown in Figure 6-12 however does not appear to show any crystallographic axis dependence as seen by Irkhin *et al.*. The apparent lack of crystallographic dependence could though, be attributed to the less than ideal spatial resolution of the system.

The spectra presented within Figure 6-12 shows a variation between the surface and bulk measurements. This variation seems to show a suppression of the band III. This is in agreement

††† In order to ensure that excitation occurred due to two photon absorption the PL intensity as a response of power should be measured. This needs to be undertaken before further studies to confirm we are definitely seeing the effect of 2P excitation.

with data presented by Mitrofanov *et al.*.[30] They see both a suppression of band III as well as an increase of band O, as PL excitation moves from the bulk to the surface. It is suggested by Mitrofanov *et al.* that this is due to the inclusion of atmospheric oxygen within the material. The samples used within this study have been stored in atmospheric conditions and therefore this data is consistent with the hypothesis proposed by Mitrofanov *et al.*.

Figure 6-13 and Figure 6-14 show non-symmetric exciton diffusion. The diffusion pattern shows two well orientated lines which are consistent with other PL maps acquired within this sample. The consistent and well orientated PL diffusion implies that presence crystallographic defects which are seen throughout the sample. The defects clearly appear to affect the diffusion of the exciton, stimulating the emission of all the PL bands at specific locations. It is interesting that the emission of the O band appears to occur adjacent to that of the other bands and not at the same position, this is shown clearly in Figure 6-14. The PL distribution implies the recombination of each exciton is affected by the presence of defects within the material. The variation of relative peak intensities further suggests that the recombination of excitons forming the O-band is mediated differently at crystallographic defects. This agrees with Mitrofanov *et al.*,[30, 38] and Chen *et al.*,[79] who both suggest that the presence of the PL band located around 650 nm (band O) is due to the incorporation of defects. As has previously been discussed the origin of this band is disputed. It is debated whether it is due to the incorporation of oxygen or the presence of amorphous rubrene pockets in the crystal. The work presented in this chapter on its own cannot resolve this debate. The increased emission of the O band could feasibly be due to an increase of amorphous inclusions at structural defects, or also an increase in oxygen inclusions which require the steric deformation allowed at structural defects.

6.6 Conclusions

This chapter details the design of a bespoke confocal microscope used to image the photoluminescence distribution both within the bulk and at the surface of rubrene. It has been shown that the system can acquire PL which has been excited from within the bulk. The recorded PL agrees with previous reported pristine rubrene spectra. The system has successfully imaged the PL at a resolution which is able to show the occurrence of exciton diffusion within the material. The exciton diffusion has been seen to vary between the surface and within the bulk, having larger exciton diffusion at the surface. A suppressed 603 nm band III at the surface was also noted. This shows the increased presence of environmentally incorporated defects at the surface, in line with studies by Mitrofanov *et al.*.[30]

The mapping of PL at the location of crystallographic defects has shown the influence of a structural defect upon exciton diffusion, with emission stimulated at the presence of the crystallographic defect. By successfully fitting the PL spectra with 3 Gaussian peaks it has been possible to track the variations in spectral components. This has shown that the emission of the 650 nm line is strongly dependent on the presence of defects, having only a small contribution to the PL where no structural defects are seen to be present. The emission of the 650 nm line is also seen to be spatially displaced from the maximum PL intensity of the other bands. This implies that the recombination pathway leading to 650 nm emission may follow a different process from that of the other bands and is mediated by the presence of a defect. This data on its own however does not shed light on the nature of this defect, whether it is amorphous rubrene as discussed by Chen *et al.* or an oxygen incorporation as put forward by Mitrofanov *et al.*.

The study presented within this chapter provides initial observations of the effect of defects on excitons within rubrene. Notable differences have been observed between the PL of a sample location with no detectable defects and one with a structural defect. In order to provide a full understanding with conclusive evidence these experiments need be undertaken on several more samples. Ideally sample positions with and without defects should be found within one crystal. A full understanding of these effects will have implication on the performance and design of rubrene based devices, in particular photo voltaic cells. The future work of these studies is discussed further in Section 7.2 .

Chapter 7

Conclusions and future work

7.1 Conclusions

The aim of this work was to probe the intrinsic properties of single crystal rubrene and observe how these properties were affected by exposure to the environment and the presence of structural defects. This was undertaken using atomic force microscopy (AFM), time of flight secondary ion mass spectroscopy (ToF-SIMS) and photoluminescent (PL) spectroscopy. The highlights of this work are summarised below followed by a description of future work which has been stimulated by this research.

To study the surface evolution and degradation, a method of cleaving was first devised to produce pristine surfaces free from previous exposure to the ambient. The resulting surfaces, along with the as-grown surfaces, were then analysed using several techniques. To allow nanometre resolution imaging of surface features AFM was used. This allowed the tracking of nanoscale topographical evolution on the surface. With the addition of Conductive-AFM it was possible to obtain information as to how the imaged features affected local electrical properties. In order to further understand the origin of environmental defects within the material, a technique with chemical specificity was sought. ToF-SIMS provided a potentially ideal technique to accomplish this, allowing spatial analysis of the chemical composition at the surface. Finally in order to provide information on the nature of the exciton, a confocal PL arrangement was designed. The microscope used two photon (2P) photoexcitaton to generate excitons and a scanning aperture to spatially map the PL around the point of photo excitation.

Cleaving of the surface was successfully accomplished, reproducibly creating environmentally unexposed surfaces. These were exposed from within the bulk of the crystal and produced large terraces, intersected by straight step edges with regular orientations. The resulting surfaces provided the ideal environment for investigating pure rubrene surfaces. With terraces produced which were larger than any reported in the literature.

By imaging the pristine surfaces of rubrene both immediately after cleaving and after exposure to the environment, two distinct processes were identified; initially the three-dimensional growth of nanoscale beads, followed later by the formation and two-dimensional growth of narrow, monolayer high fingers. The environmental dependence implied the incorporation of an atmospheric component. However, the AFM imaging was unable to provide details on the exact structure and chemical composition of the features. Both features occurred at the location of step edges implying that the environment was suitably different at these positions. The step edges offer a different chemical environment to the terraces and also allow for a degree of steric deformation. Both of these localised properties have the potential to make a reaction with the environment more favourable. The application of C-AFM showed that the beads exhibited an insulating behaviour with an increase in conductivity in a localised area of the crystal surface, directly surrounding to the beads. The lack of conduction implied that the beads were formed in an amorphous phase preventing a continuous overlap of molecular orbitals and therefore obstructing conduction. The results of AFM and C-AFM studies indicate that the presence of crystallographic defects, such as grain boundaries and step edges will control the post growth modification of the surface and in particular the conductivity. The technique though falls short of informing us of the chemical composition of the modified surface.

In striving to analyse the chemical composition both at and below the surface of rubrene, ToF-SIMS was utilised. The technique offers the potential to map the chemical composition in three dimensions. The data acquired provided the first reported ToF-SIMS analysis of rubrene and indeed any organic single crystal surface. The chemical map of the rubrene surface showed the existence of two types of oxide on the surface; a uniform coverage of rubrene-oxide existed across the surface, alongside a lesser rubrene-peroxide signal, which increased considerably at crystallographic defects. The increase of the rubrene peroxide signal at crystallographic defects agrees with the AFM studies which suggest that this molecule can only be incorporated at locations allowing chemical variance as well as steric deformation.

In order to understand how the exciton diffusion is effected by the presence of defects and study the spectral dependence on exciton diffusion, a bespoke PL measurement system was designed and built. This utilised 2P excitation to generate excitons both at the surface and within the bulk of the material. A confocal arrangement with scanning aperture was used to map the resultant PL with spectral resolution. The spatial resolution of the system allowed for the exciton diffusion to be imaged. This diffusion was seen to vary between the bulk and the surface, having a larger distribution when excitation occurred at the surface. It was also seen that at the surface, PL band III, located at 603 nm, was suppressed. This agrees with previous findings by

Mitrofanov *et al.*,[30] which imply that suppression of this band occurs due to a reaction with oxygen in the environment. Mapping the PL produced when exciting a defect incorporated sample showed the strong affect which crystallographic defects have upon the PL distribution profile and spectrum. This sample showed a general increase in the spectral O band at 644 nm, with all PL bands showing an increase in emission at the site of the crystallographic defects. A variance was seen in the location where each band had strongest emission. Band O clearly had the strongest emission displaced from that of the rest of the spectrum. From this it was concluded that the recombination of excitons to produce the O band emission followed a different recombination process to that of the other bands. It is suggested that this recombination is therefore heavily mediated by the presence of defects.

The studies presented within this thesis have provided information on the development of rubrene upon interaction with the environment. This has shown that environmental reactions readily occur at the location of crystallographic defects and step edges. This has been shown by the development of features at step edges and also the presence of rubrene peroxide at crystallographic defects. Further to these observations, which agree with previous reports seen in literature, a uniform oxide was seen to exist at the sample surface. The pristine surface of rubrene (defect free) is thought to be resilient to oxidation. The presence of this uniform oxide is therefore of importance and requires further study.

This work has not only provided novel information on the properties of rubrene but also assembled a set of appropriate techniques and developed methodologies. These enable the systematic characterisation of technologically important processes on organic semiconductors. Cleaving provides an elegant method of reproducibly preparing clean flat surfaces. AFM and ToF-SIMS are shown to be appropriate tools for monitoring the degradation processes that will limit the lifetime of organic electronic devices. The methodologies developed here should extend to other organic single crystals such as pentacene and tetracene.

7.2 Future work

The techniques and methodologies assembled and developed for this research provide a vast array of possible future studies. Much of this future work builds directly upon the work presented here, offering several seamless continuations. The following sections will briefly discuss these proposed studies

7.2.1 Environmentally driven topographical variations

In continuation of the AFM studies, it is necessary to discern which atmospheric components drive the formation of fingers and beads. By controlling the environment in which the surface is cleaved and subsequently evolves it will be possible to identify these atmospheric components. This will be done by cleaving the samples in different environments and imaging the surface after several days within the environment.

The proposed environments are dry high purity nitrogen, dry air, 'wet' high purity nitrogen and 'wet' air. The environments will be created by purging a sealed container to just above atmospheric pressure. The 'wet' environments will be created by passing the purging gas through water.

7.2.2 ToF-SIMS studies

A large portion of the ToF-SIMS studies reported in this thesis have pertained to developing the method required for rubrene analysis. The methodology has now been refined, allowing further utilisation of the technique.

There are several interesting lines of potential study. First, revealing the difference in chemical composition of the as-grown surface and the recently cleaved surface. A recently developed technique allowing in-situ cleaving will also allow analysis of the unexposed cleaved surface. Although the resolution of the system (100 nm) will not allow chemical mapping of individual beads, it will be possible to view the chemical variance between terraces and step edges where there is a high density of beads. It is proposed that these studies may be done in conjunction with Ion-TOF who have the world's only AFM and ToF-SIMS combined machine.

ToF-SIMS will also be instrumental in understanding the nature of oxidation within crystalline rubrene. This will include further studies to understand the presence of atomic oxygen seen at the top monolayer and the presence of defects. This inclusion of oxygen is of interest as it does not show any correlation with the presence of oxidised rubrene. These studies will involve local anodic oxidation, which showed this atomic oxygen inclusion, as well as studying the depth profile of oxygen and rubrene oxide.

In conjunction with PL studies ToF-SIMS should be able to provide conclusive data regarding the 650nm PL emission and its relation to oxidised rubrene. This can be done by comparing maps and depth profiles of PL and chemical composition.

7.2.3 Further development of optical studies,

Further refining of the scanning optical microscope design will allow for an increased resolution of the system. By increasing the numerical aperture of both the microscope objective and the focusing lens, it should be possible to quantitatively measure the diffusion length of the excitons. Further work is needed to develop the z-axis resolution of the system. This will take into account the spherical aberrations which are inherent within the system. Initially a calibration curve should be calculated and measured to estimate the focal position with respect to depth. This will allow mapping in the z direction and will lead to an understanding of the limitations of the confocal nature of the system.

7.2.4 Development and characterisation of rubrene solar cells

The ultimate goal in characterisation of rubrene is to enable design and optimisation of rubrene based electronic devices. The optical and electrical properties of rubrene, namely long exciton diffusion and high charge carrier mobilities, make it an ideal candidate for solar cell development.

The techniques presented within this thesis offer an ideal basis for probing the physical processes which occur in solar cell devices. Understanding these processes will provide optimal specifications for the device such as, contact spacing, active layer thickness and surface treatment. Figure 7-1 shows a rubrene solar cell concept.

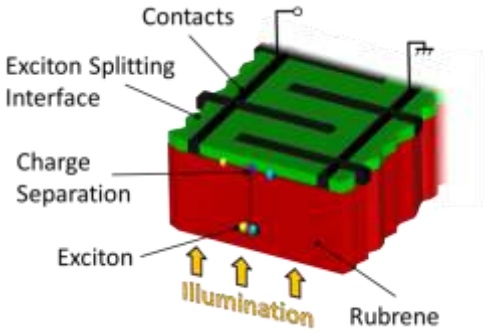

Figure 7-1 Concept of a solar cell device based on a thinly cleaved rubrene sample.

The proposed study to enable solar cell design will electronically probe exciton diffusion. This would be done by developing the confocal microscope system with the addition of an in-situ C-AFM. 2P excitation would occur within the bulk, with a C-AFM cantilever at the surface measuring the resultant electrical current. Figure 7-2 illustrates this system.

In order to progress with the development of a rubrene solar cell, the following plan should be implemented. First of all, determine factors which affect the conversion efficiency. This would be done by developing a full understanding of the photo-carrier generation process in rubrene, from photon absorption, through exciton diffusion to the carrier separation process. The second stage would evaluate the impact of rubrene interfaces (with other organic materials, as well as with the environment) on exciton splitting and develop methods for modifying and controlling electronic and optical properties of rubrene on the microscopic level. Finally, in order to develop a photovoltaic cell prototype and find the optimal operation conditions, fabrication methods would be developed. These methods would be: (1) producing devices with required rubrene thickness, (2) deposition of exciton splitting interfaces and (3) developing compatible electrical contacts.

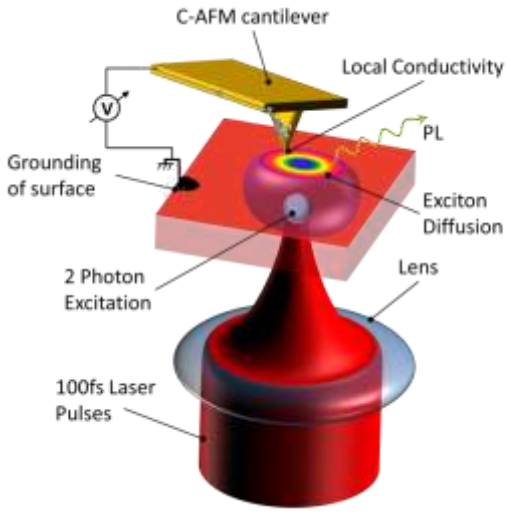

Figure 7-2 Proposed scanning probed microscope system which combines C-AFM, confocal PL spectroscopy and 2 photon microscopy.

Academic activity

Publications

Thompson, R.J., *et al.* "Revealing surface oxidation on the organic semi-conducting single crystal rubrene with Time of Flight Secondary Ion Mass Spectroscopy." Phys. Chem. Chem. Phys. **(2013)**

Thompson, R.J., *et al.* "Morphology of cleaved rubrene and its evolution in an ambient environment." SPIE Photonic Devices+ Applications. International Society for Optics and Photonics. **(2011)**

Thompson, R.J., *et al.* "Evolution of the surface morphology of rubrene under ambient conditions." Applied Physics Letters, 98.5 **(2011)**

Conference presentations

Thompson, R.J., *et al.* "A study of Rubrene Surface Evolution." MRS-fall (2011)

Thompson, R.J., *et al.* "ToF-SIMS (Time of Flight Secondary Ion Mass Spectroscopy) studies of Rubrene Single Crystals." MRS-fall (2011)

Thompson, R.J., *et al.* "Morphology of cleaved rubrene and its evolution in an ambient environment." SPIE Optics + Photonics 2011 (2011)

Thompson, R.J., *et al.* "Cleaved rubrene surfaces: surface reactions and oxidation." ICMAT (2011)

Thompson, R.J., *et al.* "Evolution of topography and conduction at the surface of rubrene." ICMAT (2011)

Thompson, R.J., *et al.* "Studies of the cleaved surface of rubrene with relevance to rubrene electrical devices." ICMAD Korea (2011)

Fearn, S., **Thompson, R.J.**, *et al.* "Ion Beam Interactions on Organic (2011)

Single Crystals" SIMS XVIII

Mitrofanov, O., **Thompson, R.**, *et al.* "THz near-field microscopy of graphene nano-ribbon arrays" CLEO 2013 (2013)

Awards

Cullen Prize, (first place) – UCL E&EE dept. Research poster competition (2011)

UCL graduate school Research poster competition (runner up) (2011)

Bibliography

[1] Blanchet, G., Loo, Y., Rogers, J., Gao, F., and Fincher, C. *Applied Physics Letters* **82**(3), 463–465 (2003).

[2] Klauk, H. *Organic Electronics: Materials, Manufacturing, and Applications*. Wiley-VCH, (2006).

[3] Podzorov, V. *MRS Bulletin* **38**(01), 15–24 (2013).

[4] Sheats, J. *Journal of Materials Research* **19**(07), 1974–1989 (2004).

[5] Stingelin-Stutzmann, N., Smits, E., Wondergem, H., Tanase, C., Blom, P., Smith, P., and de Leeuw, D. *Nature materials* **4**(8), 601–606 (2005).

[6] Alibart, F., Pleutin, S., Guérin, D., Novembre, C., Lenfant, S., Lmimouni, K., Gamrat, C., and Vuillaume, D. *Advanced Functional Materials* **20**(2), 330–337 (2010).

[7] Owens, R. and Malliaras, G. *MRS bulletin* **35**(06), 449–456 (2010).

[8] Søndergaard, R. R., Hösel, M., and Krebs, F. C. *Journal of Polymer Science Part B: Polymer Physics* **51**(1), 16–34 (2013).

[9] Forrest, S. R. *Nature* **428**(6986), 911–918 (2004).

[10] Turbiez, M., Frere, P., Allain, M., Videlot, C., Ackermann, J., and Roncali, J. *Chemistry-A European Journal* **11**(12), 3742–3752 (2005).

[11] Yoon, M., Facchetti, A., Stern, C., and Marks, T. *Journal of the American Chemical Society* **128**(17), 5792–5801 (2006).

[12] Helfrich, W. and Schneider, W. *Physical Review Letters* **14**(7), 229–231 (1965).

[13] Pope, M., Kallmann, H., and Magnante, P. *The Journal of Chemical Physics* **38**(8), 2042–2043 (1963).

[14] Chiang, C., Fincher Jr, C., Park, Y., Heeger, A., Shirakawa, H., Louis, E., Gau, S., and MacDiarmid, A. *Phys. Rev. Lett* **39**(1098), 1098 (1977).

[15] Heeger, A. J. *Angewandte Chemie International Edition* **40**(14), 2591–2611 (2001).

[16] MacDiarmid, A. *Reviews of Modern Physics* **73**(3), 701–712 (2001).

[17] Shirakawa, H. *Reviews of Modern Physics* **73**(3), 713 (2001).

[18] Coropceanu, V., Li, Y., Yi, Y., Zhu, L., and Brédas, J. *MRS Bulletin* **38**(01), 57–64 (2013).

[19] Gershenson, M., Podzorov, V., and Morpurgo, A. *Reviews of modern physics* **78**(3), 973 (2006).

[20] Irkhin, P. and Biaggio, I. *Physical Review Letters* **107**(1), 017402 (2011).

[21] Najafov, H., Lee, B., Zhou, Q., Feldman, L., and Podzorov, V. *Nature materials* **9**(11), 938–943 (2010).

[22] Podzorov, V., Pudalov, V., and Gershenson, M. *Applied physics letters* **85**(24), 6039–6041 (2004).

[23] Takeya, J., Yamagishi, M., Tominari, Y., Hirahara, R., Nakazawa, Y., Nishikawa, T., Kawase, T., Shimoda, T., and Ogawa, S. *Applied Physics Letters* **90**(10), 102120–102120 (2007).

[24] *http://www.eight19.com/* .

[25] Zhang, K., Tan, K., Zou, C., Wikberg, M., McNeil, L., Mhaisalkar, S., and Kloc, C. *Organic electronics* **11**(12), 1928–1934 (2010).

[26] Briseno, A., Mannsfeld, S., Ling, M., Liu, S., Tseng, R., Reese, C., Roberts, M., Yang, Y., Wudl, F., and Bao, Z. *Nature* **444**(7121), 913–917 (2006).

[27] Briseno, A., Tseng, R., Ling, M., Falcao, E., Yang, Y., Wudl, F., and Bao, Z. *Advanced Materials* **18**(17), 2320–2324 (2006).

[28] Podzorov, V., Pudalov, V., and Gershenson, M. *Applied physics letters* **82**(11), 1739–1741 (2003).

[29] Podzorov, V., Sysoev, S., Loginova, E., Pudalov, V., and Gershenson, M. *Applied Physics Letters* **83**(17), 3504–3506 (2003).

[30] Mitrofanov, O., Lang, D., Kloc, C., Wikberg, J., Siegrist, T., So, W., Sergent, M., and Ramirez, A. *Physical review letters* **97**(16), 166601 (2006).

[31] Petrenko, T., Krylova, O., Neese, F., and Sokolowski, M. *New Journal of Physics* **11**(1), 015001 (2009).

[32] Jurchescu, O. D., Meetsma, A., and Palstra, T. T. *Acta Crystallographica Section B: Structural Science* **62**(2), 330–334 (2006).

[33] Bowen, E. and Williams, A. *Transactions of the Faraday Society* **35**, 765–771 (1939).

[34] Kytka, M., Gerlach, A., Schreiber, F., and Kovac, J. *Applied physics letters* **90**(13), 131911–131911 (2007).

[35] Wu, K. and Trozzolo, A. *Journal of Physical Chemistry* **83**(22), 2823–2826 (1979).

[36] Henn, D., Williams, W., and Gibbons, D. *Journal of Applied Crystallography* **4**(3), 256–256 (1971).

[37] Laudise, R., Kloc, C., Simpkins, P., and Siegrist, T. *Journal of crystal growth* **187**(3), 449–454 (1998).

[38] Mitrofanov, O., Kloc, C., Siegrist, T., Lang, D., So, W., and Ramirez, A. *Applied Physics Letters* **91**(21), 212106–212106 (2007).

[39] Pope, M. and Swenberg, C. *Electronic processes in organic crystals and polymers*, volume 2. Oxford University Press, (1999).

[40] Brédas, J., Calbert, J. P., da Silva Filho, D., and Cornil, J. *Proceedings of the National Academy of Sciences* **99**(9), 5804–5809 (2002).

[41] da Silva Filho, D., Kim, E., and Brédas, J. *Advanced Materials* **17**(8), 1072–1076 (2005).

[42] Bulgarovskaya, I., Vozzhennikov, V., Aleksandrov, S., and Belsky, V. *Latv. PSR Zinat. Akad. Vestis,Khim. Ser.* **53** (1983).

[43] [edited by] Zhenan Bao, J. L. *Organic Field-Effect Transistors*. Boca Raton ; London : CRC Press, (2007).

[44] Menard, E., Podzorov, V., Hur, S., Gaur, A., Gershenson, M., and Rogers, J. *Advanced materials* **16**(23-24), 2097–2101 (2004).

[45] Podzorov, V., Menard, E., Borissov, A., Kiryukhin, V., Rogers, J., and Gershenson, M. *Physical review letters* **93**(8), 086602 (2004).

[46] Takeya, J., Nishikawa, T., Takenobu, T., Kobayashi, S., Iwasa, Y., Mitani, T., Goldmann, C., Krellner, C., and Batlogg, B. *Applied physics letters* **85**(21), 5078–5080 (2004).

[47] Bisri, S., Takenobu, T., Takahashi, T., and Iwasa, Y. *Applied Physics Letters* **96**(18), 183304–183304 (2010).

[48] Kymissis, I. *Organic Field Effect Transistors: Theory, Fabrication and Characterization*. Springer, (2009).

[49] Sze, S. and Ng, K. *Physics of semiconductor devices*. Wiley-interscience, (2006).

[50] Reese, C. and Bao, Z. *Advanced Materials* **19**(24), 4535–4538 (2007).

[51] Podzorov, V., Menard, E., Rogers, J., and Gershenson, M. *Physical review letters* **95**(22), 226601 (2005).

[52] Farchioni, R. *Organic electronic materials: conjugated polymers and low molecular weight organic solids*, volume 41. Springer Verlag, (2001).

[53] Greene, B. and Millard, R. *Physical review letters* **55**(12), 1331–1334 (1985).

[54] Huang, L., Liao, Q., Shi, Q., Fu, H., Ma, J., and Yao, J. *Journal of Materials Chemistry* **20**(1), 159–166 (2010).

[55] Ma, L., Zhang, K., Kloc, C., Sun, H., Michel-Beyerle, M., and Gurzadyan, G. *Physical Chemistry Chemical Physics* **14**(23), 8307–8312 (2012).

[56] Irkhin, P., Ryasnyanskiy, A., Koehler, M., and Biaggio, I. *Physical Review B* **86**(8), 085143 (2012).

[57] Tavazzi, S., Borghesi, A., Papagni, A., Spearman, P., Silvestri, L., Yassar, A., Camposeo, A., Polo, M., and Pisignano, D. *Physical Review B* **75**(24), 245416 (2007).

[58] Bardeen, C. *MRS Bulletin* **38**(01), 65–71 (2013).

[59] Fox, A. M. *Optical properties of solids*, volume 3. Oxford university press, (2001).

[60] Knupfer, M. *Applied Physics A* **77**(5), 623–626 (2003).

[61] Karak, S., Lim, J. A., Ferdous, S., Duzhko, V. V., and Briseno, A. L. *Advanced Functional Materials* (2013).

[62] Najafov, H., Lyu, B., Biaggio, I., and Podzorov, V. *Applied Physics Letters* **96**(18), 183302–183302 (2010).

[63] Hummer, K. and Ambrosch-Draxl, C. *Physical Review B* **71**(8), 081202 (2005).

[64] Brédas, J., Norton, J., Cornil, J., and Coropceanu, V. *Accounts of chemical research* **42**(11), 1691–1699 (2009).

[65] Gregg, B. A. *The Journal of Physical Chemistry B* **107**(20), 4688–4698 (2003).

[66] Yi, Y., Coropceanu, V., and Bre?das, J. *Journal of the American Chemical Society* **131**(43), 15777–15783 (2009).

[67] Smith, M. and Michl, J. *Chemical reviews* **110**(11), 6891 (2010).

[68] Johnson, J. C., Nozik, A. J., and Michl, J. *Journal of the American Chemical Society* **132**(46), 16302–16303 (2010).

[69] Rao, A., Wilson, M., Hodgkiss, J., Albert-Seifried, S., Ba?ssler, H., and Friend, R. *Journal of the American Chemical Society* **132**(36), 12698–12703 (2010).

[70] Singh, S., Jones, W., Siebrand, W., Stoicheff, B., and Schneider, W. *The Journal of Chemical Physics* **42**, 330 (1965).

[71] Wang, C. and Tauber, M. *Journal of the American Chemical Society* **132**(40), 13988–13991 (2010).

[72] Wen, X., Yu, P., Yuan, C.-T., Ma, X., and Tang, J. *The Journal of Physical Chemistry C* (2013).

[73] Maliakal, A., Chen, J., So, W., Jockusch, S., Kim, B., Ottaviani, M., Modelli, A., Turro, N., Nuckolls, C., and Ramirez, A. *Chemistry of Materials* **21**(22), 5519–5526 (2009).

[74] So, W., Wikberg, J., Lang, D., Mitrofanov, O., Kloc, C., Siegrist, T., Sergent, A., and Ramirez, A. *Solid state communications* **142**(9), 483–486 (2007).

[75] Thompson, R., Yadin, B., Grout, Z., Hudziak, S., Kloc, C., Curson, N., and Mitrofanov, O. In *SPIE Photonic Devices+ Applications*, 811712–811712. International Society for Optics and Photonics, (2011).

[76] Thompson, R., Yadin, B., Grout, Z., Hudziak, S., Kloc, C., Mitrofanov, O., and Curson, N. *Applied Physics Letters* **98**(5), 053302–053302 (2011).

[77] Uttiya, S., Raimondo, L., Campione, M., Miozzo, L., Yassar, A., Moret, M., Fumagalli, E., Borghesi, A., and Sassella, A. *Synthetic Metals* **161**(23), 2603–2606 (2012).

[78] Kloc, C., Tan, K., Toh, M., Zhang, K., and Xu, Y. *Applied Physics A* **95**(1), 219–224 (2009).

[79] Chen, Y., Lee, B., Fu, D., and Podzorov, V. *Advanced Materials* **23**(45), 5370–5375 (2011).

[80] De Boer, R., Gershenson, M., Morpurgo, A., and Podzorov, V. *physica status solidi (a)* **201**(6), 1302–1331 (2004).

[81] Binnig, G., Quate, C., and Gerber, C. *Physical review letters* **56**(9), 930–933 (1986).

[82] Menard, E., Marchenko, A., Podzorov, V., Gershenson, M., Fichou, D., and Rogers, J. *Advanced Materials* **18**(12), 1552–1556 (2006).

[83] Minato, T., Aoki, H., Fukidome, H., Wagner, T., and Itaya, K. *Applied Physics Letters* **95**, 093302 (2009).

[84] Horcas, I., Fernandez, R., Gomez-Rodriguez, J., Colchero, J., Gómez-Herrero, J., and Baro, A. *Review of Scientific Instruments* **78**, 013705 (2007).

[85] Lee, B., Choi, T., Cheong, S., and Podzorov, V. *Advanced Functional Materials* **19**(23), 3726–3730 (2009).

[86] Machida, S., Nakayama, Y., Duhm, S., Xin, Q., Funakoshi, A., Ogawa, N., Kera, S., Ueno, N., and Ishii, H. *Physical review letters* **104**(15), 156401 (2010).

[87] Thompson, R., Fearn, S., Kloc, C., Curson, N., and Mitrofanov, O. *Phys. Chem. Chem. Phys.* **15**, 5202–5207 (2013).

[88] Najafov, H., Lyu, B., Biaggio, I., and Podzorov, V. *Physical Review B* **77**(12), 125202 (2008).

[89] El Helou, M., Medenbach, O., and Witte, G. *Crystal Growth & Design* **10**(8), 3496–3501 (2010).

[90] Käfer, D. and Witte, G. *Physical Chemistry Chemical Physics* **7**(15), 2850–2853 (2005).

[91] De Biévre, P. and Taylor, P. *International Journal of Mass Spectrometry and Ion Processes* **123**, 149–166 (1993).

[92] Zhu, Z., Nachimuthu, P., and Lea, A. *Analytical chemistry* **81**(20), 8272–8279 (2009).

[93] Vickerman, J. C. and Briggs, D. *ToF-SIMS: surface analysis by mass spectrometry*. IM publications Chichester, (2001).

[94] Briggs, D. and Hearn, M. *Vacuum* **36**(11), 1005–1010 (1986).

[95] Mahoney, C. *Mass spectrometry reviews* **29**(2), 247–293 (2010).

[96] Py, M., Barnes, J., Charbonneau, M., Tiron, R., and Buckley, J. *Surface and Interface Analysis* **43**(1-2), 179–182 (2011).

[97] Shard, A., Green, F., and Gilmore, I. *Applied Surface Science* **255**(4), 962–965 (2008).

[98] Lee, J., Kang, M., Lim, W., Shin, K., and Lee, Y. *Surface and Interface Analysis* **45**(1), 498–502 (2013).

[99] Sjovall, P., Rading, D., Ray, S., Yang, L., and Shard, A. *The Journal of Physical Chemistry B* **114**(2), 769–774 (2009).

[100] Houssiau, L. and Mine, N. *Surface and Interface Analysis* **43**(1-2), 146–150 (2011).

[101] Lu, C., Wucher, A., and Winograd, N. *Analytical chemistry* **83**(1), 351–358 (2010).

[102] Shard, A., Green, F., Brewer, P., Seah, M., and Gilmore, I. *The Journal of Physical Chemistry B* **112**(9), 2596–2605 (2008).

[103] Cervenka, J., Kalousek, R., Bartošk, M., Škoda, D., Tomanec, O., and Šikola, T. *Applied Surface Science* **253**(5), 2373–2378 (2006).

[104] Day, H. and Allee, D. *Applied physics letters* **62**(21), 2691–2693 (1993).

[105] Ma, Y., Yu, C., Yao, Y., Liou, Y., and Lee, S. *Physical Review B* **64**(19), 195324 (2001).

[106] Hecht, E. and Zajac, A. *Addison-Wesley* **2**, 163–169 (2002).

[107] Panico, R., Powell, W. H., and Richer, J.-C. *A guide to IUPAC Nomenclature of Organic Compounds*. Blackwell Scientific Publ., (1993).

[108] Seki, T., Matsuo, J., Takaoka, G., and Yamada, I. *Nuclear Instruments and Methods in Physics Research Section B: Beam Interactions with Materials and Atoms* **206**, 902–906 (2003).